Flow-Through PIN Photodiodes for Integrated Micro Diagnostic Biosensors

Bonghoe Kim

A thesis
submitted in partial fulfillment of the
requirements for the degree of

Master of Science in Electrical Engineering

University of Washington
2014

Committee:

Robert Bruce Darling (Chair)

Manjari. P. Anantram

Tai-Chang Chen

Program Authorized to Offer Degree: Electrical Engineering

Abstract

Flow-Through PIN Photodiodes for Integrated Micro Diagnostic Biosensors

Bonghoe Kim

Chair of the Supervisory Committee:

Professor Robert Bruce Darling
Department of Electrical Engineering

This study focuses on the design, fabrication, and evaluation of a trench Flow-Through PIN Photodiode (FTPD). Highly sensitive silicon PIN photodiodes embedded into the bottom as well as the sidewalls of a microfluidic channel can significantly improve the collection of photons emitted from particles in the channel. And a 360 degree angular field of view (FOV) of the sensor minimizes the optical loss. The microfluidic channel was made by a deep reactive ion etching (DRIE) process so that photo-luminescent particles can flow through the photodiodes. The geometry that has been investigated for the trench FTPD is surprisingly simple, and requires only three diffusions; one for n+, two for p+; a DRIE etching step to create the microfluidic channels, and metal contacts for the anode and cathode. However, the deep trenches requires specialized photolithography steps. The FTPDs characteristics of dark current, breakdown voltage, photocurrent versus wavelength, and responsivity to light were measured and compared against other test structures and commercial photodiodes. The trench FTPD exhibited a 114 nA background dark current at −2 V and a maximum photocurrent of 256 nA from phosphorescent microspheres of 5.59 nW optical power. By comparison, a planar type PD of the same lateral area shows only 14.8 nA of photocurrent generated by phosphorescent emission from the same microspheres. The back ground dark current of planar type PD is 2.83 nA at −2 V. The FTPD improves photon collection efficiency and responsivity to light over that of conventional planar type photodiodes due to the larger active area of photodiodes. This sensor can be used for biosensing applications such as disease detection, cell counting, laser induced fluorescence detection, and miniaturized total analysis systems.

TABLE OF CONTENTS

LIST OF FIGURES

LIST OF TABLES

ACKNOWLEDGEMENTS

I wish to express sincere appreciation to the Department of Electrical Engineering for their extended long-term support and especially to Professor Robert Bruce Darling for his vast reserve of patience and knowledge. If he had not given me an opportunity to work with him, I would not be where I am now. This thesis would never have been completed without the encouragement and devotion of my supervisor and my family.

I thank my beloved father, mother, sister, and friends for their prayers, supports, and encouragement through my study. Finally, I thank Trinity and the Lord for all of the grace and blessings they have given to me.

DEDICATION

To my parents and the Lord.

Chapter 1

Introduction

The world market for biosensor includes blood glucose measurement for diabetes patients and pregnancy testing kits as examples [1]. Low cost and portable biosensors have been employed in various applications, and have stimulated the development and improvement of point of care systems.

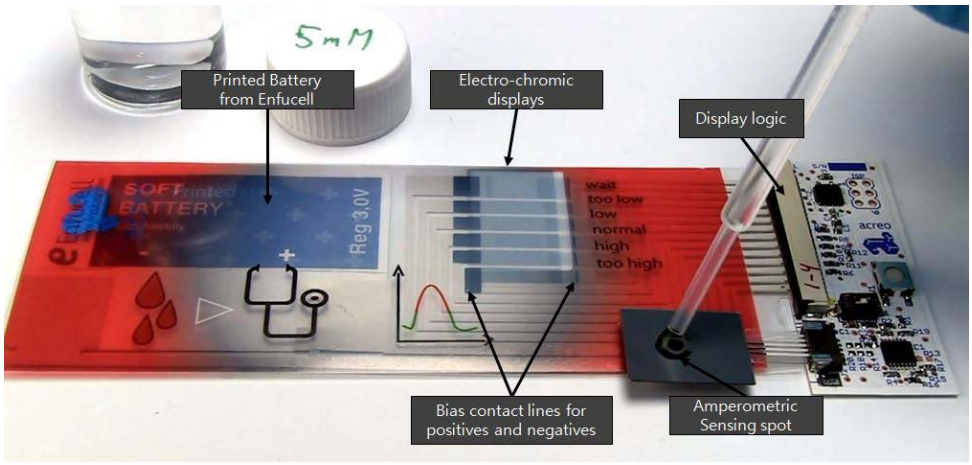

Figure 1.1. An amperometric biosensor system fabricated by printed electronic techniques Original image from www.acreo.se [2].

For instance, the all-printed amperometric biosensor system as shown in Fig. 1.1 is a typical example of a portable and low cost biosensing system [2].

In addition to electronic biosensing systems, the use of optics allows greater flexibility in more applications, such as deoxyribonucleic acid (DNA) sequencing for gene expression and mapping, immunosensing, pathogen detection, environmental biohazard detection, cytometry, and other medical diagnostics [3-6]. However, commercial optical biosensors have limitations, particularly their ability to efficiently collect emitted light from particles, and new type of sensor has been developed to overcome these drawbacks [7].

1.1 Optical biosensing systems for micro diagnostics

1.1.1 Integrated optical sensing systems

The acronym μTAS, short for Micro Total Analysis System and the term lab-on-a-chip epitomize the technologies of integrated miniaturized chemical analysis systems that include sample preparation, particulate filters, mixers and detection systems on a small and single chip. Recently, these have been utilized for chemical processing, implementing micro-organs, DNA fluorescent sequencing, and

analysis of drugs and metabolites, as compact chemical and biological analysis systems. μTAS has drawn more attention due to the fact that it has more varied applications in biomedical diagnostics using opto-fluidic sensors.

Integrated optical sensing systems can offer fairly good sensitivity and specificity [4,7]. In most past research work prototype integrated fluorescence optical sensors have used commercial photodiodes. These have generally been attached and aligned simply over the top of the fluidic channels, sometimes with optical fibers to route the light from the sample to the detector [8-11]. Fig. 1.2 depicts a typical fluorescence detection system employing PIN photodiodes. Emitted light from the particles in the fluidic channel can be detected by PIN photodiodes coupled with optical fibers. PIN photodiodes convert the light to an electrical signal, and the generated signal is amplified by a pre-amplifier.

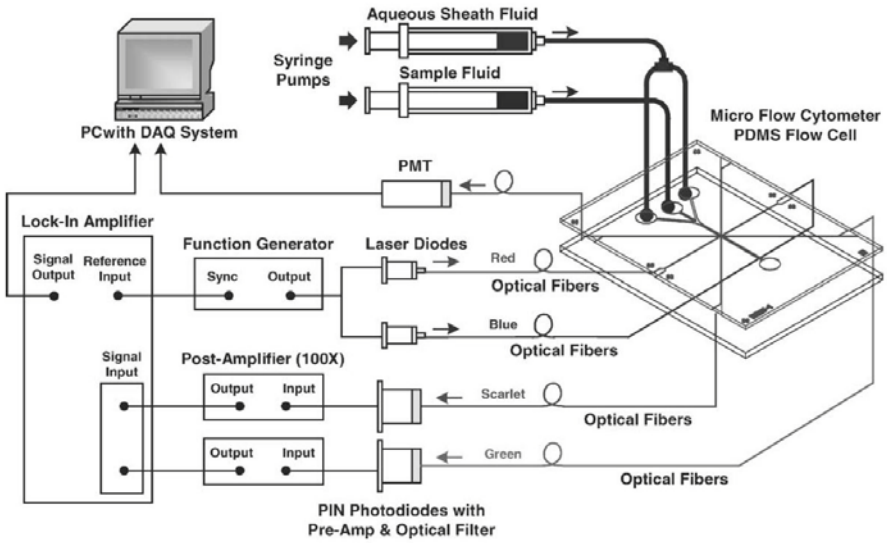

Figure 1.2. An example of fluorescence detection system with PIN photodiodes [11].

1.1.2 Fluorescence microscopy systems

In terms of the instrumentation, fluorescence microscopy is one of the most widely used systems in biomedical research. Today, fluorescence microscopy is used not only for the identification and classification of small particles or molecules, but also for quantitative measurement of biological processes and phenomena. Through these applications in research fields, fluorescence microscopy system has continued to prosper. To detect fluorescent light, fluorescence microscopy systems employ a CCD or a CMOS imager, and the captured images are analyzed by processing software to extract quantitative data. [12-13]. Various optical filters are often used in florescence microscopy to help improve the efficiency and image quality, and to measure multiplexed data emitted from multiple colored targets.

Figure 1.3 illustrates a typical fluorescence microscope and its architecture. From a laser source, the excitation light hits the sample in the specimen imaging chamber through an excitation filter and a

dichroic mirror. The excitation filter removes stray output associated with the emission wavelength of the light, and the dichroic mirror reflects only the desired wavelengths. Flourophore particles in the sample chamber emit fluorescent light at a different wavelength than their excitation. This emitted light is allowed to pass through the dichroic mirror because it has a longer wavelength than that of the excitation light. The light passes on to a photomultiplier tube (PMT) or a CCD image sensor passing through filters and focusing lens

In spite of its wide capabilities for biological measurements, the imaging system of a fluorescence microscope is bulky, and too expensive to be considered as a practical detection system for point-of-care applications [14].

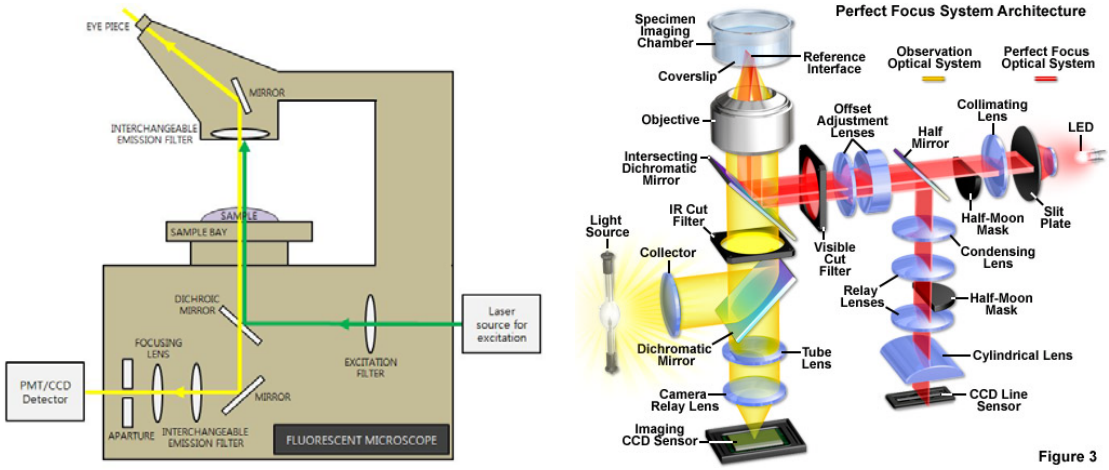

Figure 1.3. Schematic of a typical microscope system utilized in fluorescence imaging, Nikon microscopy system [7, 15].

1.2 Limitations and possible solutions using existing optical biosensors

Even though many novel optical biosensors have been developed for highly sensitive detection systems, there are still some limitations on their performance.

A common requirement for a lab-on-a-chip system is fluorescence detection. Such a system consists of flow channels, optical fibers for excitation and detection of the fluorescent particles, photodetectors or a fluorescence microscope. However, conventional fluorescence detection systems remain bulky and expensive, especially because many additional peripheral components are necessary. One of the many challenges to solve in fluorescence detection systems is an improvement of their sensitivity or photon collection efficiency.

The goal of this work is to develop optoelectronic devices with high photon collection efficiency by designing a simple but effective device structure for micro diagnostics. The proposed devices will provide a new solution for existing biosensors which are currently non-portable and expensive traditional analysis instruments.

In addition to portability and cost issues, another limitation is caused by the geometry of the sensors themselves. One of the critical drawbacks of these methods is that they commonly introduce a tremendous optical loss, since the angular field of view (FOV) of systems coupled to commercial planar photodiodes is only a few degrees. Consequently, many biosensors using fluorescent detection exhibit poor sensitivity because the majority of the photons from the isotropic emission fluorescing molecules are lost. Diagrammatic cross sections of a commercial photodiode and its general methods for collecting fluorescent light from a microfluidic optical-sensor prototypes are shown in Fig 1.4.

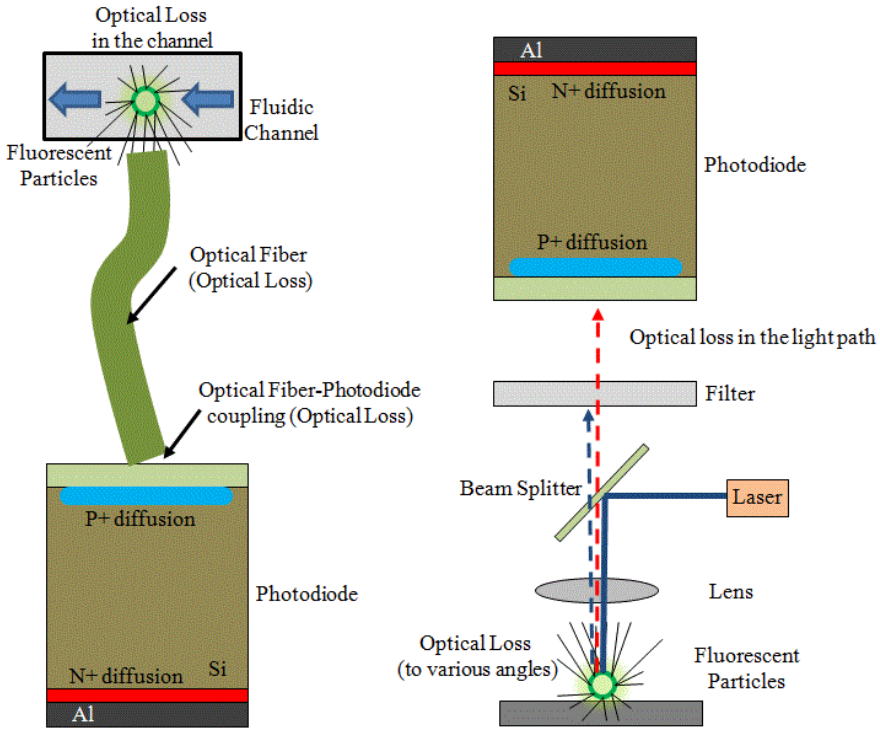

(a) (b)

Figure 1.4. Cross sections of a commercial photodiode and its general methods for collecting fluorescent light from a microfluidic optical-sensor prototypes, (a) Key components of the fluorescence detection system (Polydimethylsiloxane (PDMS) flow channel, a optical fiber and a photodiode) (b) principle of operation.

By modifying the geometry of the sensor, it can be possible to improve the photon collection efficiency of the sensor. The angular FOV of a system using coupled photodiodes can be dramatically increased by placing the photodiodes around all interior surfaces of the flow channel. The angular FOV of a few degrees for a general planar commercial photodiode can be increased to nearly the maximum of 360 degrees using this technique. This design structure is referred to as a Flow-Through PIN Photodiode (FTPD). The proposed sensor designs are expected to overcome these limitations of low photon collection efficiency.

1.3 Thesis organization

This thesis develops a new design for a PIN photodiode which offers photon collection for highly sensitivity fluorescence or phosphorescence microfluidic sensing applications. This chapter has discussed the motivation and possible solution to overcome the limitations of conventional planar photodiodes which have so far been used for microfluidic biosensing.

The thesis is divided into five parts. Chapter 2 describes the fundamentals of semiconductor optoelectronic devices, which is the foundation of the proposed devices. The physics of pn-junction diodes, the principle of operation of a silicon PIN photodiode, and the current-voltage characteristics are discussed. Chapter 3 describes the design and microfabrication of the devices. All of the design considerations and fabrication steps are introduced including the device structure and the fabrication issues. The results of the electrical, optical, and microfluidic measurements are presented in Chapter 4. Finally, Chapter 5 summarizes further experimental plans to improve the prototype sensor.

Chapter 2
Semiconductor photodiodes

The key component for an integrated optical biosensing system is the semiconductor photodiode. In this chapter, a general introduction to the physics of semiconductor photodiodes is presented. This discussion will include the semiconductor physics of optical transitions, silicon PIN photodiodes, photoluminescence and performance factors of photodetectors.

2.1 Semiconductor band gap and optical transitions

The most important material consideration for optoelectronic devices is the energy band structure. Commonly used semiconductor materials are silicon (Si), germanium (Ge), and gallium arsenide (GaAs), each with a cubic crystal lattice structure. The bandgap of a semiconductor refers to the minimum energy difference between the top edge of the valence band and the bottom edge of the conduction band.

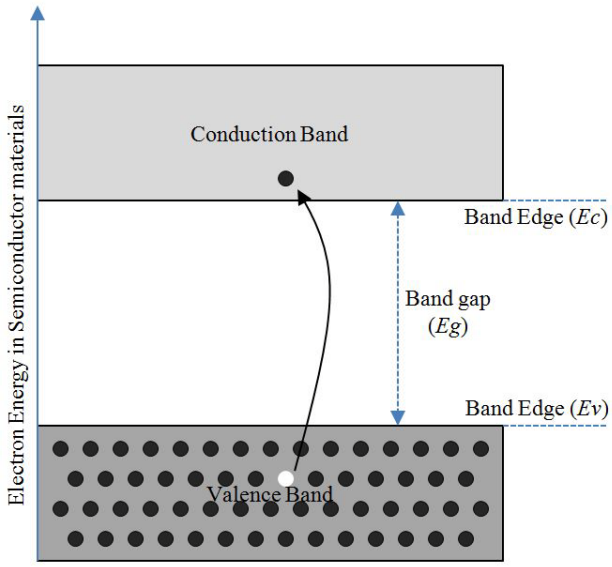

Figure 2.1. Electron energy band diagram of a semiconductor. The energy difference between E_c and E_v is the energy bandgap (E_g).

Generally, the maximum and minimum of an energy band do not lie at the same crystal symmetry point, and therefore have differing values of electron wavevector. For example, in direct band gap semiconductor such as GaAs, the valence band maximum and the conduction band minimum both lie at the Γ symmetry point. In an indirect semiconductor such as Si and Ge, the maximum energy of the valence band occurs at a different value of momentum compared to the minimum energy of conduction band.

The momentum of a photon is related to its energy by

$$p = \frac{E}{c} \quad , \qquad (2.1)$$

where, p is the momentum, E is the photon energy, and c is the velocity of the light, $c = 3 \times 10^8$ ms^{-1}. For photons in or near to the visible range, their energy is ~1 eV, and their momentum is therefore small in comparison to the zone edge wavevector in a semiconductor crystal. Optical transitions are therefore nearly vertical in energy versus wavevector diagrams. Common semiconductors and their energy band gaps are listed in Table 2.1.

Table 2.1. Band gap energies of semiconductor materials [16].

	Material	**Direct / Indirect Bandgap**	**Band Gap Energy at 300 K (eV)**
Elements	C (diamond)	Indirect	5.47
	Ge	Indirect	0.66
	Si	Indirect	1.12
	Sn (grey)	Direct	0.08
Groups III-V compounds	GaAs	Direct	1.42
	InAs	Direct	0.36
	InSb	Direct	0.17
	GaP	Indirect	2.26
	GaN	Direct	3.36
	InN	Direct	0.70
Groups IV-IV compounds	α-SiC	Indirect	2.99
Groups II-VI compounds	ZnO	Direct	3.35
	CdSe	Direct	1.70
	ZnS	Direct	3.68

If the energy of a photon exceeds the bandgap energy, the absorption of that photon can produce an electron-hole pair.

The rate of the generation of electron-hole pairs in the indirect process is lower than the direct process. It is more obvious in the recombination process because the photon can be generated more efficiently for the direct bandgap material than the indirect material, in which a lattice vibration called a phonon is involved to gain or lose momentum. This is one reason why solid state laser devices prefer alloy compound materials based on a direct bandgap, for example GaAs, due to its strong optical interactions.

From Fig. 2.2 which illustrates the three optical transitions in a semiconductor material, absorption

occurs when an electron moves to a higher energy band by absorbing a photon energy which is equal to or greater than the bandgap energy of a semiconductor. A photon which has $E = E_2 - E_1$ is absorbed by the electron moving from energy level E_1 to E_2. Spontaneous emission occurs when an electron in a higher energy band moves down to a lower energy band. The lifetime of an excited state depends upon the type of the excited state. In some cases, electrons can remain longer in metastable states. Finally, when a photon with an energy equal to the bandgap energy interacts with an electron in a higher energy band, the electron can be stimulated and emits another identical photon, a process called stimulated emission. As a result of photon emission, the electron drops down to the lower energy level, and consequently, an additional photon is created at the end of the process as shown in Fig. 2.2 [17].

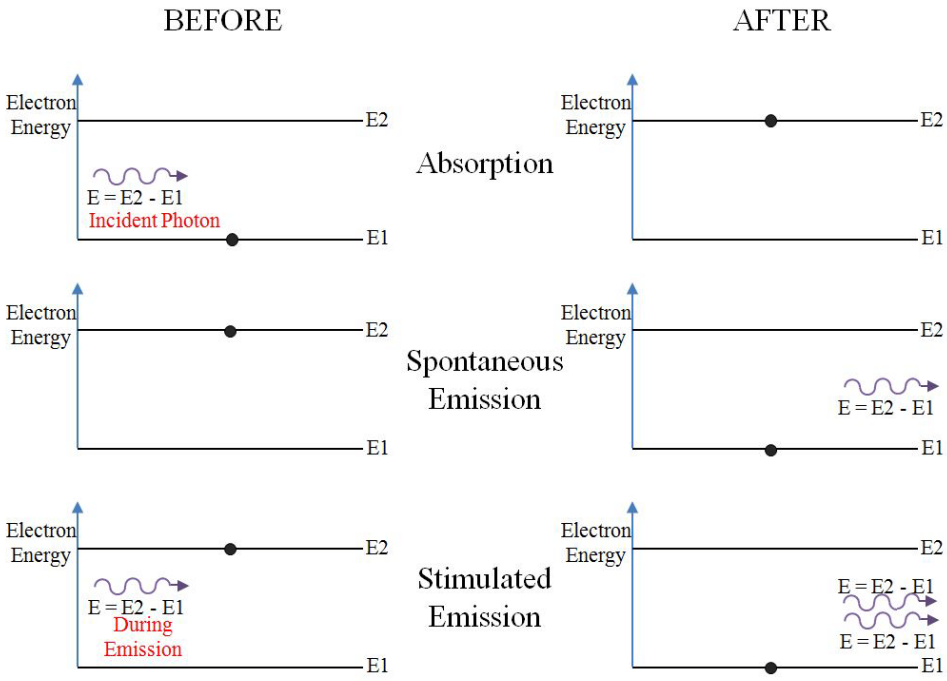

Figure 2.2. Three types of optical transitions in a semiconductor materials [17].

2.2 Silicon PIN photodetectors

The history of photodetectors dates back well over 100 years. In the early 1940s, the basic development of the pn-junction photodiode began. A photodiode is a device that converts light into photocurrent. There are a number of different types of photodiodes to satisfy a wide variety of purposes even though the term 'photodiode' has been used broadly. For example, avalanche photodiodes which can amplify the electric current and Schottky photodiodes formed between the semiconductor and metal to create an asymmetric potential barrier have been utilized for different purposes and applications.

2.2.1. Physics of pn-junction diode

The structure of pn-junction diode is fundamental to the development of a photodiode. The planar type PIN photodiode has become a significant optoelectronic devices which is used in numerous applications. A planar silicon fabrication process is commonly employed to manufacture photodiodes. A one-sided abrupt pn-junction under thermal equilibrium is the normal starting point for most analytical descriptions. From Poisson's equation, the relationships between potential, electric field, and charge are shown in Eq. 2.2.

$$\frac{d^2\phi_i}{dx^2} = -\frac{dE}{dx} = -\frac{\rho}{\varepsilon_s} \quad , \qquad (2.2)$$

where, ϕ_i is the electrostatic potential, ρ is the volume charge density, E is the electric field, and ε_s is the permittivity of semiconductor.

The depletion approximation assumes a rectangular profile of the depleted charge. Since the total charge on each side of the junction is equal, the relationship between the concentration of doped impurities and depletion width can be expressed by,

$$N_A W_{Dp} = N_D W_{Dn} \quad , \qquad (2.3)$$

where N_A and N_D are the doping concentration of acceptors and donors, respectively, and W_{Dp} and W_{Dn} are the depletion widths of p-side and n-side of the junction, respectively.

Uncompensated donor and acceptor ions create fixed charges for establishing the depletion region electric field. This field is referred to as the built-in field. Between the edges of the depletion region, there is a difference of potential due to the built-in field. And the corresponding built-in potential or built-in voltage is

$$V_{bi} = V_{th} \ln \frac{N_D N_A}{n_i^2} \quad , \qquad (2.4)$$

where the thermal voltage is, $V_{th} = kT / q$, n_i is the intrinsic carrier concentration, and N_D and N_A are the doping concentrations of n-type and p-type region, respectively.

When impurities are fully ionized, an electric filed is created within the depletion region. Thus, the depletion width for a abrupt junction can be expressed by,

$$W_D = \left[\frac{2\varepsilon_s}{qN_d} \left(\phi_{bi} - V_{bias} - \frac{2kT}{q} \right) \right]^{1/2} \quad . \qquad (2.5)$$

The depletion width also depends on the applied bias voltage as shown.

2.2.2. Operation principle of silicon PIN photodiodes

After the introduction of the pn-junction diode, the PIN photodiode was developed for higher charge collection efficiency, and now various PIN photodiodes are commonly utilized for many photonic applications. The general structure of a silicon PIN photodiode is shown in Fig. 2.3. This structure includes a p-type region, an intrinsic region, a n-type region, and metal electrodes. Silicon PIN photodiodes use an intrinsic or near-intrinsic silicon region as the substrate, and the intrinsic region is commonly denoted by the letter *i* or Greek letters π or ν to indicate a lightly doped region. P-type and n-type regions are created by a doping processes, for instance, high temperature diffusion or ion-implantation process or by an epitaxial growth process. The boundary (or interface) between two regions of p-type and n-type doping is the functional pn-junction. Generally, the p-type region is created by doping with boron, and phosphorus or arsenic is used for doping the n-type region. [18]

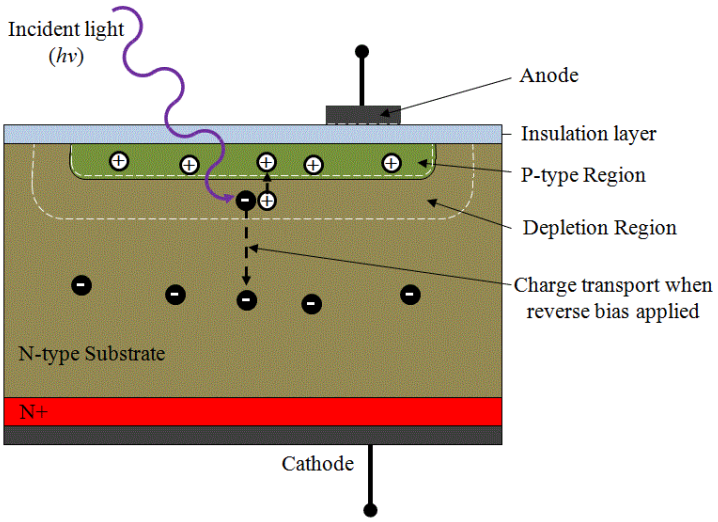

Figure 2.3. General structure of a silicon PIN photodiode

Silicon has a relatively small band gap of 1.12 eV. As illustrated in Fig. 2.4, the energy of an incident photon determines the availability of unoccupied conduction band and occupied valence band states. Accordingly, EHPs generation by the photon absorption can be controlled. Optically generated EHPs increase the conductivity of the semiconductor as shown in Fig. 2.4 [19].

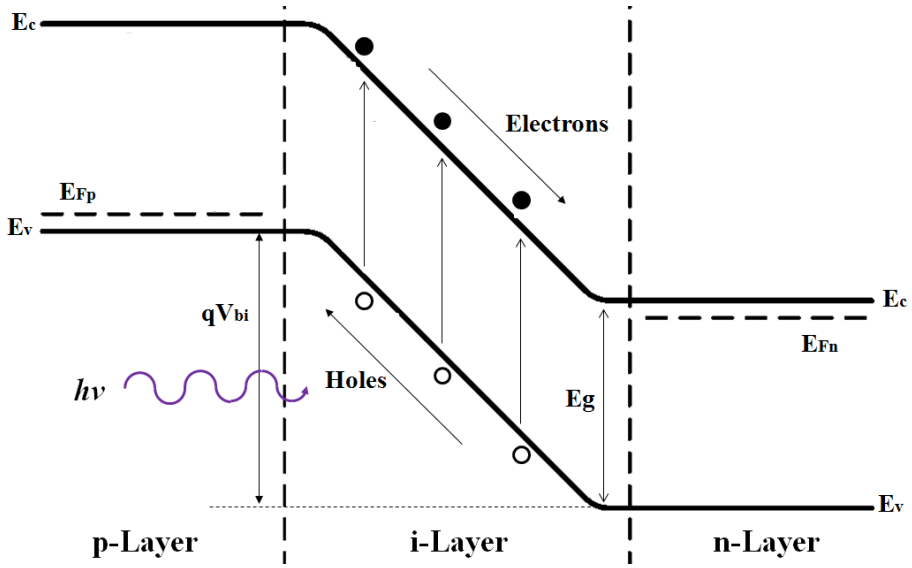

Figure 2.4. Energy band diagram of a silicon PIN photodiode [19].

EHPs generated in the depletion region are separated by the electric filed and collected by the device contacts, creating a photocurrent.

There are three key advantages of PIN photodiode over a regular pn-junction photodiode. First, the higher resistivity intrinsic layer increases the depletion region width such that more volume is available for absorbing incident light. Also, the wider depletion region reduces the junction capacitance and thereby the RC time constant will be reduced, leading to a faster responding device.

2.2.3. Current-Voltage Characteristics of photodiode

The current-voltage characteristics of practical silicon pn-junction diodes include two different behaviors in forward and reverse bias operation modes. When the photodiode operates under forward bias, the current increases exponentially with voltage, while in contrast, a very small saturated current occurs under the reverse bias, and this is the leakage current of photodiode, usually called as dark current in the absence of light as expressed in Eq. 2.6,

$$I_{dark} = I_{sat}\left(\exp^{\frac{qVA}{kT}} - 1\right) \quad , \qquad (2.6)$$

where I_{dark} is the dark current of photodiode, I_{sat} is the reverse saturation current, q is the electron charge, V_A is the applied bias voltage, k is the Boltzmann's constant (=1.38 x 10^{-23} J / K) and T is the absolute temperature.

In addition to the dark current, the breakdown voltage of the junction is another consideration. Specifically, the breakdown voltage can be defined as the voltage at which the dark current becomes

10μA in reverse bias. In particular, PIN photodiodes have a relatively higher breakdown voltage than normal pn-junction diodes because of the presence of the i-region. The breakdown voltage is expressed by,

$$V_{br} = -V_{bi} + \frac{\varepsilon_s \varepsilon_0 E_{br}^{\ 2}}{2qN_d} \ \text{[V]} \quad , \qquad (2.8)$$

where, E_{br} is the critical electric field, which is the maximum ratio of the potential across depletion region to the width of depletion region before breakdown occurs. ε_s and ε_0 are the relative permittivity of silicon and the absolute permittivity of vacuum, respectively, and N_d is donor concentration.

In the case of an asymmetrically doped pn-junction, the depletion region width is more influenced by the more lightly doped side, and the breakdown voltage of the PIN photodiode is mostly determined by the width of the i-region.

2.3 Photoluminescence

Generally, all phenomena involving light emission from matter resulting from photon absorption can be classified as photoluminescence. Photoluminescence in the ultraviolet through visible spectra is comprised of phosphorescence and fluorescence.

Fig. 2.6 illustrates the basic concept of fluorescence and phosphorescence emission. The energy transferred from an absorbed photon promotes one of the electrons in a valence band to move from the ground state to a single excited state. This process is called excitation. Electrons in the excited states will not remain there indefinitely due to their instability, as they tend to spontaneously return back to the ground state by losing energy. At some unknown moment, they return to their original ground state, and this process is called relaxation, decay, or deactivation. During the relaxation process, the energy is released in the form of photon emission. For fluorescence emission, the average lifetime is very short since the electrons in the excited state can remain only for 10^{-5} to 10^{-8} seconds. Light emission decay occurs rapidly after the excitation light is removed. Eq. 2.9 describes the intensity of fluorescence emission, and it is similar to the phosphorescence emission, but with a longer lifetime than that of fluorescence,

$$I = I_0 \exp(-t/\tau) \quad , \qquad (2.9)$$

where I_0 is the initial intensity of fluorescence decay, and τ is the lifetime.

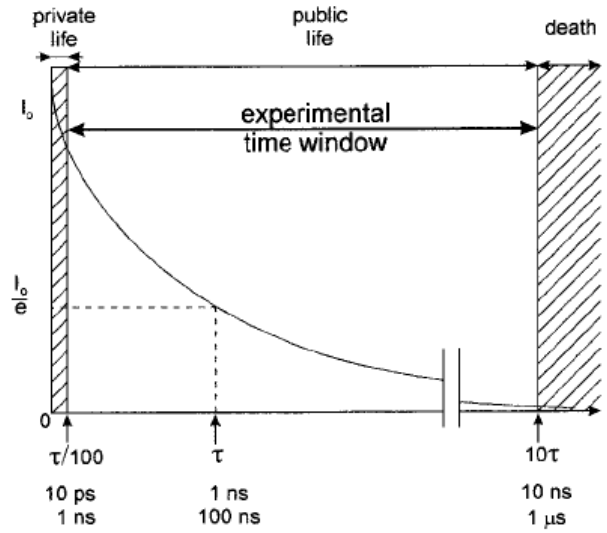

Figure 2.5. Decay of fluorescence as a function of time [20].

However, phosphorescence involves emission between a triplet excited state and a singlet ground state. Also, if some of the molecules in a singlet excited state are transformed into a triplet excited state, phosphorescence emission can also occur.

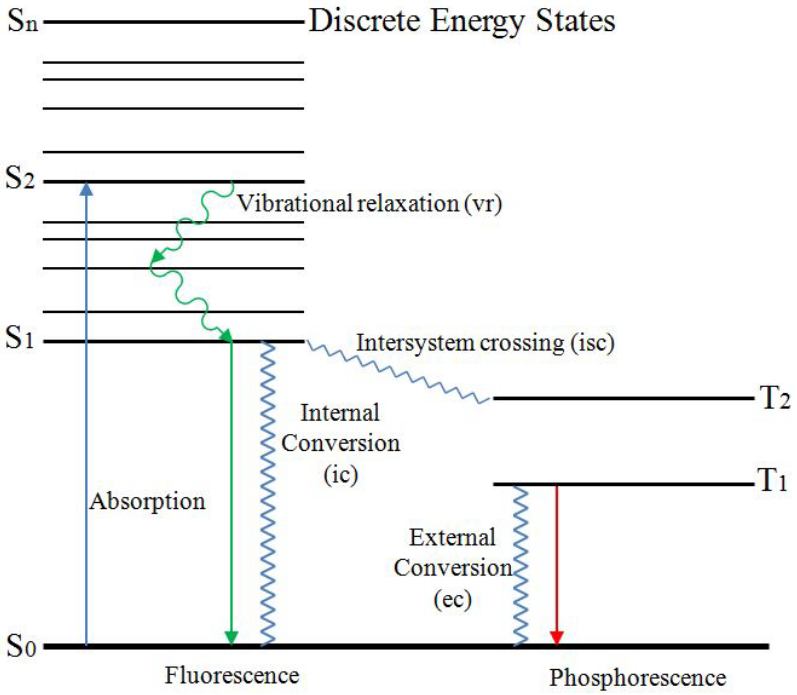

Figure 2.6. Jablonski diagram, where, S = singlet state, T = triplet state, ic = internal conversion, ec = external conversion, isc = intersystem crossing [21].

As Fig. 2.6 indicates, vibrational relaxation called radiation-less deactivation occurs where a molecule in an excited state moves to a lower vibrational energy level by losing energy. The lifetime for

vibrational relaxation (vr) is very short; 10^{-12} seconds or less. Internal conversion (ic) represents a phenomena where a molecule at the lowest excited state passes to the highest vibrational energy of a lower energy state. External conversion (ec) is a similar energy conversion process whereby excess energy is transferred to other energy state. Also, intersystem crossing (isc) is a radiation-less relaxation in which a molecule in the lowest excited state moves into the highest vibrational energy of a triplet excited state. In summary, fluorescence can be observed only if the radiative relaxation is more dominant than the combination of internal conversion and vibrational relaxation. Similarly, phosphorescence emit radiation only by relaxation or intersystem crossing.

In the present work, phosphorescence will be used as a light source for the microfluidic experiments in Chapter 4. Fluorescence materials could not be employed because their shorter decay time would not allow the emission to persist long enough for capture within the channel. The phosphorescent lifetime is much longer and ranges from 10^{-4} to 10^{4} seconds depending on the material. This is long enough for the particles to be excited in one location and transported to another while still emitting.

As discussed in Chapter 1, photoluminescence is isotropic. A photoluminescence detection system should be designed to collect as much of the emitted light as possible. That is a goal of the this sensor development work.

2.4 Characteristics of optoelectronic devices

2.4.1. Noise performance

The minimum limit of the detectable optical signal strongly depends on the noise level of the photodetectors [22]. Several noise sources contribute to the overall noise, and these include thermal (or Johnson) noise, shot noise, bulk and silicon-silicon dioxide interface noise, and flicker noise (1/f noise).

1. Electrical thermal noise (Johnson noise)

Thermal noise in electroincs arises from the random vibrational motion of the carrieres. Macroscopic currents arise from their collective motion. Thermal noise occurs in all resistive materials, and it is spectrally white so that the noise power is proportional to the bandwidth of the measuring system [*Hz*]. Expression of noise power is given in Eq. 2.10,

$$P = \frac{v_n^{\,2}}{R} = 4k_B TB\left[Watt\right], \qquad (2.10)$$

where B is bandwidth in Hertz, R is the resistance, and T is the temperature in Kelvin.

The thermal noise spectral density in watt per Hertz is shown in Eq. 2.11, which was developed by Nyquist and Johnson [23-24],

$$S_{thermal} = 4k_B T\left[Watt/Hz\right], \qquad (2.11)$$

2. Shot noise

Shot noise was originally described by Walter Schottky in 1918 to describe the random fluctuation in the arrival of electrons at the anode of a vacuum diode [26]. In a semiconductor, when electrons and holes cross a potential barrier, a similar noise current occurs. The dark current is in reverse bias,

$$I = I_{sat}\left(\exp^{qV/kT} - 1\right) = -I_d \quad . \qquad (2.12)$$

The root-mean-square (RMS) value of the shot noise current is given by

$$\overline{i_{shot}^{\,2}} = 2qB\left|I_d\right| \quad . \qquad (2.13)$$

Thus, the spectral noise density at the frequency ω is

$$S(\omega) = 2q\left|I_d\right| \qquad (2.14)$$

where *I* is the average DC current created by the electron stream.

The noise spectral density is frequency independent, which means shot noise is white. Unlike thermal noise, it depends upon the bias condition because it depends directly on the average DC current *I* as shown in Eq. 2.14. Moreover, shot noise is usually the dominant noise source in a reverse biased photodiode.

3. Noise from defects in semiconductors (bulk defects / interface traps)

At the silicon-silicon dioxide interface, interface traps can be a source of undesired noise signals produced by randomized trapping and de-trapping of carriers.

The density of traps at the silicon-silicon dioxide interface can evaluated by using a high frequency C-V measurement using Terman's method [27]. In particular, since the photodiode of this work was fabricated using a Bosch deep reactive ion etch (DRIE) process, its noise level could be more affected by traps at the silicon-silicon dioxide interface than through other possible noise sources. A study of the relationship between noise and various DRIE processes has been reported by Nakamura *et al.* [28].

Bulk lattice structural defects, such as dislocations, in a semiconductor are another potential noise source [19]. These can be created by ion implantation steps which are not fully annealed out. Because the photodiode process of this work does not use ion implantation, this is not a concern.

4. 1/f Noise

1/f noise is the most dominant noise source for low frequencies. Theoretically, two major models of

1/f noise have been developed, which are the surface model developed by McWhorter in 1957 [29] and the bulk model developed by Hooge in 1969 [30]. Low frequency optical instrumentation is particularly affected by 1/f noise, and so the development of devices which minimize this always a goal.

Robert Diémé, (2009) has organized the prior research that address 1/f noise as a function of the fabrication process step. From his dissertation [22], much research has focused on the process dependence of 1/f noise by considering various parameters. For example, Cocheteau *et al.* [31] demonstrated the relationship between annealing time and 1/f noise and recommend an increase in annealing time to minimize 1/f noise. Also, Belier *et al.* [32] recommended reducing the energy for the pre-amorphization and implantation steps to decrease the 1/f noise. In Chapter 4, evidence of the effects of different microfabrication process steps are shown to affect the noise sources of the fabricated devices through their dark current.

Combining all the noise sources, the total noise of the photodiode is,

$$\overline{i_{pd}^{\,2}} = \overline{i_{1/f}^{\,2}} + \overline{i_{shot}^{\,2}} + \overline{i_{thermal}^{\,2}} . \qquad (2.15)$$

2.4.2. Cut-off wavelength and absorption coefficient

The spectral range of a photodiode depends upon the band gap energy difference (E_g) of the semiconductor. Moreover, each of semiconductor has a certain cut-off wavelength for the absorption coefficient ($\alpha_s(\lambda)$). The cut-off wavelength for any semiconductor is,

$$\lambda_c(\mu\text{m}) = \frac{1.24}{E_g(\text{eV})} . \qquad (2.16)$$

From Eq. 2.16 and Fig. 2.7, the cut-off wavelength for the silicon occurs at 1.107 um wavelength, Near the cut-off wavelength, the optical absorption changes dramatically. Fig. 2.7 illustrates the absorption coefficient and absorption depth as a function of wavelength. The absorption coefficient increases as the temperature increases. The 90% absorption depth at 300K increases with longer wavelengths due to the limitation of wave penetration. For instance, at 500 nm wavelength, the penetration depth is about 1.1 um. This is one of reasons why the pn-junction depth should be controlled precisely. In other words, the thickness of the p+ layer of the pn-junction photodiode should be shallower than the absorption depth for the range of wavelengths of the incident light source so that the generation of EHPs can concentrated into the depletion region.

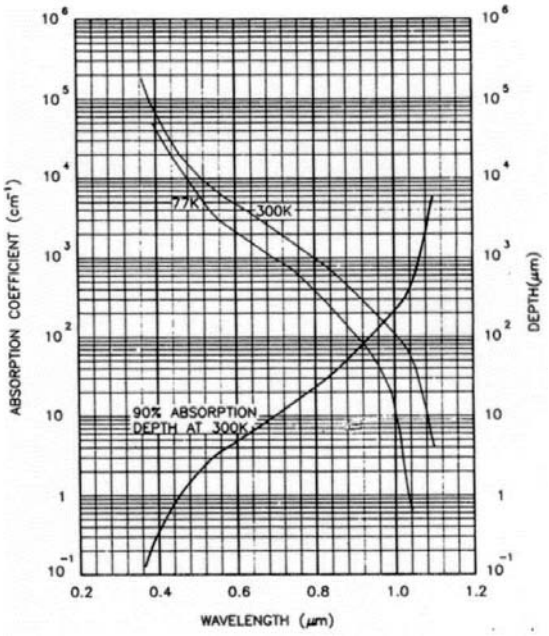

Fig 2.7. Absorption coefficient and absorption depth as a function of wavelength [33].

2.4.3. Absorbed power and reflectance

In the previous section, the absorption of photon was discussed. Optical power or intensity decays exponentially with distance according to Beer's Law,

$$P(x) = P_0(1 - e^{-\alpha_s(\lambda)x}) \qquad (2.17)$$

where $\alpha_s(\lambda)$ is absorption coefficient for a certain wavelength and P_0 is initial incident optical power.

The reflectance (R_f) at the device surface affects the absorbed power. The absorbed power considering reflectance losses at the device surface can be represented by a multiplication of $(1 - R_f)$ to the optical power intensity as expressed in Eq. 2.18,

$$P_{reflected}(x) = P_0(1 - e^{-\alpha_s(\lambda)x})(1 - R_f)\,. \qquad (2.18)$$

2.4.4. Quantum efficiency

One measure for specifying the sensitivity of a photodetector is the quantum efficiency. The quantum efficiency (η) is the ratio of the number of electrons produced to the number of photons captured,

$$\eta_e = \frac{\text{\# of collected EHPs}}{\text{\# of incident photons}} \quad , \qquad (2.19)$$

$$\eta_e = \frac{I_P / q}{P_0 / h\nu} \quad . \qquad (2.20)$$

Generally, the quantum efficiency includes the effects of optical losses by reflection or absorption, which is the external quantum efficiency (η_e). The external quantum efficiency can be improved by techniques which reduce the optical losses, such as anti-reflection coating. The internal quantum efficiency can be determined from the reflection and transmission factors of the device [34],

$$\eta_e = \frac{\text{External Quantum Efficiency}}{\text{1 - reflection - transmission}} \qquad (2.21)$$

2.4.5. Spectral responsivity / radiant sensitivity

Photodetectors are normally optimized for a given spectral region. For a certain wavelength of light, the photocurrent depends on the incident optical power, absorption coefficient, reflectance (R_f) at the device surface, and the applied bias voltage. The primary photocurrent is then

$$I_p = \frac{q}{h\nu} P_0 (1 - e^{-\alpha_s(\lambda)w})(1 - R_f) \qquad , \qquad (2.22)$$

where η is quantum efficiency and h is Planck's constant.

The responsivity ($\Re$) is defined as the ratio of the incident optical power (P_0) in Watts to the output of photocurrent (I_p) in Amperes,

$$\Re = \frac{I_P}{P_0} = \frac{\eta q}{h\nu} \quad \text{[A/W]} \qquad . \qquad (2.23)$$

Since the typical temperature coefficient of responsivity for silicon photodiode at 530 nm wavelength is about 0 %, theoretically, the maximum responsivity for silicon at 300K and 530nm is 0.3 A/W [35]. Also it can be expressed by the density of incident radiant power in W/cm^2 to the photocurrent density in A/cm^2.

Chapter 3
Device Design and Fabrication

In this chapter, an unique but not complicated PIN photodiode design is developed to perform a micro diagnosis experiment. Section 3.1 describes the structure of the Flow-through PIN photodiode (FTPD) and its operation principle. Section 3.2 contains mask design considerations for the fabrication process as well as experimental work. The microfabrication process is discussed in Section 3.3.

3.1 Structures and Principles of Operation

3.1.1 Structures

In past research work microfluidic optical sensors have used commercial photodiodes, which have generally been attached and aligned simply over the top of the fluidic channels [36-38]. One of the critical drawbacks of this method is that it introduces a tremendous optical loss, since the angular field of view (FOV) of the coupled commercial photodiodes is only a few degrees. Diagrammatic cross sections of a commercial photodiode and general methods of collecting fluorescent light for microfluidic optical sensors are shown in Fig. 3.1.

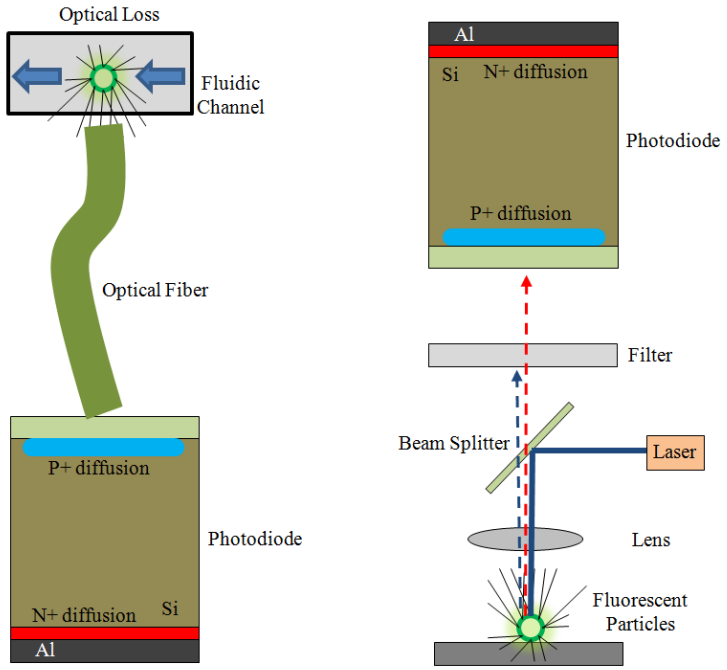

(a) (b)

Figure 3.1. Diagrammatic cross sections of a commercial photodiode and general methods of collecting fluorescent light for microfluidic optical sensors.

Many biosensors using fluorescent detection result in poor sensitivity because the majority of photons

from the isotropic emission of fluorescing molecules are lost as shown in Fig. 3.1 above. An approach to improve the collection efficiency is one of the most significant design factors for the Flow-Through PIN Photodiode (FTPD). The proposed FTPDs have a new geometry in which the microfluidic channel is made by deep reactive ion etching (DRIE), and the fluid flows through the photodiode itself as the photodiodes are embedded into the bottom and wall of the channel.
The fluidic channels have different depths for two process wafers; wafer #1 has 50 μm deep trenches and wafer #2 has 80 μm deep trenches. The cover is coated with a thin chrome film which helps to enhance the sensitivity of photon collection as will be shown in Chapter 3.1. As a result, the proposed new geometry in this study can provide essentially 360° of optical collection with virtually no stray light entry.

the main photodiode structure of the FTPD in this study is the trench channel PIN photodiode. This structure has a trench as a fluidic channel, and a PIN photodiode is embedded into the wall of the trench through the p+ diffusion doping process. Moreover, the trench will be covered by the cover glass deposited chrome film as a high reflective material layer to improve photon collection efficiency of the FTPD as shown in Fig. 3.2 (a).

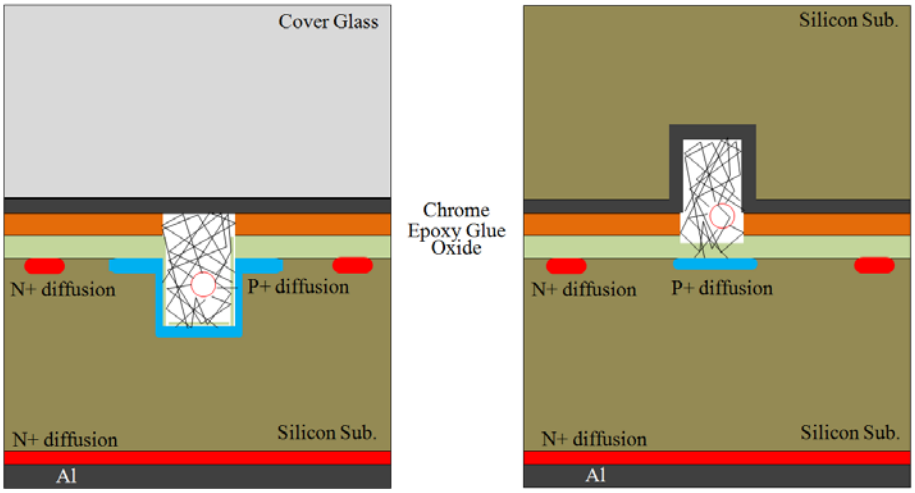

(a) (b)

Figure 3.2. Cross-section view of the Trench(a) and Planar(b) type flow-through PIN photodiode (FTPD) with 360° of optical collection.

In Fig. 3.2, the red circles represent particles, cytometric beads, or living cells. Both concepts provide essentially 360° of optical collection, and these geometries can enhance the photon collection efficiency without any unnecessary stray light entry.

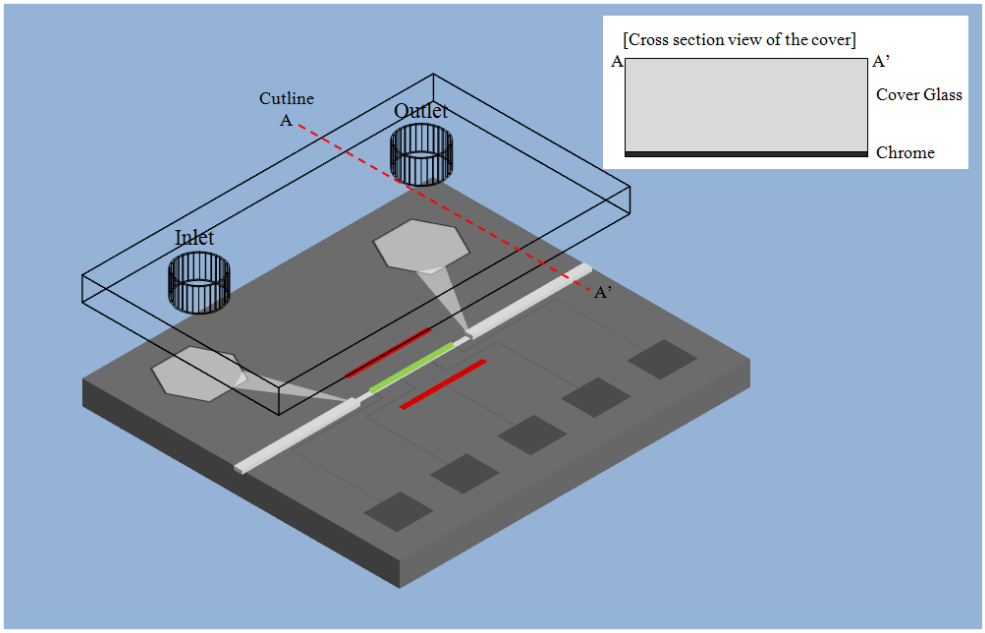

Figure 3.3. FTPD and its reflective glass cover. Cutline of this sensor matches to the diagram shown in Fig. 3.2 (a).

An alternate structure is the planar PIN photodiode. the key difference between the trench type PIN photodiode and the planar type PIN photodiode is the location where the p+ doping is created as an active area of the photodiode. While the FTPD has a p+ diffusion area into the bottom and sidewalls of the trench, p+ dopants were diffused on the surface of the silicon substrate in the case of the planar type PD, more like a regular commercial photodiode. However, its reflective glass cover includes the fluidic channel, as shown in Fig. 3.3. Both type of devices have five 2 mm x 2 mm electrode pads, and two vertical holes in the cover for attachment of the tubing system. One is for the inlet and the other is for the outlet.

In Chapter 4, the electrical and optical characteristics between these two geometrically different sensors will be compared to develop the sensor geometries with the highest sensitivity.

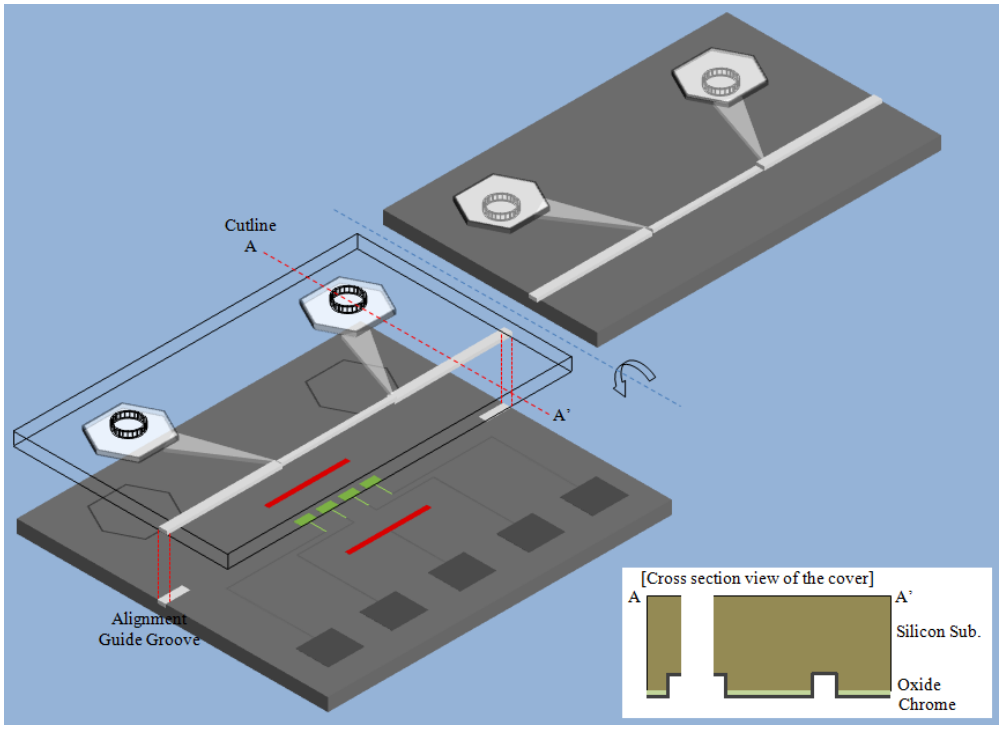

Figure 3.4. Planar type PD and its cover which contains a trench channel, The sensor cutline matches to the diagram shown in Fig. 3.2 (b).

Unlike the structure shown in Fig. 3.3, The alignment guide grooves shown in Fig. 3.4. are used to align the body and cover. To increase the alignment accuracy, alignment guide grooves were created by DRIE. Because the cover is silicon, obviously, it is not transparent. These two tiny alignment grooves are very useful when the body and the cover are assembled. The alignment groove will be discussed further in the Section 3.4.2 on mask design considerations.

3.1.2 Principles of operation

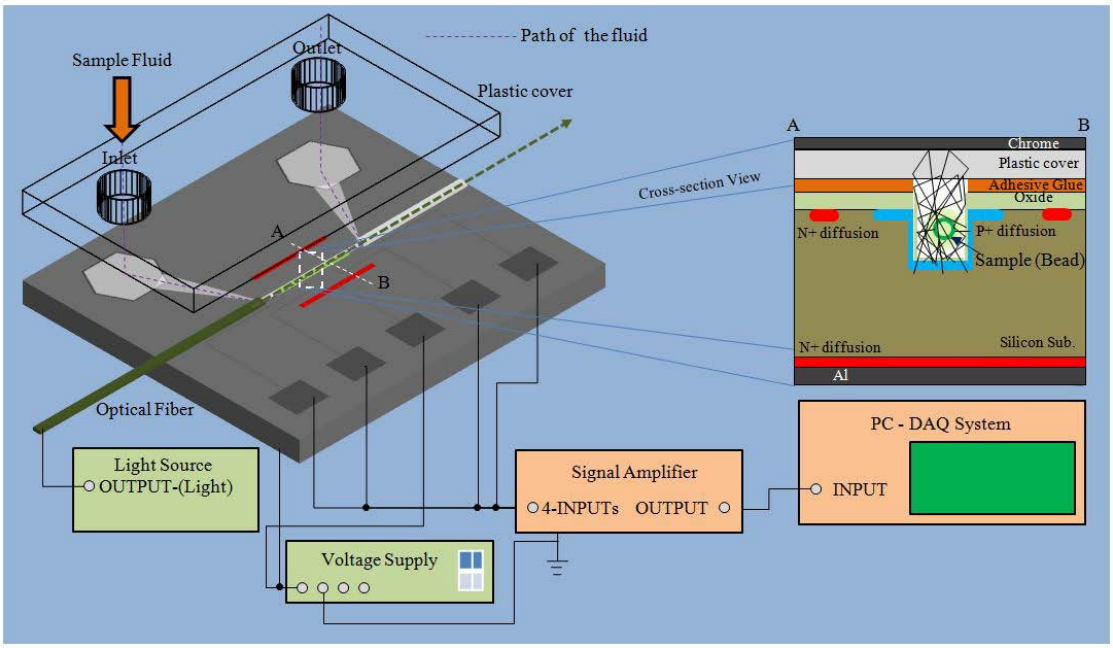

Figure 3.5. Operation of FTPDs for the experiments.

The operation principle of the proposed FTPDs is straightforward and illustrated in Fig. 3.5. The voltage supply provides a constant DC bias for the channel photodiode. While the FTPD is being operated, phosphorescent microspheres will flow through the trench channel from inlet to outlet, driven by a syringe pump system. At the same time, an ultra-violet (UV) light source will excite phosphorescent microspheres via the optical fiber. A laser source coupled optical fiber can be inserted into the optical fiber groove created by the deep reactive ion etching process. Photons created by phosphorescent microspheres create electron-hole pairs in the depletion volume of the FTPD. Generated electrons and holes drift towards the positive and negative electrodes by the depletion region electric field, respectively. Since the collected signal level is very small, the current will be amplified by a transresistance amplifier. Finally, through a data acquisition (DAQ) system, data will be converted into digital numeric values that can be manipulated by a computer.

3.2 Mask Design Considerations

3.2.1 Mask Design Considerations

The Flow-through PIN photodiodes (FTPDs) were fabricated by using a commercial 6-layer photo mask process. The photo masks were constructed as thin film chromium on soda lime glass. The thickness of the soda lime glass was 0.063 inch, and the outside dimensions were 5.00 inches by 5.00

inches square. The photo masks were manufactured by Photosciences Inc., Torrance, California.

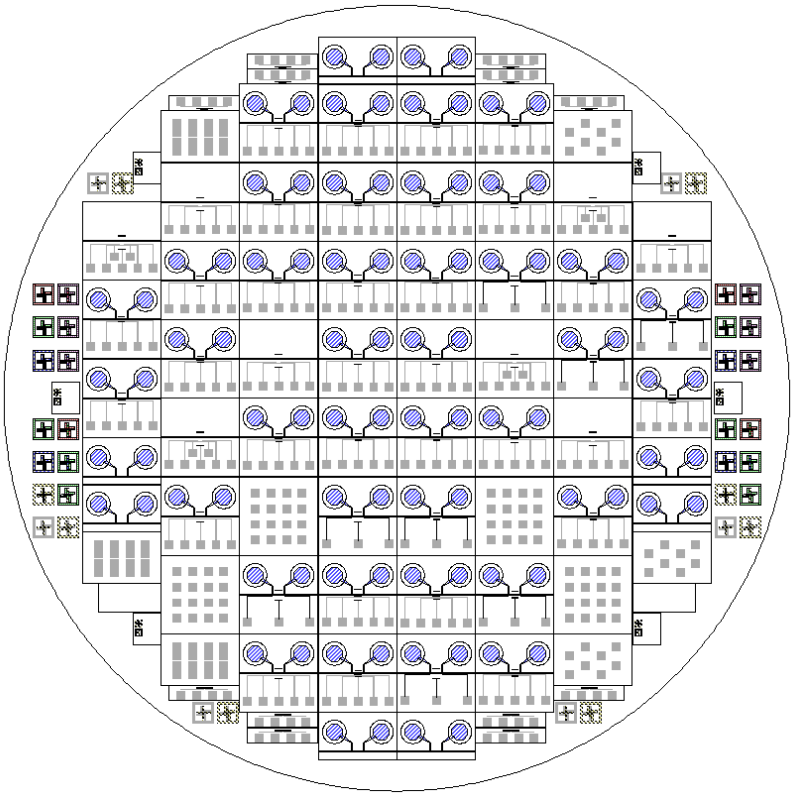

Figure 3.6. Mask Design for the fabrication of FTPDs.

Different types of FTPDs were designed in order to compare different functional features of the structure, as shown in Table 3.1.

Table 3.1 Test patterns to be compared.

Comparison	Note
Planar type PD vs. FTPD	-
50 μm depth of Trench vs. 80 μm depth of Trench	Wafer #1 vs. Wafer #2
Different size of Trench Single and Planar PDs (100×100 μm^2, 150×150 μm^2, 200×200 μm^2)	-

As illustrated in Fig. 3.5, the sensor has grooves to install and align the optical fibers. The width of the groove is 150 μm, and the height is the same as the depth of the trench made by DRIE.

Because most of the test pattern dies have trench channels, arranging each die is one of the significant considerations in the mask design step. a Zigzag arrangement of dies with and without trenches is shown in Fig. 3.7(a). This strategy reduces the risk of accidental wafer breakage by not having the trench run all the way across the wafer.

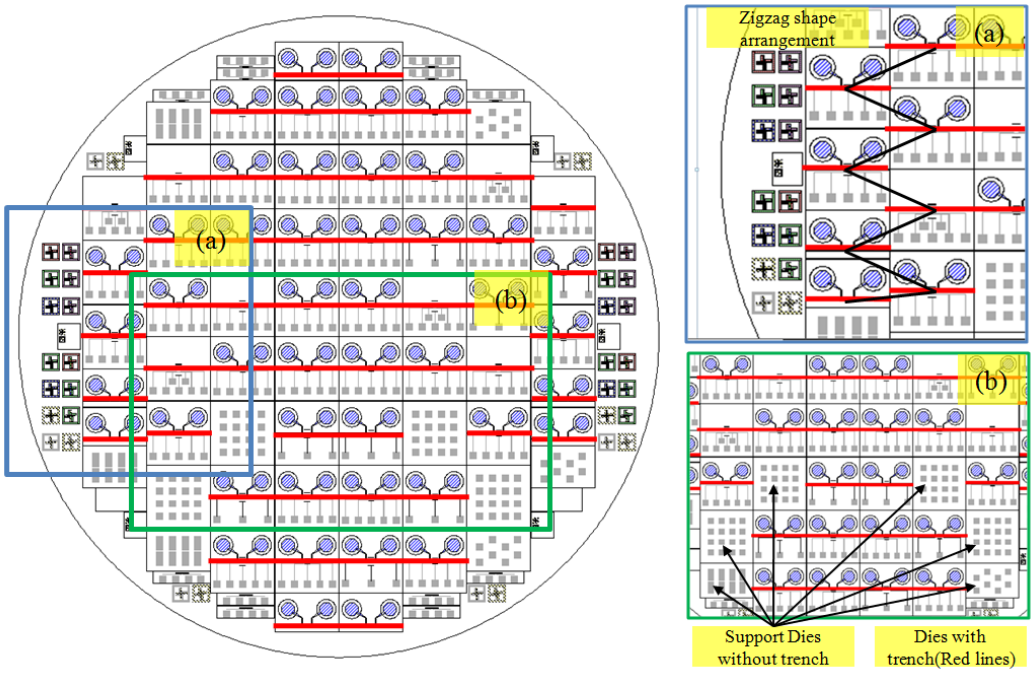

Figure 3.7. Zigzag-patterned arrangement of 10 mm x 10 mm size dies to avoid wafer breakage; Horizontal red lines represent 50 µm or 80 µm depth trench(depends on the wafer number), (a)Zigzag-patterned arrangement, (b)Supporting dies are placed between trench structures to hold near dies in position.

Moreover, each die is braced by placing supporting dies without trench channels in between the dies with trench channels.

As mentioned above, the proposed devices have many deep trenches, and the photolithography process will become difficult after creating the DRIE trenches. Thus, it is necessary that the alignment key for DRIE (Mask #4) and Via (Mask #5), i.e. Alignment key '4-5', should be roughly 6 times bigger than the alignment keys for other steps as shown in Fig. 3.8. This is because the thickness of the AZ4620 photoresist will not be uniform due to those big and deep features. This issue will be covered later in the Section 3.3.3. Table 3.2 shows the names and numbers of each mask layer.

Table 3.2. Mask Layers.

Mask #	**Name**
1	Alignkeys
2	Ndiff
3	Contactpdiff
4	DRIE
5	Via
6	Metal

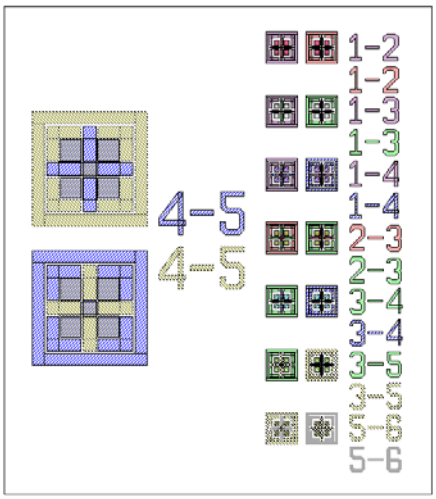

Figure 3.8. Alignment keys for the entire 6-layers mask, alignment keys '4-5' are bigger than the others.

The mask design includes the cover part for the planar type PD, as shown in Fig. 3.9, which has a trench and two holes for inlet and outlet. These two holes can be made by laser or mechanical drilling during the post-process.

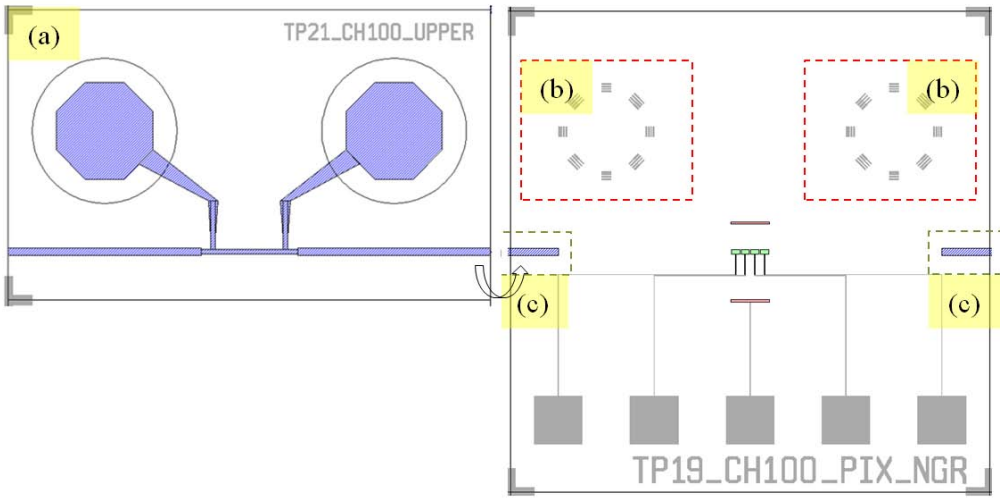

Figure 3.9. Cover of Planar type PDs (a), octagon metal patterns for the ease of alignment (b) and grooves (c).

In the case of the planar type PDs, it may be difficult to align the sensor body and its cover. Octagon boundary metal patterns and alignment grooves and are drawn on the Mask 4 (DRIE) and Mask 6 (Metal), respectively as shown in Fig. 3.9 (b) and (c). These metal patterns and grooves help the cover to be aligned with the planar type PD body much more easily.

Since the ultimate purpose of this FTPD sensor is measuring optical signals under the fluidic test environment, the tubing system should be carefully considered in the mask design step as well. To implement the fluidic test experiment, about half of the entire 1 mm x 1 mm size die area was preserved for the tubing connections. Each test die has 5 metal pads and electrodes. The channel can be divided using laser micromachining so that each electrode and each divided PIN photodiode can be

operated and measured independently as shown in Fig. 3.10, similar to a 1 × 4 pixel detector.

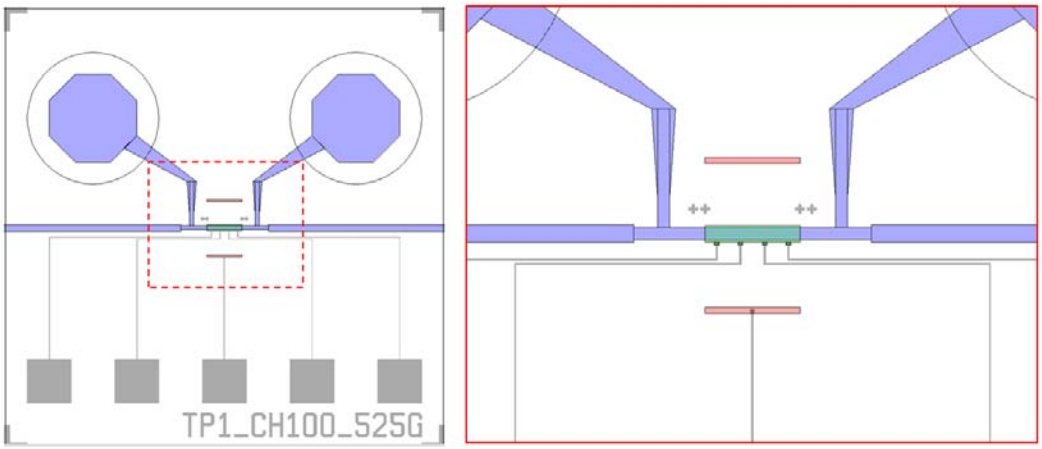

Figure 3.10. Metal electrodes and pads for electrical testing.

In Fig. 3.11, 25 μm wide and 200 μm long cross marks (the gray colored area) are drawn near the p+ doped area (the green colored area). These cross marks are used as a guide to separate the doped regions, as a result of laser cutting. During the laser cutting process, these cross marks help the laser cutter separate pixels more precisely as reference marks.

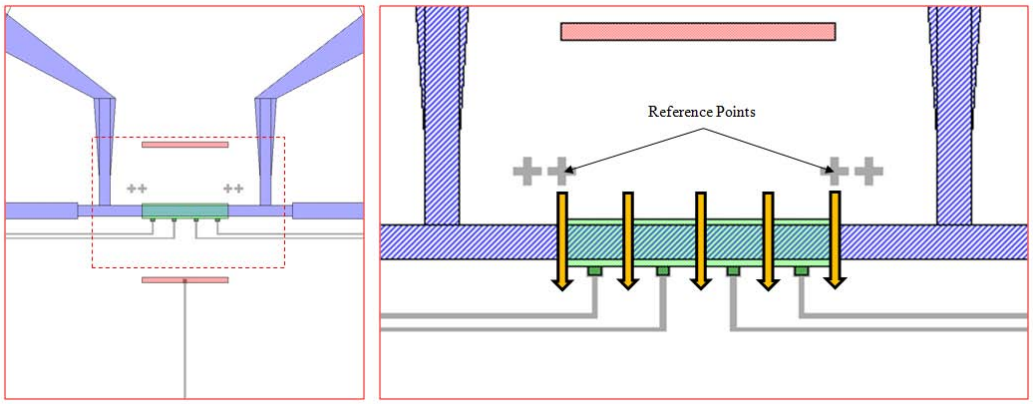

Figure 3.11. Cross marks as a reference point for the laser cutting process.

3.3 Micro-fabrication Processes

3.3.1 Overview

In this section, the entire micro-fabrication process of the FTPDs is discussed. It is necessary to insure that the mask patterns, alignment keys, and polarity of each mask match with the photoresist type. The fabrication process flow is custom designed for the unusual geometry of the FTPD, and involves a considerable efforts in development. This process flow is described step by step. Finally, some problems and their solutions are discussed at the end of this section.

3.3.2 Micro-fabrication process flow

Much research has been carried out to improve the micro-fabrication technology and the characteristics of silicon photodiodes [39-42].

The geometry for the FTPD is surprisingly simple, and requires only three diffusions; one n+, two p+; DRIE etching for the microfluidic channels, and metal contacts for the anode and cathode. However, after completing the DRIE process (50μm and 80μm depth for wafer #1 and wafer #2, respectively), steps that looked simple and easy to fabricate turned out to more challenging due to the topology of the thin films near the deep trenches.

The prototypes were fabricated on 100 mm diameter high resistivity silicon wafers using the tools of the Micro-Fabrication Facility (MFF) at Fluke Hall at the University of Washington, Seattle.

N-type, (100) orientation, single side polished substrates (525 μm thickness, 100 mm diameter, 584 ohm-cm resistivity, phosphorus doped) were used for the fabrication of the FTPDs. Fig. 3.12 illustrates the process flow for the FTPDs.

a. 1.5μm thickness oxide deposition (wet oxidation)

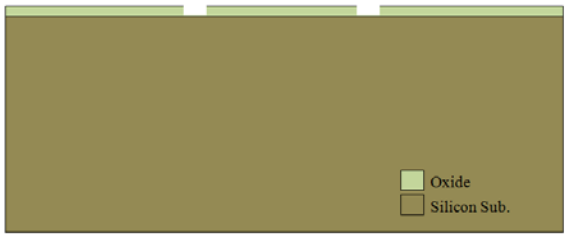

b. 1.5μm thickness oxide etching (dry etching)

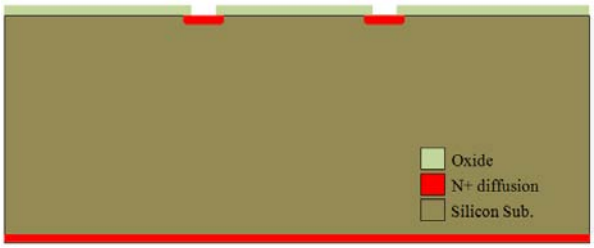

c. Phosphorus high temperature diffusion doping for n+ region (soak temp. 1025deg.C., 60min.)

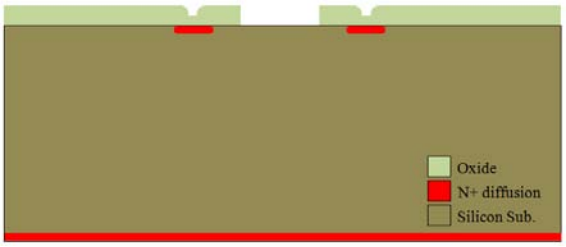

d. 1μm thickness PECVD oxide deposition and oxide etching for the p+ contact area diffusion (dry etching)

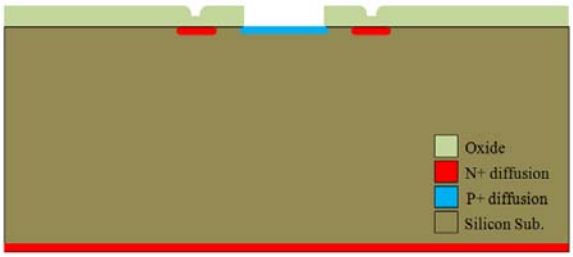

e. Boron high temperature diffusion doping for p+ contact region (soak temp. 1100deg.C., 60min.)

f. 1μm thickness PECVD oxide deposition

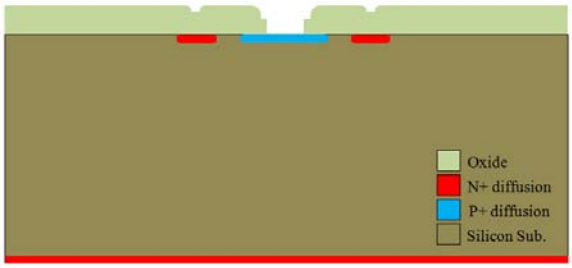

g. Oxide etching for making DRIE oxide mask

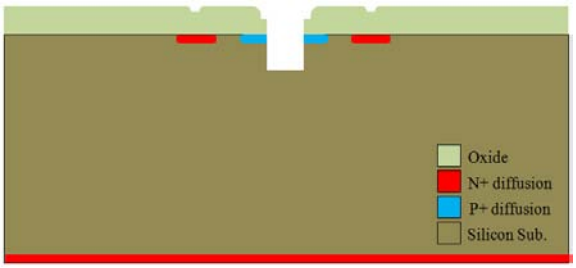

h. Deep reactive ion etching (DRIE) for the channel

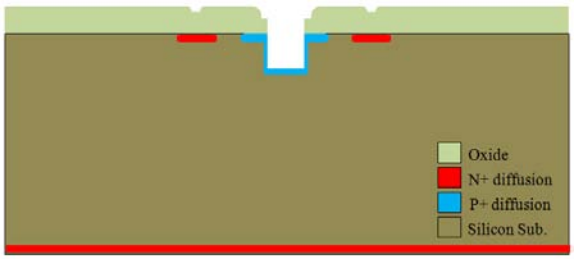

i. Boron high temperature diffusion doping for p+ region onto the surface of the channel. (soak temp. 1000°C., 30min.)

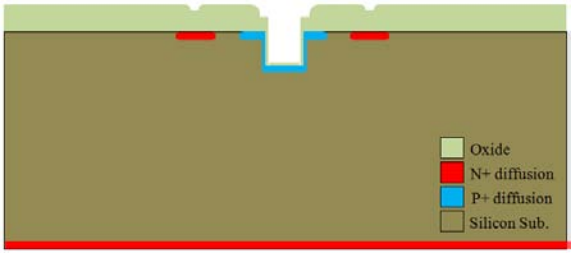

j. 1μm thickness PECVD oxide deposition for passivation layer. (preventing the electrical short during the fluidic experiment)

k. Photoresist coating

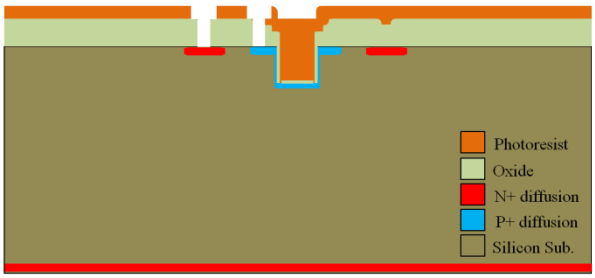

l. Photoresist patterning and oxide etching

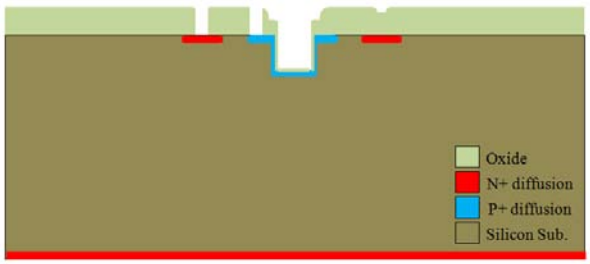

m. Photoresist stripping

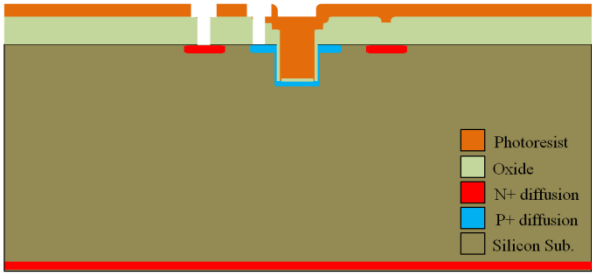

n. Photoresist coating & patterning

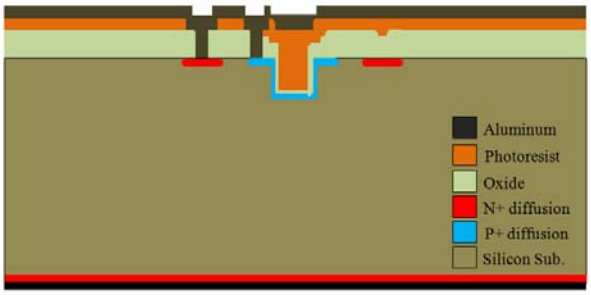

o. Aluminum deposition (for both sides)

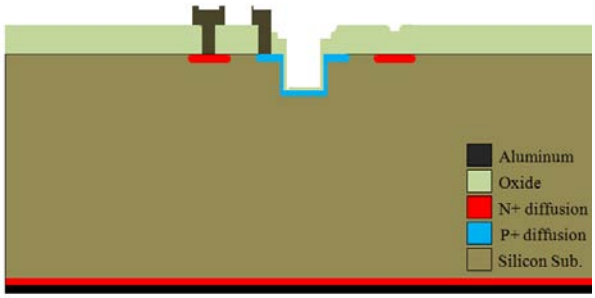

p. Aluminum lift-off and annealing

Figure 3.12. Fabrication flow of the flow-through PIN photodiodes.

First, RCA cleaning was performed with an ammonia hydrogen peroxide mixture (APM); 5:1:1 [vol :

vol : vol] solution of de-ionized (DI) water (H_2O), 30% ammonium hydroxide(H_2O_2), 30% hydrogen peroxide (NH_4OH) followed by a hydrochloric acid hydrogen peroxide mixture (HPM); 5:1:1 [vol : vol : vol] solution of de-ionized (DI) water (H_2O), 32% hydrochloric acid (HCl), and 30% hydrogen peroxide (NH_4OH) at around 80°C for the standard clean-1 (SC-1) and 2 (SC-2), respectively. Basically, SC-1 is used to remove organic residues from the surface of the wafer, and SC-2 is used for removing metallic contaminations from the wafer. This general cleaning method was developed by Werner Kern at Radio Corporation of America's (RCA's) laboratories in the late 1960's, and it became the most common wafer cleaning procedure in the micro-fabrication process [43]. Note that Fig. 3.12 above does not include RCA cleaning and alignment key etching steps.

Initial oxidation was conducted at 1050°C in wet O_2 for 480 minutes to make a high quality hard blocking mask against the high-temperature phosphorus diffusion doping. After the wet oxidation process, patterning of the silicon dioxide layer was carried out by a dry etching system, the Vision RIE tool (from Advanced Vacuum). Then, a high concentration n-type dopant was diffused into the silicon surface. The temperature and diffusion time (or drive-in time) were 1025°C and 80 min, respectively. Generally, the diffusion process is carried out at a high temperature of about 950°C to 1250°C in a quartz furnace tube with dopant gases or solid source wafers such as planar diffusion source (PDS) wafers. For this study, PDS wafers are used as solid diffusion sources to simplify fabrication procedures and save time.

The process using PDS wafers is one of the best methods for phosphorus or boron diffusion. There are several advantages of the solid source diffusion method. It requires no additional equipment to convert the dopants from a gas phase or to meter them into the furnace tube, reducing the capital expense. Furthermore, this process shows improved yield and reduces process faults since it is based on precision chemical principles which make for predictability and repeatability [44]. A proper dopant, such as boron or phosphorus for making p-type or n-type doping regions can be diffused into the silicon lattice in the high temperature ambient. PDS wafers need to be arranged on a specially designed quartz boat. This quartz boat has an unique spacing and groove width so that the solid source wafer and processing silicon wafer can be placed in the proper order.

PDS phosphorus wafers (PH-1025 model, from Saint-Gobain Advanced Ceramics, PA) were used for the n+ diffusion doping process. Brand new PDS phosphorus wafers were first annealed at 1025°C in an ambient of 100% N_2 for 4 hours to remove entrapped moisture. Table 3.3 briefly shows the target conditions for the phosphorus diffusion doping process. To make a good ohmic contact, a high concentration of phosphorus and a long diffusion time were applied as shown in the Table 3.3. Phosphorus has a higher solid solubility in silicon than boron, and a surface concentration range of 1.0×10^{21} atoms/cm^{23} can be achieved during a high-temperature diffusion process.

As Fig. 3.12 shows below, PH-1025 PDS phosphorus wafers produce about a 2.5 ohm/square sheet resistance at 1025°C and 80 minutes soaking time, according to the material data sheet from Saint-Gobain Advanced Ceramics [44].

Table 3.3. Target conditions for the phosphorus diffusion doping.

Conditions	Target Values
Temperature	1025°C
Soaking Time	80 min.
Target Dose	1.4×10^{16} atoms/cm^2
Sheet Resistance	2.5 ohm/square (as low as possible)
Junction Depth	2.7 µm

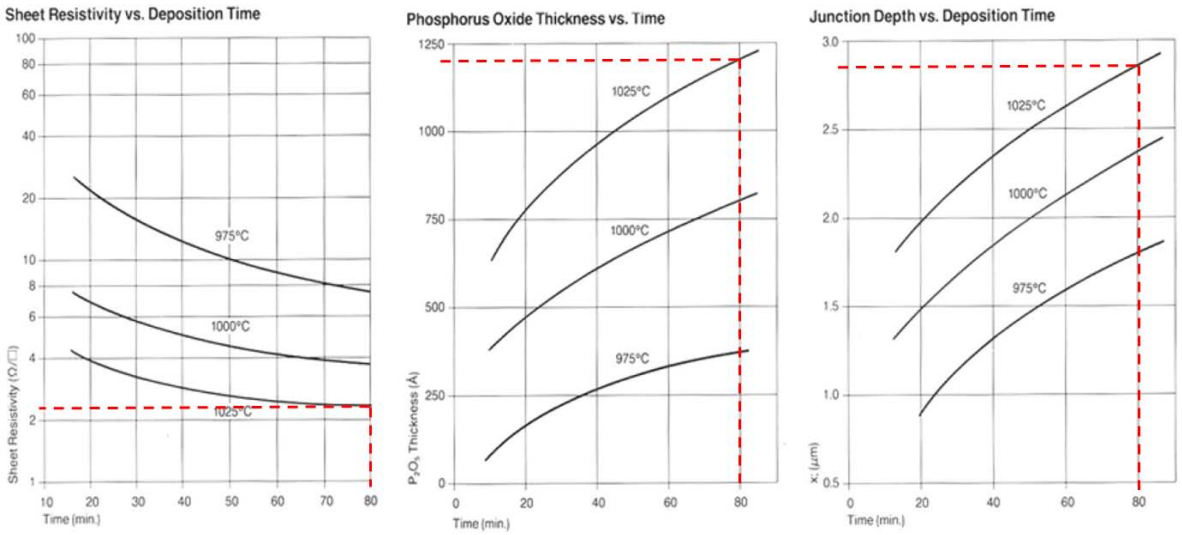

Fig 3.13. Performance data; sheet resistivity (ohm/sq.) vs. time (min) (left), P_2O_5 thickness (angstroms) vs. time (min.) (center), junction depth (µm) vs. time (min.) (right) for model 'PDS Products N-type Grade PH-1025', red lines stand for the desired and targeted diffusion time [44].

From the target diffusion temperature and soaking time (1025°C and 80 minutes), the sheet resistance, the thickness of the phosphorus-oxide (P_2O_5) and the junction depth were predicted. Also, the sheet resistance was measured by a Four-Point-Probe tool (FPP-5000) after the deglazing process.

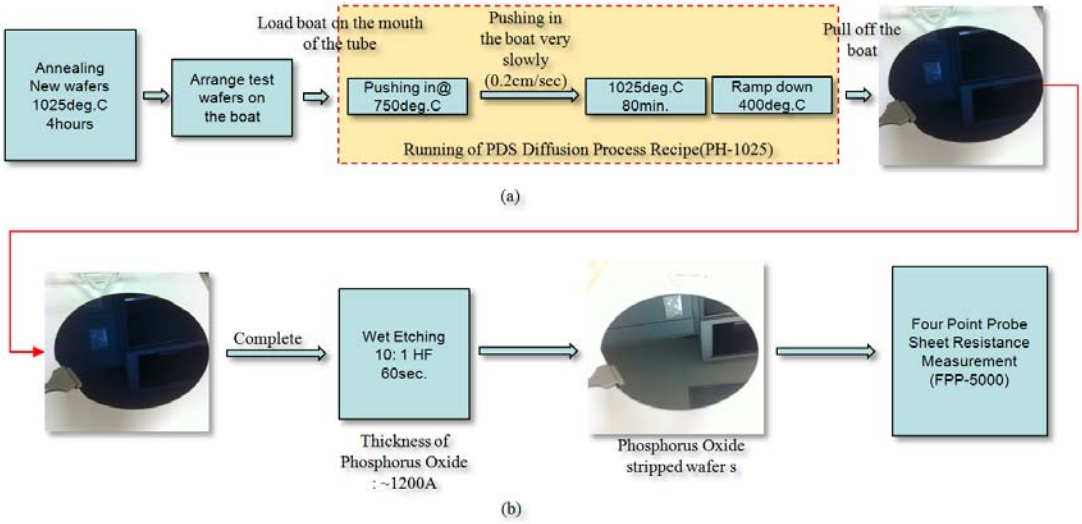

Figure 3.14. Diagram of the n+ diffusion doping procedure and the sheet resistance measurement; (a) Steps of the phosphorus diffusion process, (b) Steps of deglazing process for the sheet resistance measurement.

The PH-1025 phosphorus solid source used in this work is a ceramic wafer containing 60 % of ZrP_2O_7, 30% SiP_2O_7 and 10 % of SiO_2 [45]. At diffusion temperature, the active component decomposes to form P_2O_5 vapor, which evolves from the source by direct volatilization. During the infinite-source diffusion (or pre-deposition) step, a thin P_2O_5 glass layer evaporates slowly from the ceramic wafer and condenses on the silicon wafer. P_2O_5 glass layer on the silicon wafer decomposed to phosphorus atoms and SiO_2. Equation 3.1. describes chemical reaction of the thin layer of P_2O_5 phosphorus for the diffusion into the silicon. After the n+ diffusion doping process, the remaining P_2O_5 thin film and additionally created SiO_2 on the wafer surface was removed.

$$2\,P_2O_5 + 5\,Si \;\Leftrightarrow\; 4\,P + 5\,SiO_2 \qquad (3.1)$$

To remove the remaining P_2O_5 and SiO_2 layer, 10:1 diluted HF etching was carried out for 60 seconds after cooling down the wafers. P_2O_5 obstructs the four point probe (FPP) tool to measure precise values of the sheet resistance, since it is an insulator. By immersing the wafers into 10:1 HF, P_2O_5 was stripped completely. Fig. 3.15 indicates the sheet resistance measurement using the FPP tool and its test results are illustrated in Fig. 3.16. Four test wafers are provided a sheet resistance in the range from 3.2 to 3.8 ohm/square, as shown in Fig. 3.16. Measured values are not exactly the same as the sheet resistance values from the data sheet; however, these are still within the range to make perfectly good ohmic contacts on both sides of the silicon substrates. As Fig. 3.15 shows, sheet resistance values were measured for five points; center, top, right, bottom, and left, which are 3 cm away from the center of the silicon substrate. The measured values indicate a good uniformity of the sheet resistance. These wafers showed sheet resistance standard deviation (Std.) from 0.032 to 0.089

Ω/square and the uniformity in the range of 97.6 % to 98.9 % as shown in Table 3.4 below.

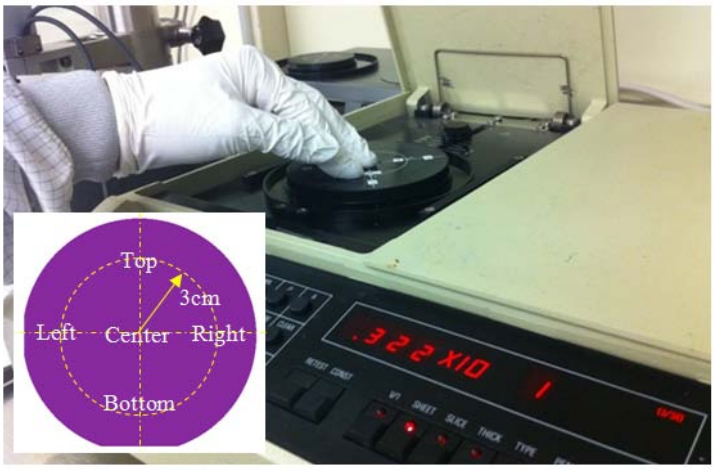

Fig 3.15. Sheet resistance measurement using a four point probe (FPP).

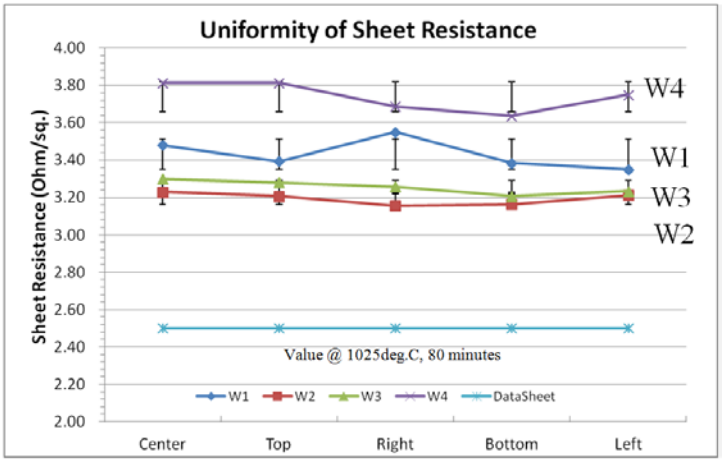

Fig 3.16. Uniformity of the sheet resistance for the n+ diffusion doping process, the light-blue line indicates the sheet resistance value that the datasheet [44] provides. 'W#' represents test wafer number (#).

$$Uniformity(\%) = 1 - \frac{Std.}{Mean} \qquad (3.2)$$

Table 3.4. Calculated uniformity value of n+ (Phosphorus) doping test wafers.

Wafer #	Std.	Mean	Uniformity (%)
1	0.089	3.43	97.61
2	0.032	3.19	98.99
3	0.037	3.26	98.87
4	0.078	3.74	97.91
Datasheet	-	2.50	-

Next, after the n+ diffusion doping process, an additional 1μm thickness PECVD oxide was deposited

and selectively etched using the Oxford Plasma Lab PECVD tool and the Vision RIE tool, respectively. In order for the oxide layer to better protect the boron diffusion, an additional oxide layer was deposited over the existing wet oxide layer without any oxide stripping step.

The p+ contact diffusion doping process was carried out with the target conditions as shown in Table 3.5.

Table 3.5. Target conditions for the boron diffusion doping.

Conditions	**Target Values**
Temperature	1050°C
Soaking Time	60 min.
Target Dose	6.0×10^{15} atoms/cm^2
Sheet Resistance	2.5 ohm/square (as low as possible)
Junction Depth	2.2 μm

The purpose of the p+ contact diffusion doping is to create a p+ well for the contact. For doing this step, it was one of key design consideration to establish the misalignment margin, since trenches will be made near the p+ contact well as shown in Fig. 3.12(e). Boron diffusion doping was carried out through the solid source diffusion method with Grade BN-HT wafers from Saint-Gobain Advanced Ceramics. The BN-HT wafers were first oxidized in the furnace tube at 1000°C for 30 minutes. This initial oxidation process grows a B_2O_3 thin glass layer on the surface of the boron nitride solid source wafers. This layer acts as the boron dopant source during subsequent steps. A surface reaction with the created boron trioxide allows boron atoms to diffuse into the silicon surface in the high-temperature furnace [46].

$$2\,B_2O_3 + 3\,Si \Leftrightarrow 4\,B + 3\,SiO_2 \qquad (3.3)$$

During the photo lithography process for the p+ contact diffusion doping, the misalignment margin will be an significant factor to guarantee proper electrical contacts. If there is no extra marginal area for developing the contact via holes, the processes following the DRIE step will be difficult to perform. Thus, a 5 μm margin is applied to the photo mask patterns for these regions.

Table 3.6. Sheet resistance (Unit: Ohm/sq.).

	Trial #	Center of the wafer
Test wafer #1	T1	7.33
	T2	7.26
	T3	7.31
	Average	**7.30**
Test wafer #2	T1	7.27
	T2	7.24
	T3	7.22
	Average	**7.24**
Test wafer #3	T1	6.75
	T2	6.62
	T3	6.63
	Average	**6.67**

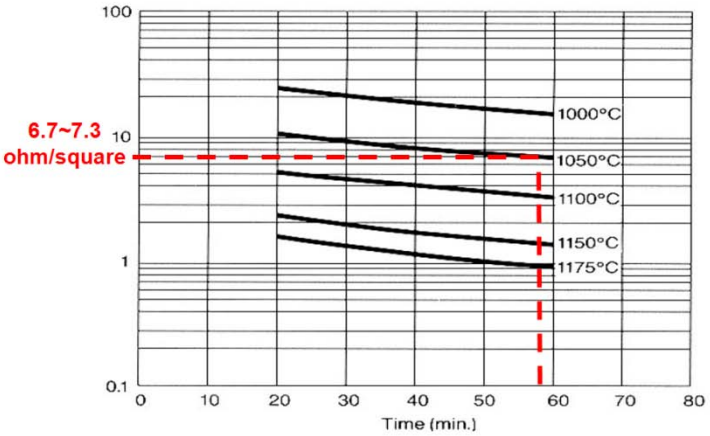

Figure 3.17. Sheet resistance vs. diffusion time [46].

The most important feature of the proposed structure is that PIN photodiodes are embedded into the trenches which are used as fluidic channels. To create 50 μm and 80 μm deep trenches, a deep reactive ion etching (DRIE) process was performed. The remain oxide layer was used as a blocking hard mask during the DRIE process.

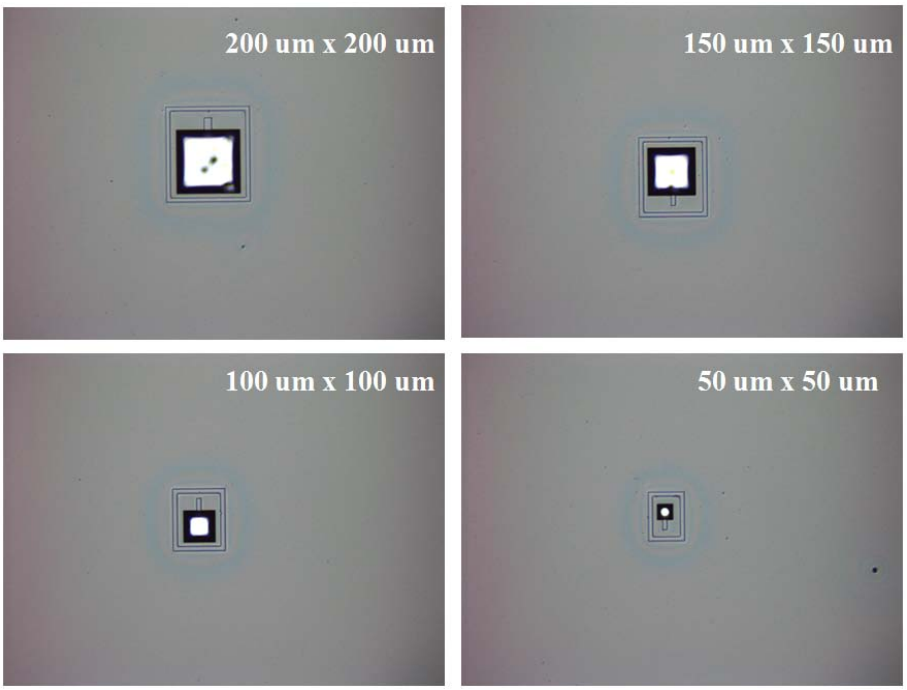

Figure 3.18. Microscope images of etched single trench photodiodes by DRIE.

To evaluate the characteristics of the photodiodes themselves, 200 μm × 200 μm , 150 μm × 150 μm, 100 μm × 100 μm, 50 μm × 50 μm size planar and trench photodiodes were designed and fabricated. Fig. 3.18 shows microscope images of these etched single trench photodiodes.

Immediately following the DRIE process, a second solid source boron diffusion doping was performed without additional photolithography, a 'self-aligned step'. Boron was diffused into the bottom and walls of the trenches. Table 3.7 gives process targets and conditions of the second solid source boron diffusion doping.

Table 3.7. Process goals and conditions of the 2nd boron diffusion doping.

Parameters	**Value**
Desired Junction depth	1 μm
Desired Sheet resistance	20 ohm/sq.
Desired dose of Boron impurity	6.0×10^{15} atoms/cm^2
Diffusion Temperature	1000°C
Diffusion Time	30 min.
Ambient	N_2, O_2

After deglazing the B_2O_3 glass thin layer on the wafer surface with 10:1 HF for 2 minutes, the sheet resistance of the test wafer was measured at four selected positions with the FPP tool. the desired junction depth of 1 μm was achieved through the process.

Table 3.8. Results of the 2nd Boron diffusion doping process.

Results	**Test wafer for 2nd Boron diffusion**				
Measurement Environment	Deglazing remaining B_2O_3 glass layer (10:1 HF for 2 minutes)				
Positions	Center	Top	Right	Bottom	Left
Sheet resistance (ohm/sq.)	22.4	23.1	23.4	22.1	20.7
Average	22.34 ohm/sq.,				
X_j	~ 0.95 μm from PDS material data sheet [46]				

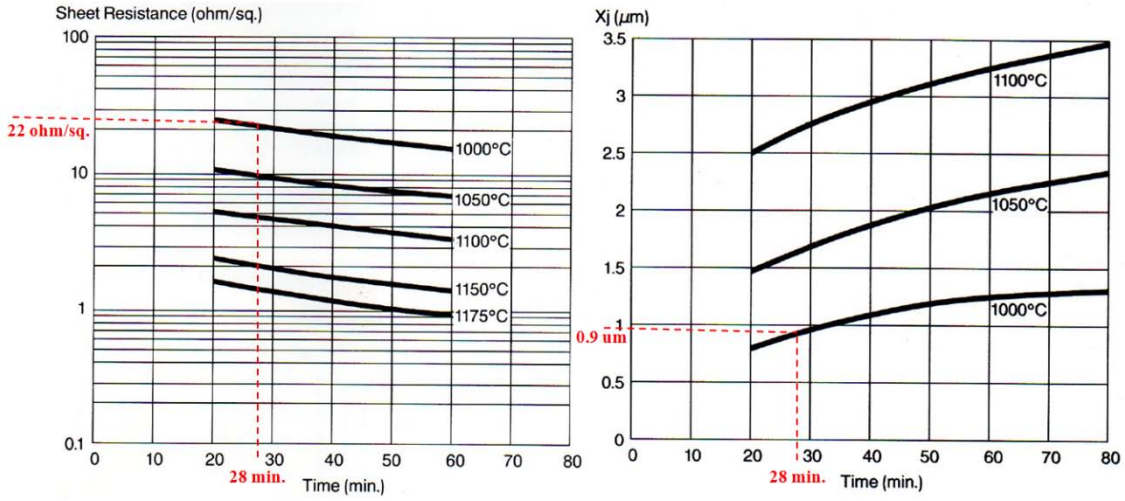

Figure 3.19. Sheet resistance vs. diffusion time (Left), Junction depth vs. diffusion time (Right) [46].

A PECVD oxide was deposited to a thickness of 1μm for two wafers. It was not easy to check precisely whether the PECVD oxide was fully covering the walls of trenches with using the microscope, but it appeared that an oxide layer was covering the entire area inside the trenches and over the wafer surface. Scanning electron microscopy (SEM) provided accurate verification that the deposited oxide covers the entire area of inside trenches. Moreover, by checking the color of oxide layer, its thickness can be estimated as shown in Fig. 3.20. Enhancement of certain wavelengths in the reflected light is caused by constructive interference, and the color of wafer corresponds to the enhanced wavelength. Additionally, an ellipsometer could have be used to accurately determine the film thickness. A mechanical surface profilometer was used to determine the film thickness, X_0.

$$2X_0 = \frac{k\lambda}{n}, \tag{3.4}$$

where, X_0 is the oxide thickness, n and k are representing the refractive index and any integer number, respectively.

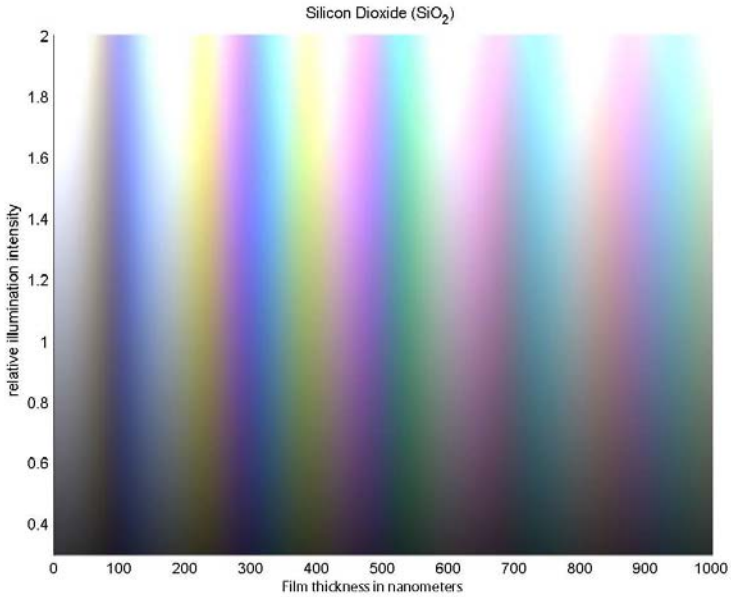

Figure 3.20. Color chart of silicon dioxide as a function of its thickness [47].

From the microscope images in Fig. 3.21, the oxide has been deposited uniformly over the entire wafer surface; however, the oxide inside the trenches shows some non-uniformity. This phenomenon is natural because the angle of the trench wall is not ideally perpendicular to the bottom of the trench as well as trench is not wide enough in order for ambient and plasma to generate the same chemical reaction in the PECVD chamber uniformly as over the wafer surface. In the fluidic testing, the entire trench needs to be electrically isolated by the PECVD oxide layer.

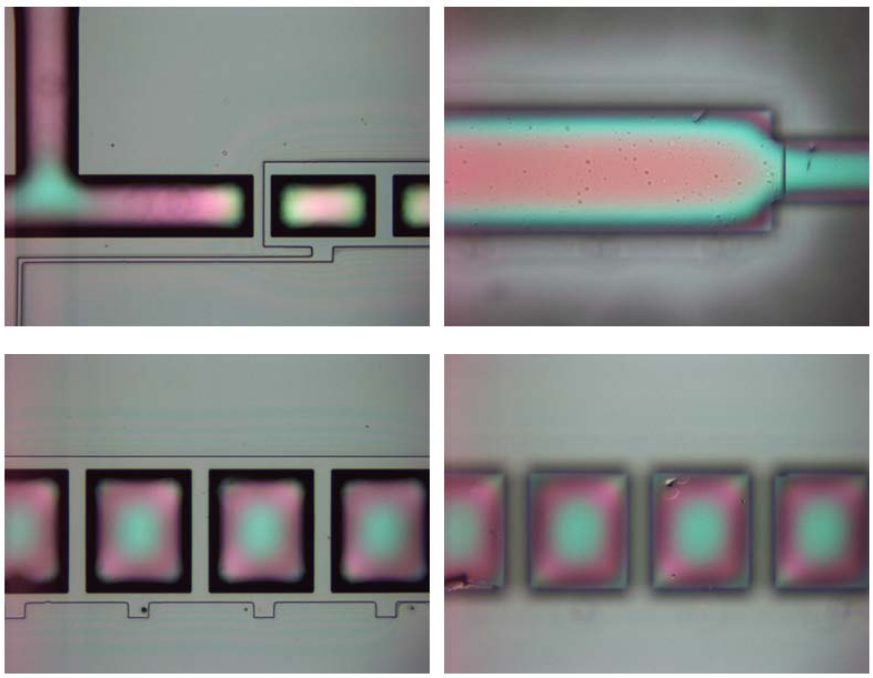

Figure 3.21. Result after the 1 μm thickness PECVD oxide deposition. Top right and bottom right pictures are focusing on the bottom of the trench using microscope.

After the DRIE process, the photolithography process recipe was completely changed to handle the 50 μm and 80 μm depth of deep trenches. As Fig. 3.22 illustrates, double photoresist (PR) spin coating and a higher viscosity positive photoresist (AZ4620) were both required.

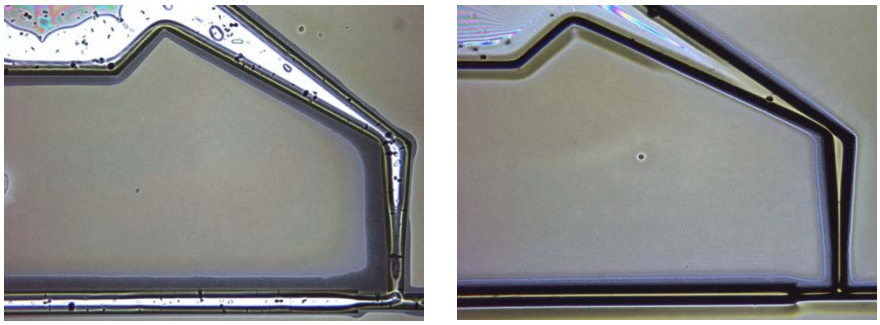

Figure 3.22. Single (a) and Double PR coating (b) results; AZ4620 positive photoresist was used.

As shown in Fig. 3.22 (a), a single spin photoresist coating did not work following the DRIE process due to the deep trenches which trap the photoresist non-uniformly and restrict proper spin spreading of the photoresist. Fig. 3.22 (b) shows a deep trench pattern covered properly by photoresist through the double PR coating recipe of the Table 3.9.

Table 3.9. Double PR coating and baking condition.

	Wafer 1	**Wafer 2**	**Note**
Trench depth	50 μm	80 μm	-
Coating Method (AZ4620)	Double Coating	Double Coating	~22μm thick total
Spin conditions	Spread - 300rpm, 150rpm/sec, 3sec Spin - 1800rpm, 1250rpm/sec, 20sec Stabilization - 1600rpm, 1800rpm/sec, 120sec	Spread - 300rpm, 150rpm/sec, 5sec Spin - 1700rpm, 1250rpm/sec, 20sec Stabilization - 1600rpm, 1800rpm/sec, 120sec	-
1st coating Bake conditions	70deg.C -5min. / 90deg.C - 10min	70deg.C -5min. / 90deg.C - 10min	Hotplate (Temp. gradation)
2st coating Bake conditions	90deg.C -5min. / 100deg.C - 5min / 110deg.C - 10min	90deg.C -5min. / 100deg.C - 5min / 110deg.C - 10min	Hotplate (Temp. gradation)
Wait for solidifying	Leave 3 hours ~ 24hours to make the coating solid		-

As shown in Fig. 3.23, the double coating photoresist process was applied to two wafers (wafer 1: 50 μm depth, wafer2: 80μm depth). All structures were covered by photoresist properly, except for some of 50μm x 50μm single trench photodiode structures. The 200 μm X 200 μm, 150 μm X 150 μm and 100 μm X 100 μm structure were properly covered by approximately 22 μm thickness of PR. However, in case of the 50 μm X 50 μm structure, the PR coating appears like a drop of photoresist due to its relatively higher aspect ratio (aspect ratio of 50 μm wide : 80 μm depth) than in other structures. For both wafers, the FTPD structures were covered by AZ 4620 PR properly as Fig. 3.24

shows. An average intensity of 13.53 mW/cm^2 Hg-arc UV-light was used for 110 second exposure. After 60 seconds of exposure, a 3 minutes rest interval was applied to avoid photoresist bubbling caused by the long exposure and heating effects.

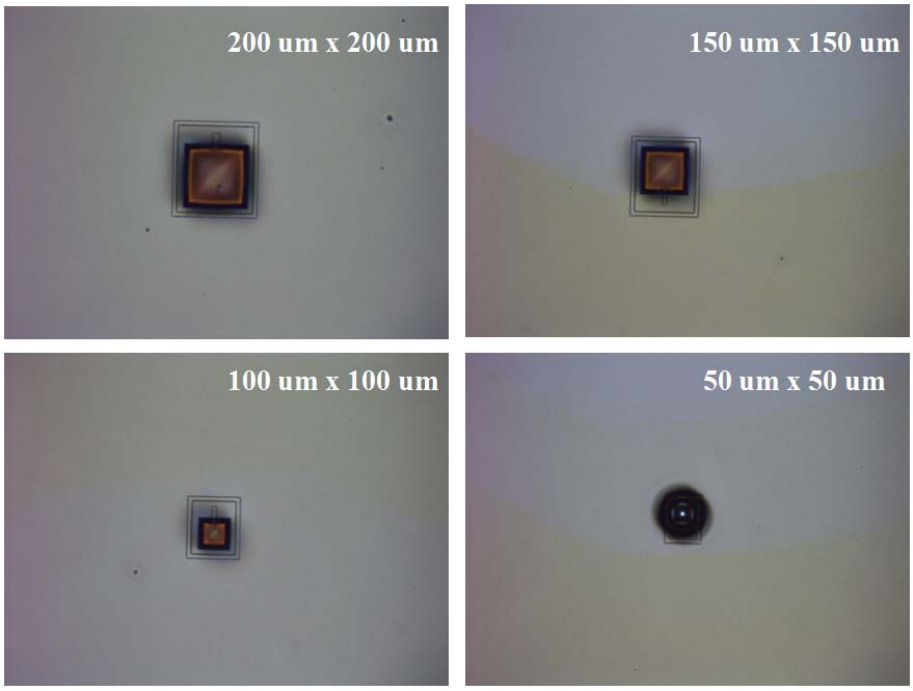

Figure 3.23. Microscope images of single trench photodiodes covered by photoresist.

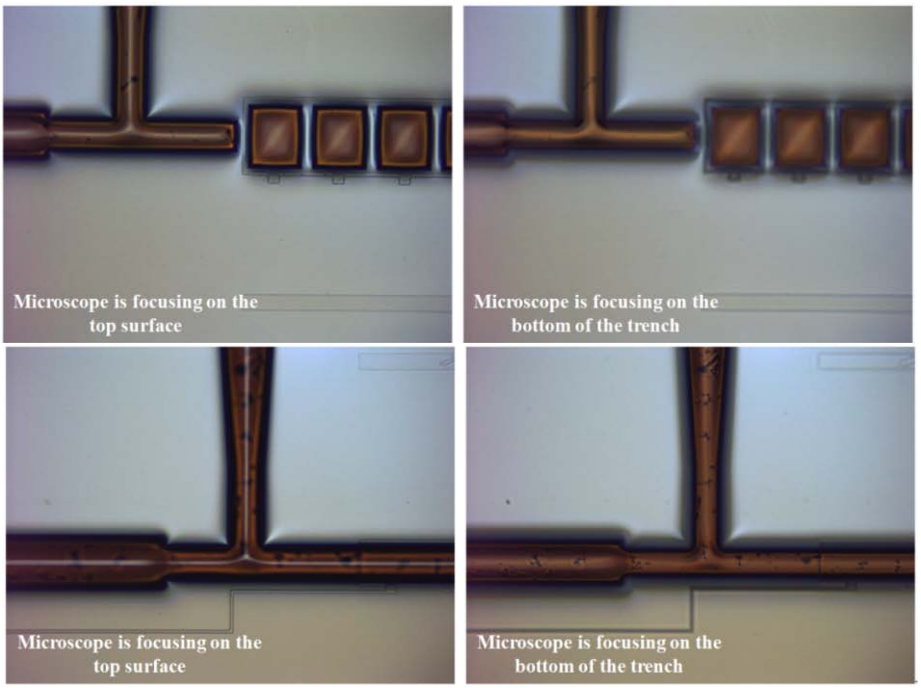

Figure 3.24. Microscope images of PR covered FTPDs.

A layer of 1 μm thick aluminum was then deposited using an electron beam evaporator. A lift-off process was performed to pattern 1 μm thickness aluminum metal. The lift-off technique is most typically employed in patterning metal thin films for making electrical interconnections [48]. It is especially suitable for gold and platinum patterning due to the fact that these metals are hard to etch [49]. Thus, most metals, multi-metal stacks and their alloys can be patterned with lift-off process. The wafers were soaked in acetone for 3 hours and then placed in an ultrasonic bath for 30 minutes. Once the aluminum layer began to peel off as shown in Fig. 3.25, gentle agitation of the acetone container helped complete the metal lift-off process. For the proposed device design, metallization using the lift-off technique appears to the best choice of other options such as metal etch-back since the proposed device has many deep trenches.

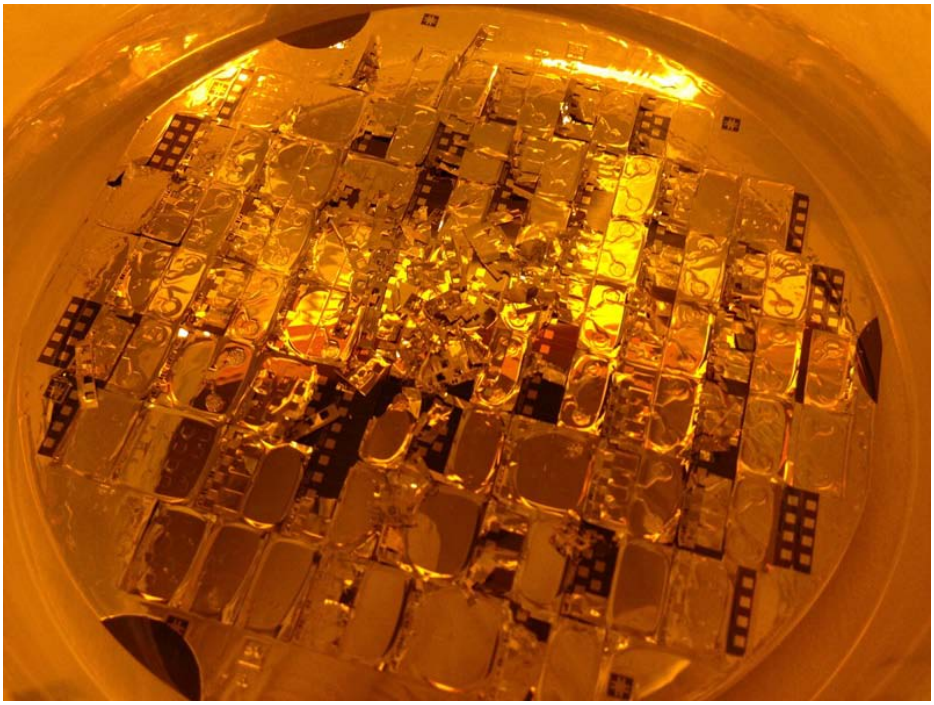

Figure 3.25. Aluminum metal lift-off process using acetone for 5 minutes.

Finally, the aluminum metal was annealed to reduce the contact resistance and re-crystallize the aluminum at the aluminum-silicon interface. N_2 gas was passed continuously through the furnace tube to minimize contamination by back-streaming of the air into the high-temperature tube. The wafers were annealed at 450 °C for 10 minutes. Fig. 3.26 shows the finished wafer.

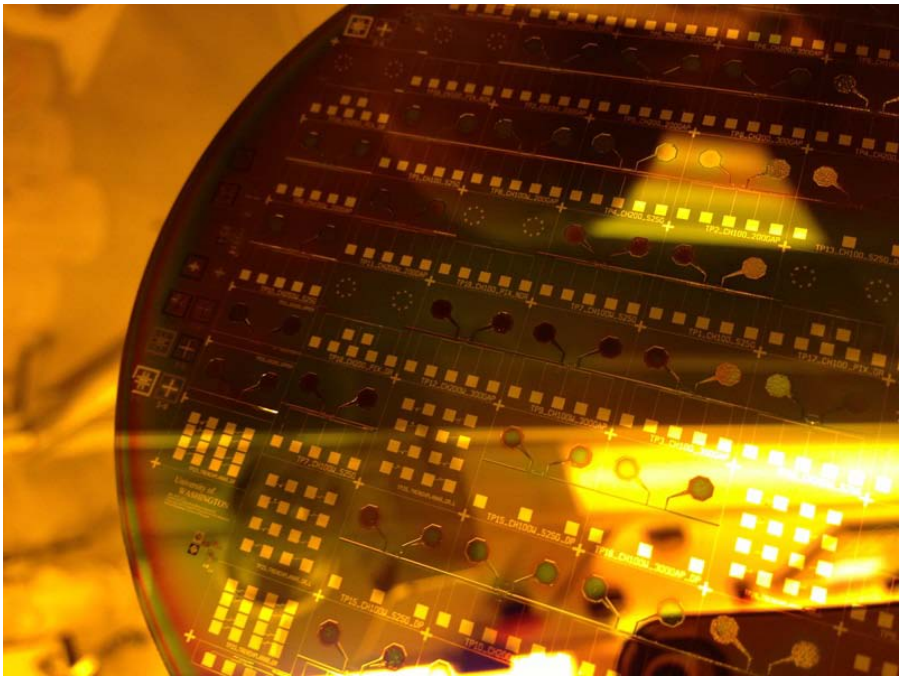

Figure 3.26. A completely fabricated wafer.

3.3.3 Problems and solutions

While the entire fabrication process was ultimately performed successfully, some problems occurred which required additional development effort. It was obvious that fabrication of this type of device structure which has deep trenches is not straightforward in comparison to a more general PIN photodiode structure.

1. Thickness variation of the photoresist coating

Due to the large trench features, photolithography became more difficult than that performed before the trenches were made by DIRE. Thickness variation of photoresist caused process failure in the PR development step. As can be seen in Fig. 3.27, while some areas were under-developed, other areas were over-developed.

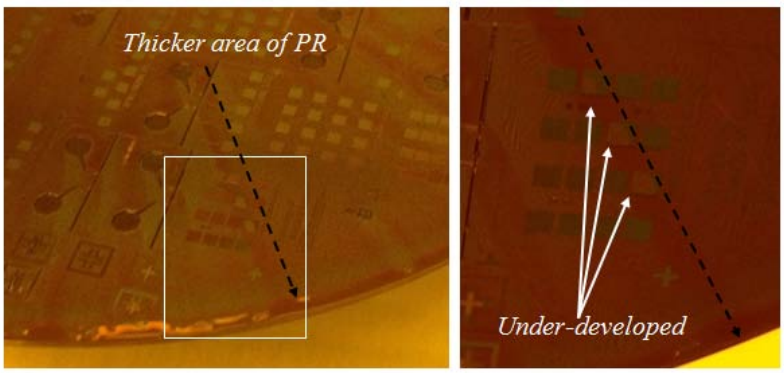

Figure 3.27. Under-developed area due to the relatively thicker photoresist. Arrows are representing the area of the thicker photoresist.

As shown in Fig. 3.28, the big and deep trench features blocked the fluid spreading of the PR during the spin coating step. As Fig. 3.29 illustrates, the relatively darker areas are the wafer are covered by thicker PR. The photoresist requires a relatively longer time to be developed properly than in thinner areas. Through trial-and-error, optimized process conditions, such as exposure time, development time, and PR baking methods were established. In this case, device design margins are strongly required in the mask design, such as wider electrode lines, larger size via holes, and a larger space between electrode lines or pads.

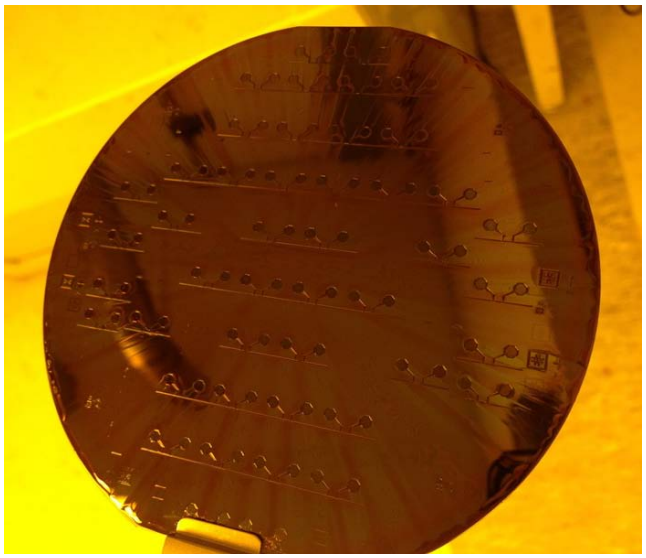

Figure 3.28. Results of double-photoresist coating. The coated photoresist layer is not uniform and has many stripes. The darker stripes represents thicker areas of the photoresist.

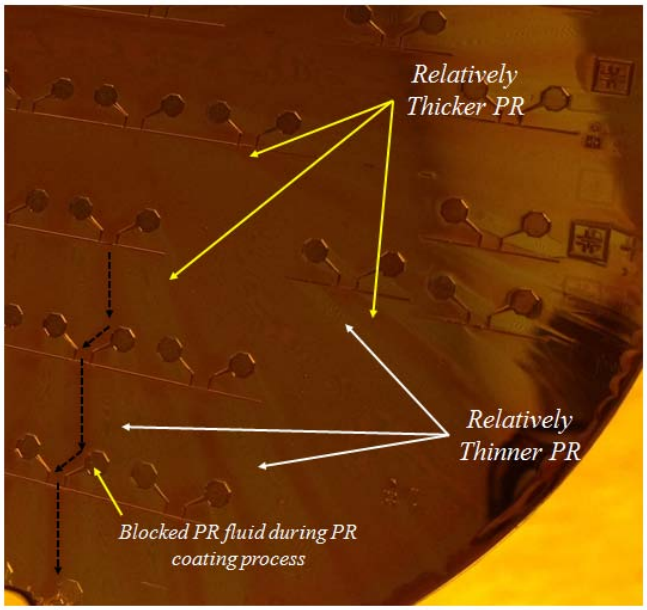

Figure 3.29. Due to the big and deep trench features, spreading of the photoresist was blocked during the spin coating step.

2. Wafer Breakage

After the DRIE process, many deep trenches are created. These trenches can increase the likelihood of wafer breaking issue. Especially in the second p+ boron diffusion process, more care is required to arrange the wafers to the quartz boat slots. Wafers are easily broken by even small impacts than wafers before DRIE process. After the diffusion process, the quartz boat must be handled very gently, particularly if the quartz boat sticks inside the furnace tube. The cleaning procedure for the quartz ware such as the furnace tube and boat helped significantly to solve this issue, since boat or wafer sticking issues after a high temperature furnace operation generally come from the contamination of quartz ware.

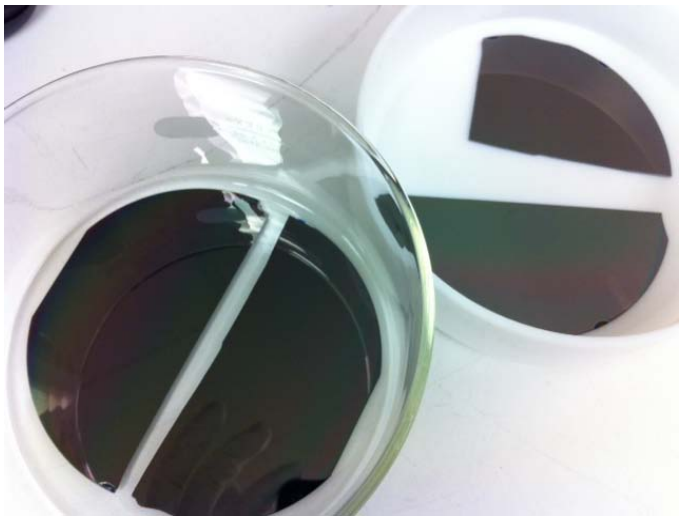

Figure 3.30. Broken wafers.

3. Boron-Silicon Skin deglazing

An excess B_2O_3 layer accumulating on the processing wafer creates a dark brown color skin (~65 nm), which can deteriorate device properties, increasing the high series resistance of the device, for instance. However, the problem is that it is very difficult to remove this layer with most acids. [50]. Thus, after the 10:1 HF deglazing step, an additional low temperature oxidation (LTO) process was performed to remove the excess B_2O_3 layer and the boron-silicon skin. The purpose of LTO step is to oxidize the un-etched boron-silicon layer and some thin silicon layer along with the defects. Oxidizing a thin silicon layer will immobilize most of the crystal defects in the oxide. Oxygen gas and the oxidation furnace were used to perform a dry oxidation of the boron-silicon layer and its silicon interface region. This step allows defects to not propagate into the silicon during the high temperature process which will be performed later. Table 3.10 and Fig. 3.31 through 3.33 show the steps of the LTO and deglazing processes to remove the B_2O_3 layer, boron-silicon layer, and some silicon region pinned by defects [51].

Table 3.10. Steps of the LTO Process [51].

Step	Details	Purpose
1	1st B_2O_3 and masking oxide Deglazing	HF etching after deposition / 10 : 1 DI Water to 49% HF for 2 minutes / To remove the layer from the exposed silicon surface and B-doped masking oxide
2	Low Temperature Oxidation (LTO)	To oxidize Boron-Silicon layer / 750C for 20 minutes in 100% oxygen ambient
3	2nd Deglazing boron-silicon layer	To remove un-etched B_2O_3 and SiO2 layer created by oxidizing the boron-silicon layer (~200A thick) / To remove defects pinned in the oxidized boron-silicon layer / To remove some of un-etched masking oxide due to B_2O_3 / 10 : 1 DI water to 49% HF for 2 minutes

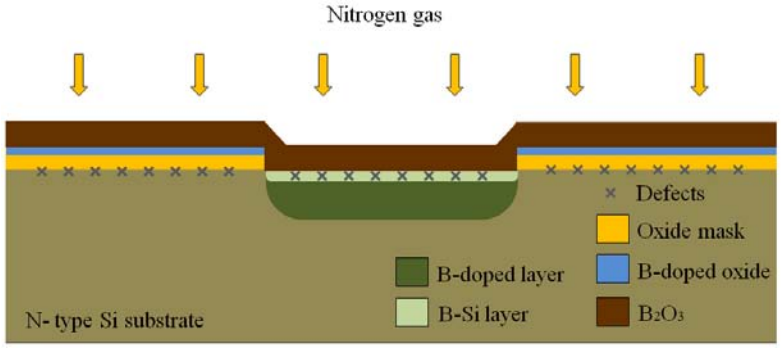

Figure. 3.31. Cross section view of the silicon wafer after p+ boron diffusion

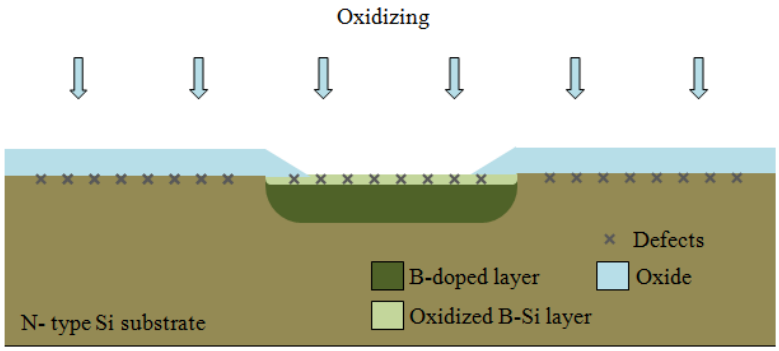

Figure. 3.32. Cross section view of the silicon wafer after 1st deglazing and LTO oxidation (step 1 and 2 in the table 3.10)

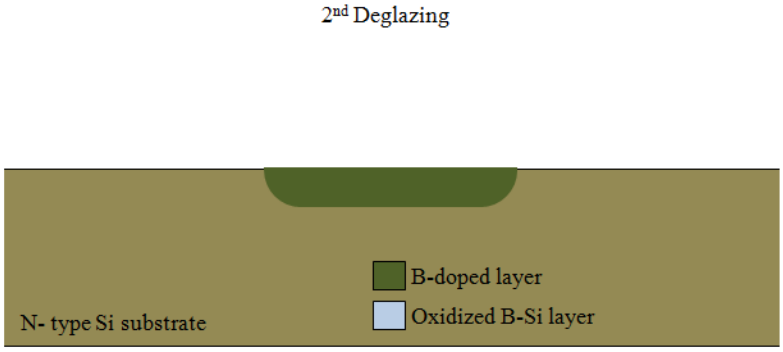

Figure. 3.33. Cross section view of the silicon wafer after 2nd deglazing (step 3 in the table 3.10)

Chapter 4
Optoelectronic Device Measurement

In this chapter, the test devices will be characterized in three ways through electrical, optical, and microfluidic measurements. The testing of this unique silicon PIN photodiode design has been developed to evaluate and improve its performance for micro diagnosis applications such as disease detection, cell counting, laser induced fluorescence detection, and miniaturized total analysis systems.

4.1. Electrical measurements

4.1.1 Electrical measurement set up

Current-voltage (I-V) measurements of the planar and trench type photodiodes were carried out using a HP-4145B, a semiconductor parameter analyzer. The experimental setup for electrical testing consists of a HP-4145B, a microscope, five spring Pogo™ pin probes, two micro-positioners, and NI LABVIEW data acquisition software as shown in Fig. 4.1 and 4.2.

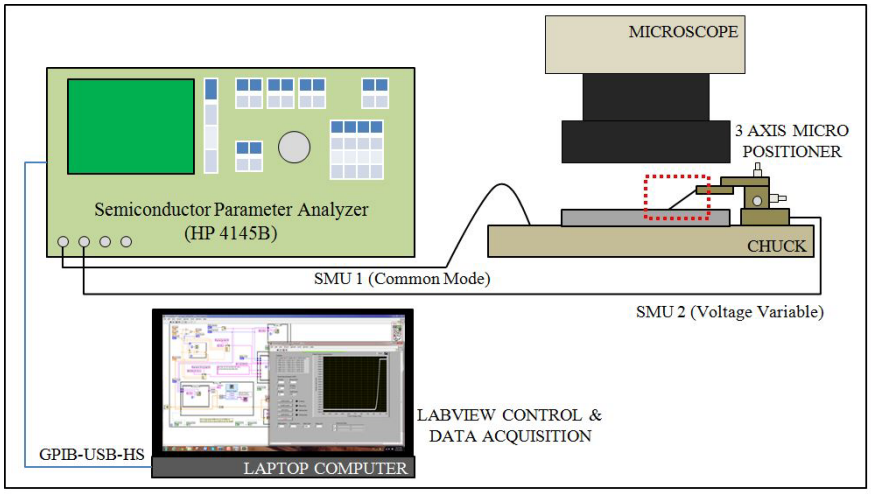

Figure 4.1. Diagram of electrical testing setup.

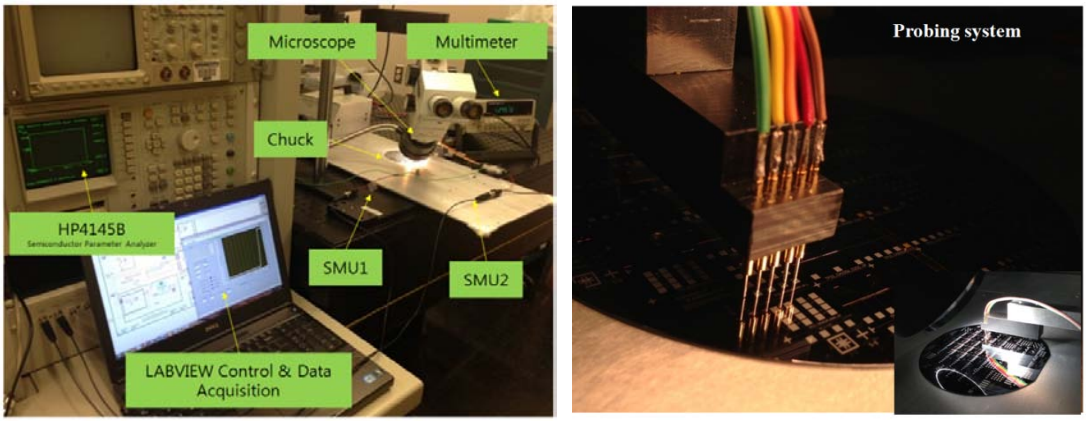

Figure 4.2. Entire electrical testing setup (left), and probing system (right).

In Fig. 4.1, two Source-Monitor-Unit (SMU) cables were used for the electrical measurement. SMU 1 was set up as an electrically common node and connected to the chuck to apply bias to the backside of the wafer. The backside electrode was fabricated by depositing 1μm thickness of aluminum and diffusing high concentration phosphorus n-type impurity onto the backside of the silicon wafer so that it has a good ohmic contact property at the interface of the silicon substrate and aluminum film. Simultaneously, SMU 2, which is a voltage variable, was connected to the micro-positioner through one of five spring-loaded Pogo™ pin probes with a 2 mm pitch such that it can be aligned and contacted to each 1 mm by 1 mm size metal pads with 2 mm pitch as well, as Fig. 4.1 shows. This connection allows each PIN photodiode to operate in the reverse biased mode.

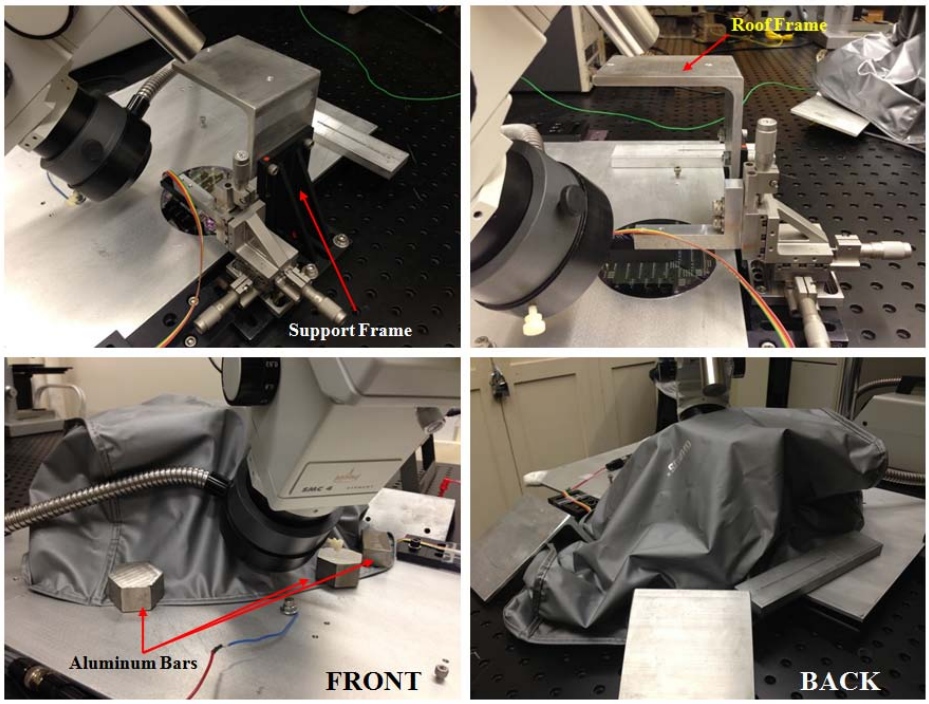

Figure 4.3. An installed dark cover.

In order to create a completely dark condition for the samples while under electrical testing, a dark cover was installed over the measurement stage as shown in Fig. 4.3. In addition, the room lights were turned off during testing to further reduce the entrance of stay light. A roof frame was used to support the dark cover, and five aluminum bars were used to press down the edges of dark cover in order to cut off the light from outside of the cover completely.

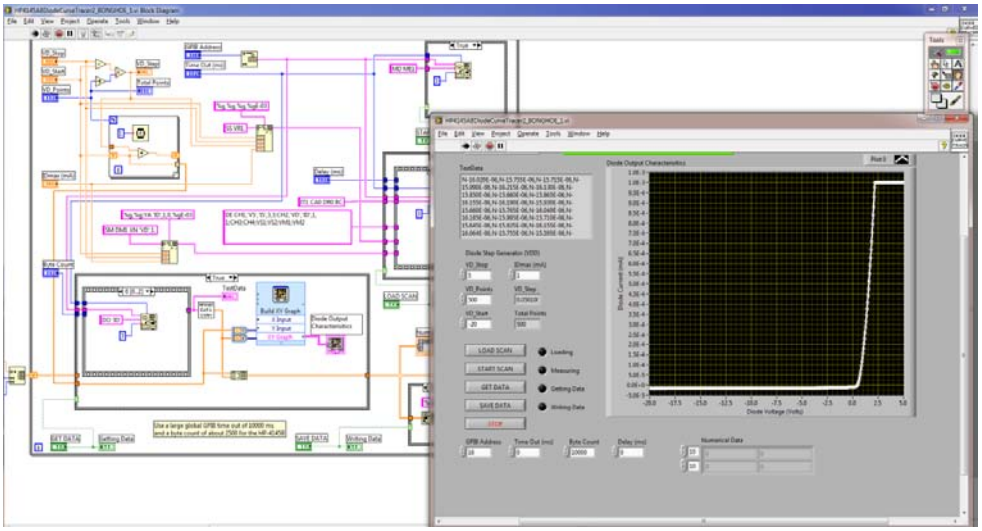

Figure 4.4. National Instrument (NI) LabVIEW software to control and collect the data from HP-4145B.

For more convenient data acquisition, NI LabVIEW software was used for collecting measured data from the HP-4145B using a GPIB (General-Purpose Interface Bus - IEEE 488) card to communicate with the HP-4145B. Collected data could be saved as a text format file and organized as a graph in the LABVIEW front panel like Fig. 4.4.

4.1.2 Dark current measurement of single PDs, planar FTPDs and trench FTPDs

In this section, current-voltage (I-V) curves describing dark current measurements of different PIN photodiodes; single PDs, planar FTPDs and trench FTPDs.

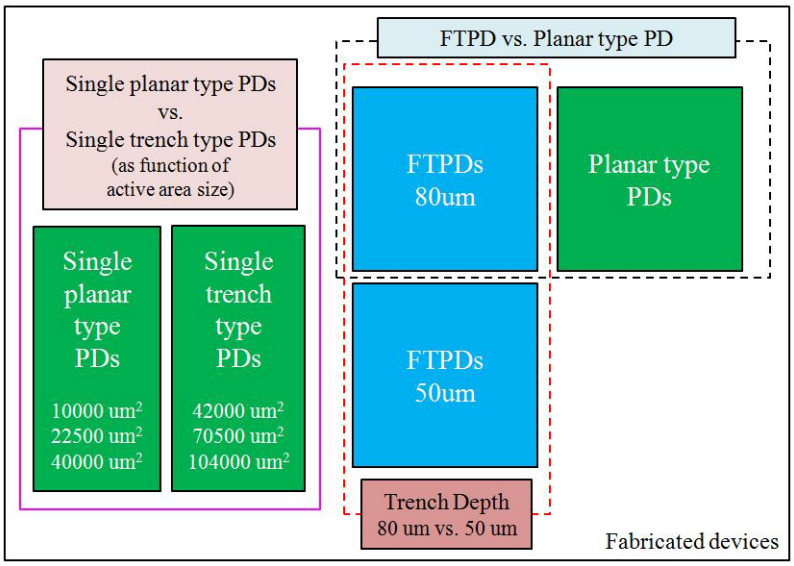

Figure 4.5. Fabricated devices and their comparison plan.

Fig. 4.5 shows the dark current measurements of planar and trench PDs with different sizes of the active area. Normally, the dark current is the current generated under a reverse bias condition without

any illumination to the photodiodes. The dark current was measured with the HP-4145B based on the setup shown in Fig. 4.1, and the voltage sweep was performed from −2 V to 1 V. Since the dark current strongly depends on the volume of the depletion region and the thermal-generation current of the photodiode, trench PDs which have larger depletion region volumes show larger values of dark current [52].

1. Single PDs

As was discussed in Chapter 3 and shown in Fig. 4.5, six different single PIN photodiode structures with different geometries and active area sizes were constructed for testing. The two types of PIN photodiodes geometries included the commonly used planar type PD, and the trench type PD, which is the basic reference structure for the flow through PIN photodiode (FTPD).

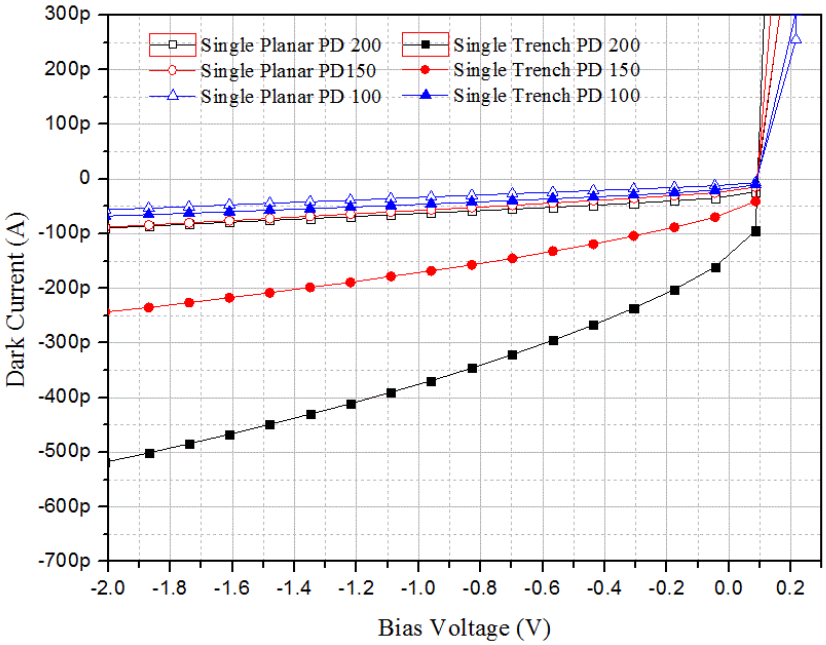

Figure 4.6. Dark current of trench type photodiodes with active areas of 100 μm × 100 μm (Black), 150 μm × 150 μm (Red), and 200 μm × 200 μm (Blue). The depth of trenches are the same in each case, 80 μm.

Fig. 4.6 and 4.7 show the dark current measurement of three planar and three trench type PDs with various active areas. The trench photodiodes have larger active area depending on the depth of the trench because their four trench sidewall areas are additional photodiodes as well, even though it may seem the trench and planar PD have the same active area size taking account of only the top view. In practice, the larger size photodiode generates the more dark current, since more carriers are randomly generated within the larger depletion region of the PDs and then they are swept out by the high electric field.

The average dark current values of the planar PDs were 37.3 pA, 51.2 pA, and 61.0 pA at −2 V for

active areas of 100 μm × 100 μm , 150 μm × 150 μm, 200 μm × 200 μm size, respectively. Moreover, 35.2 pA, 96.5 pA, and 228.0 pA average dark current of trench PDs were measured at −2 V for 100 μm × 100 μm , 150 μm × 150 μm, 200 μm × 200 μm size, respectively. Even though the average dark current measured for trench PDs with 100 μm × 100 μm active area was smaller than that for the planar PDs with the same active area, a larger variation of the measured values of the trench type PDs was observed than the planar type PDs. The much larger variation is believed to be due to the etching process using deep reactive ion etching (DRIE) which leaves a rough sidewall finish.

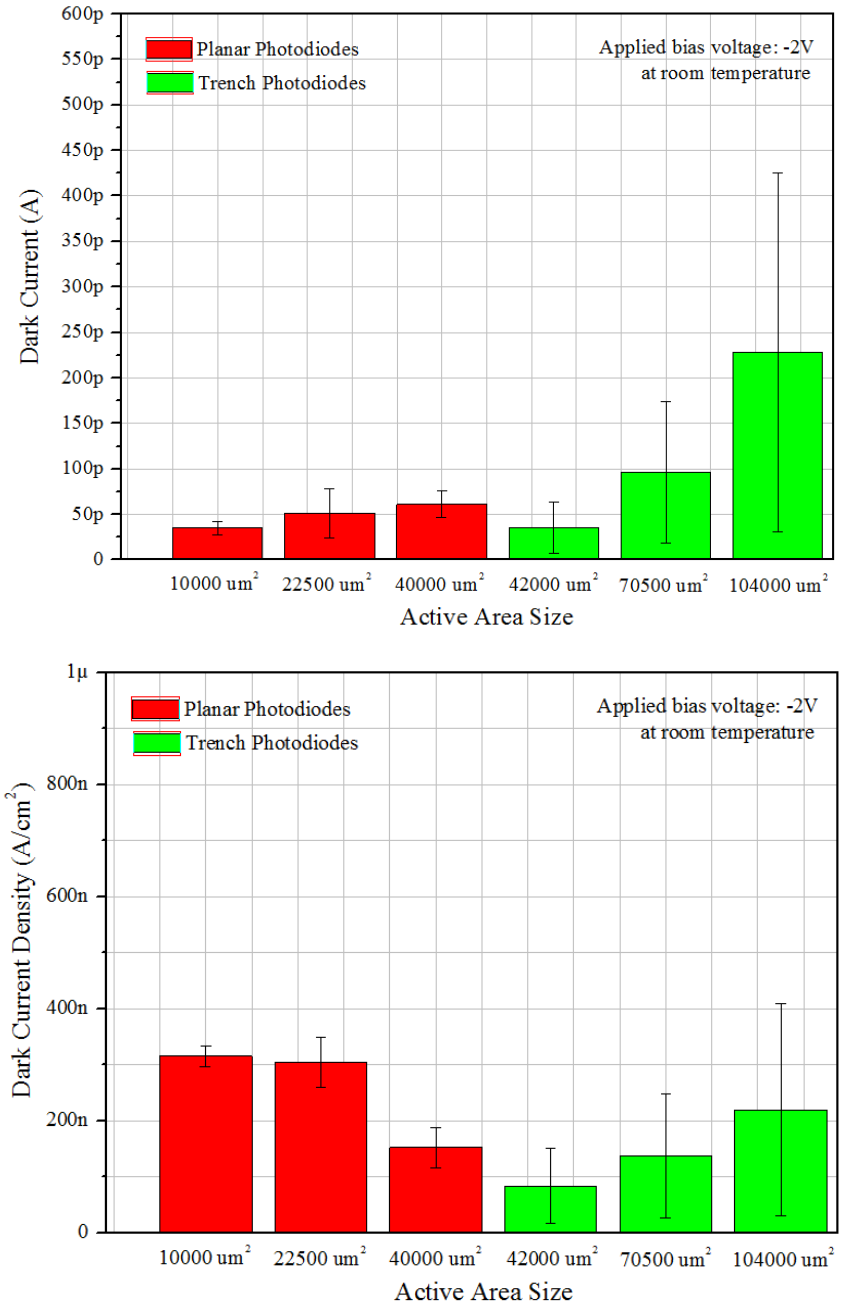

Figure 4.7. Dark current and dark current density of planar and trench type single photodiode, 5 test points were measured.

Table 4.1. Mean and standard deviation of the dark current and dark current density as a function of photodiode type and active area.

Type	Active area size	Mean of dark current(A) @−2 V	Standard deviation	Notation
Planar	**10000 μm^2**	3.73×10^{-11}	6.12×10^{-12}	Single Planar PD 200
Planar	**22500 μm^2**	5.12×10^{-11}	2.72×10^{-11}	Single Planar PD 150
Planar	**40000 μm^2**	6.10×10^{-11}	1.44×10^{-11}	Single Planar PD 100
Trench	**42000 μm^2**	3.52×10^{-11}	2.81×10^{-11}	Single Trench PD 200
Trench	**70500 μm^2**	9.65×10^{-11}	7.77×10^{-11}	Single Trench PD 150
Trench	**104000 μm^2**	2.28×10^{-10}	1.97×10^{-10}	Single Trench PD 100

Type	Active area size	Dark current density (A/cm^2) @-2 V	Standard deviation	Notation
Planar	**10000 μm^2**	3.50×10^{-7}	6.12×10^{-12}	Single Planar PD 200
Planar	**22500 μm^2**	2.27×10^{-7}	2.72×10^{-11}	Single Planar PD 150
Planar	**40000 μm^2**	1.52×10^{-7}	1.44×10^{-11}	Single Planar PD 100
Trench	**42000 μm^2**	8.38×10^{-8}	2.81×10^{-11}	Single Trench PD 200
Trench	**70500 μm^2**	1.37×10^{-7}	7.77×10^{-11}	Single Trench PD 150
Trench	**104000 μm^2**	2.19×10^{-7}	1.97×10^{-10}	Single Trench PD 100

At this point, a possible reason why the trench PDs has a larger variation of dark current than the planar PDs can be proposed. According to Nakamura [28], the leakage current depends on the trench's sidewall topology as well. These authors demonstrate that the leakage current of the trench structure which has scalloping sidewalls created by the Bosch process using gasses of SF_6 and C_4F_8 has around 10 times larger dark current than one with smooth sidewalls fabricated by direct etching using SF_6 and O_2 without scalloping. The authors suggest that SiO_N dielectric barriers show tensile cracks at the groove points of scalloping sidewalls, which are caused by stress concentrations in the SiO_N barrier, and which could generate more leakage current [28]. Moreover, at the interface between the silicon substrate and the 1 μm thickness PECVD SiO_2 layer on the scalloping sidewall of trenches, interface defects such as dangling bonds and impurities are able to generate interface energy states in the silicon energy gap. These defect states are able to act as a generation-recombination centers. As a result, this causes increased Si-SiO_2 interface leakage current and a larger dark current density for the FTPDs.

2. Planar type PDs & FTPDs

Fig. 4.7 illustrates the dark current density of planar type PDs and FTPDs. The FTPD generated more dark current below −1.2 V bias voltage. However, near the zero bias operation region or from 0 to −1.2 V, the trench FTPD generated lower dark current than the planar FTPD. The measured trench FTPD has a relatively large p-doped active area (0.0908 cm^2) because the trench FTPD was tested

before the photodiodes are separated by laser machining to make four independent trench pixels. Dark current density of FTPDs increased steeply to 1.76×10^5 A/cm^2 at −2 V reverse bias voltage.

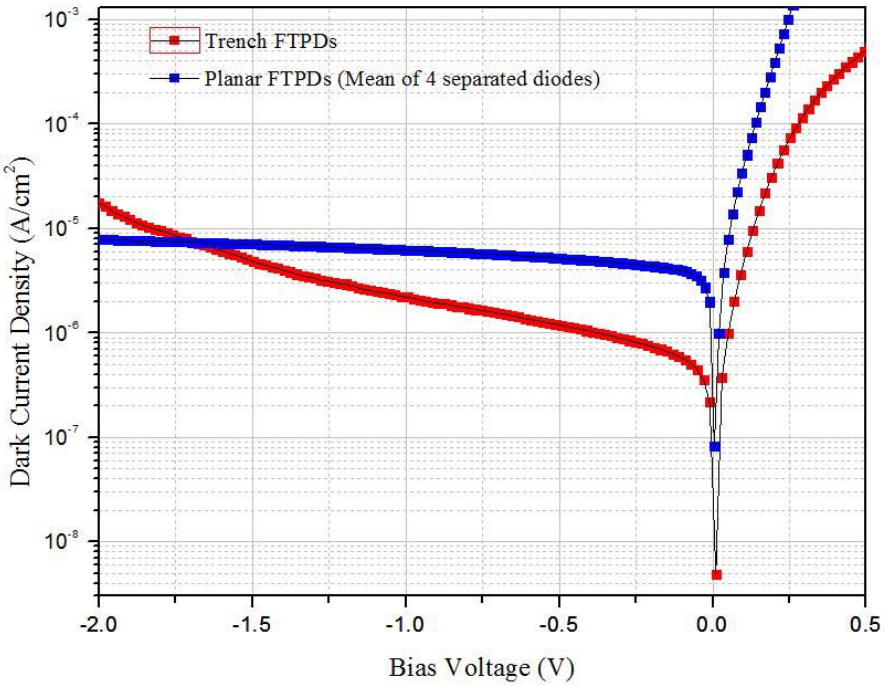

Figure 4.8. Dark current density of planar and FTPDs. The active area of the trench FTPD is 0.0908 cm^2 before laser cutting to separate PDs.

4.1.3 Breakdown voltage (V_{BR}) of single trench PDs

Single trench PDs were used to evaluate the breakdown voltage. A PIN photodiode biased in the reverse direction exhibits a small saturation current. At higher voltages a critical electric field between the p and n sides of the photodiode is generated, and reverse breakdown occurs and the reverse current through the photodiode increases dramatically. The breakdown mechanism involves impact ionization by collision of energetic carriers with the lattice under high electric field conditions, and finally it leads to carrier avalanche multiplication. Additionally, for the fabricated devices under investigation, breakdown phenomena by the tunneling effect is negligible because the junction region involves lightly doped n-type substrates, 7.37×10^{12} atoms/cm^3.

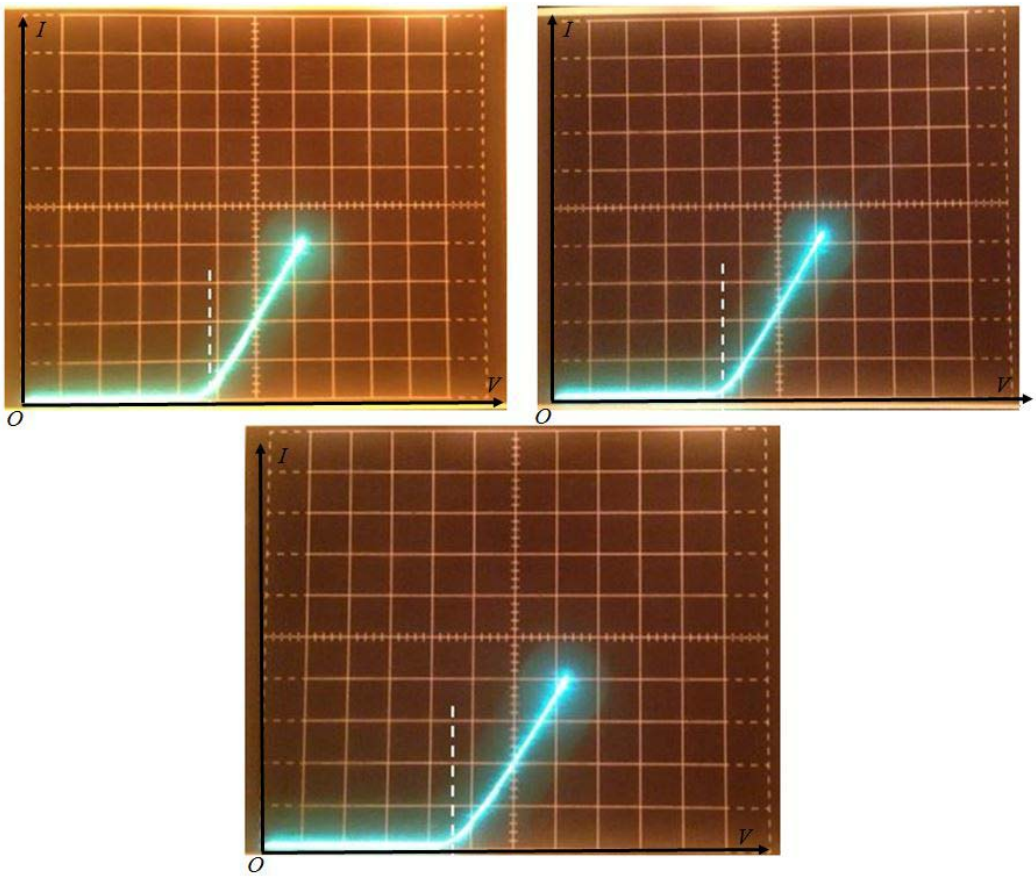

Figure 4.9. Tektronix 576 Curve Tracer screen capture; trench PD 200 µm by 200 µm (top left), trench PD 150 µm by 150 µm (top right), and trench PD 100 µm by 100 µm (bottom), Vertical: 1 mA per div, Horizontal: 50 V per div.

A Tektronix 576 Curve Tracer was used to measure the breakdown voltage, defined as when 10 µA of reverse current flows through the photodiode. The Tektronix 576 was used to sweep the reverse bias voltage through the range of 0 V through 350 V. The current increased abruptly at 240 V, 230 V, and 225 V for single trench PDs with 200 µm × 200 µm, 150 µm × 150 µm, and 100 µm × 100 µm size active area sizes, as shown in Fig. 4.9. Table 4.2 exhibits these values of breakdown voltage for single PDs of different active area sizes.

Table 4.2. Breakdown voltage of single trench PDs

Model	**V_{br} (@I_{dark}= ~10 µA)**
Single Trench PDs 200 µm × 200 µm	~240 V
Single Trench PDs 150 µm × 150 µm	~230 V
Single Trench PDs 100 µm × 100 µm	~225 V

The breakdown voltages in the range of 220 V through 240V were lower than the calculated value. According to hand calculations, the breakdown voltage should occur at a much higher voltage of

17000 V. The calculation assumes an abrupt pn-junction diode to simplify the calculation, but in practice, the doping profile cannot be made like this. Also, fabrication process defects, dust over the sensor and humidity might be reasons that occur an immature breakdown. However, sensors will not experience voltages this high in normal use, so the measured breakdown voltage is perfectly adequate.

4.2. Optical measurements

4.2.1 Optical measurement set up

In this investigation, three different colors, red, green, and blue-violet laser pointers (maximum power of 5 mW), were used as light sources, and they were coupled with an optical fiber as shown in Fig. 4.11(b). For example, a diode-pumped solid-state (DPSS) laser module consists of a powerful 808 nm IR diode laser that pumps a Nd:YVO4 laser crystal, generating 1064 nm light. This fundamental is frequency doubled to 532 nm by passing through a non-linear Potassium Titanyle Phosphate ($KTiOPO_4$, KTP) crystal, as illustrated in Fig. 4.10.

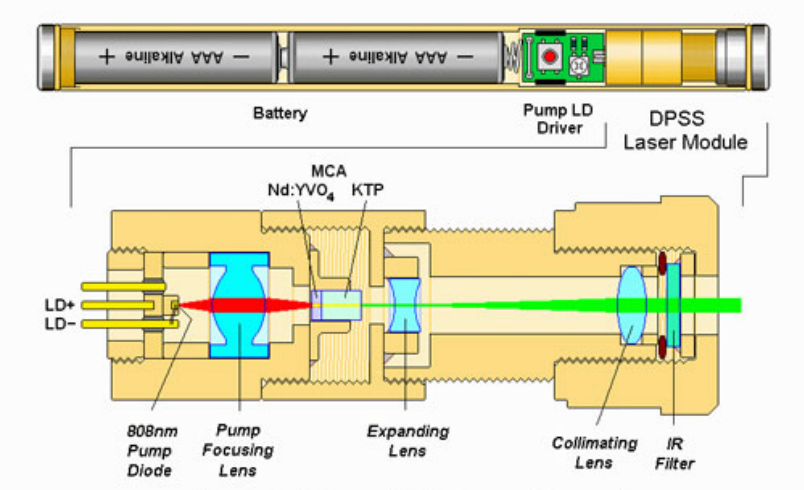

Figure 4.10. Internal construction of a green laser pointer, Courtesy of Chris Chen [53].

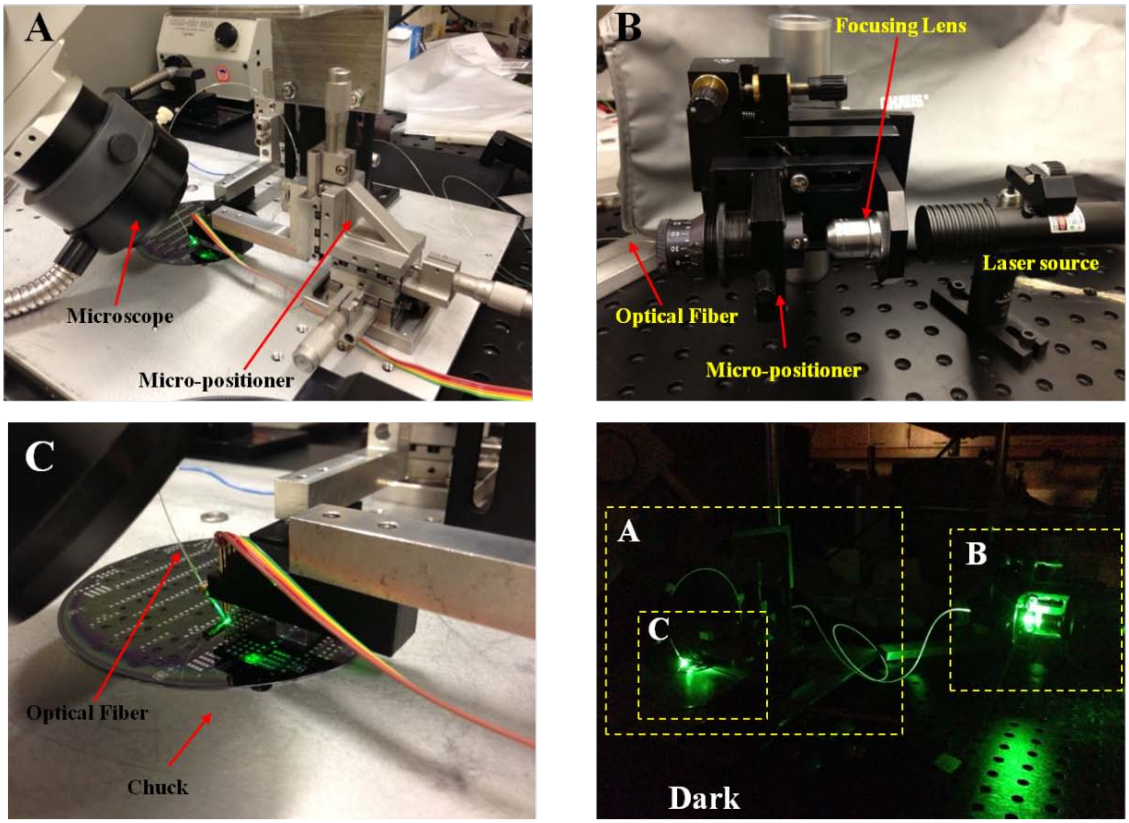

Figure 4.11. Optical experiment setup.

The optical experimental setup is shown in Fig. 4.11. One more micro-positioner was added to the experimental setup for the electrical measurements in order to hold an optical fiber to transmit the excitation light to the photodiodes. An optical fiber was coupled with a special micro-positioner using a microscope objective lens in order for the incident light to be focused and aligned from the laser source to the other end of a properly cleaved optical fiber. This special micro-positioner was used to precisely control the direction of the optical fiber by adjusting x, y, z, and theta axis knobs. A F-MSD multi-mode optical fiber from Newport Fiber Optics, which has 50 ± 3 μm core diameter, 125 ± 2 μm cladding diameter, and 250 ± 15 μm UV cured acrylate coating diameter around cladding was used. The acrylate coating (or jacket) was carefully removed by stripping with razor blade, and the fiber was cleaved with a Newport Fiber Optic Field Cleaver. Fig. 4.12 shows the end faces of optical fibers cleaved improperly by hand (a) and an optical fiber cleaved properly by using the cleaving tool (b). Generally, cleaving an optical fiber involves scribing and breaking the endface of the fiber to obtain a perpendicular and mirror-smooth face. Poor cleaving as shown in Fig. 4.12 (a) will cause lips and burrs, and as a result, it gives poor quality fiber coupling. Additionally, dust and particles on the optical fiber surface can be cleaned with isopropyl alcohol and a pressurized nitrogen gun.

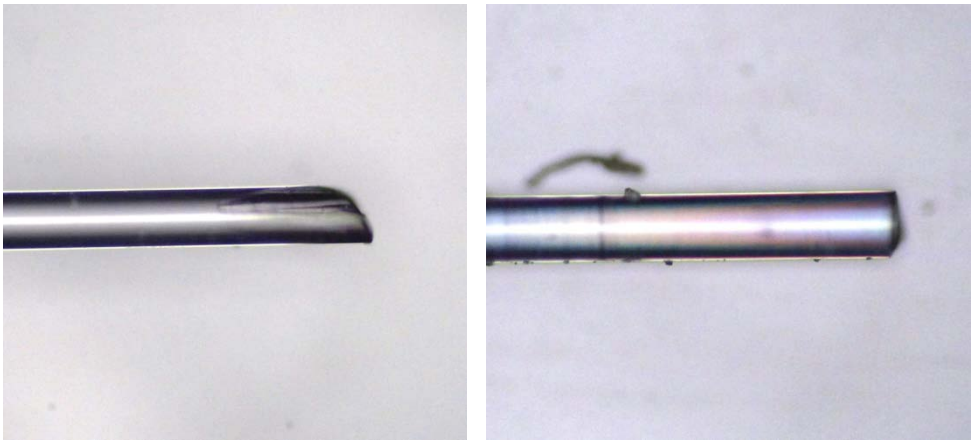

(a) (b)

Figure 4.12. Microscope images of the end of an optical fiber (a) cleaved improperly, (b) properly.

The second micro-positioner holds an optical fiber in order for its end to face directly into the planar surface or trench bottom of the planar type PDs or FTPDs, respectively.

As demonstrated above, three different laser sources which have various wavelengths: red (650 nm), green (532 nm), and blue-violet (405 nm), were prepared and used for measuring the optical properties as a function of wavelength. Optical measurements were made under dark conditions in the laboratory. The optical power of each laser beam was measured by Newport 1830-C digital power meter. For accurate and reliable measurements, it is important to ensure the stability of the optical power from the laser source, since laser sources are operated by a battery which varies over time.

Fig. 4.13 indicates a procedure block diagram for the optical measurements. The current measurement was carried out using a HP-4145B. A total of three current measurements were taken during each cycle of testing. In each cycle of current measurement, the optical power measurement was carried out twice. As indicated by the blue lozenges in Fig. 4.13, The optical power at the beginning of each measurement set P_1 is compared to the power at the end of the measurements, P_2. The purpose of these additional steps are to ensure a continuous output power from the laser sources. If the measured power at the beginning and at the end is the same ($P_1 = P_2$), then it can be assumed that a constant power was applied to the trench and planar PDs without variation from battery life sag or heating effects of the cheap laser module.

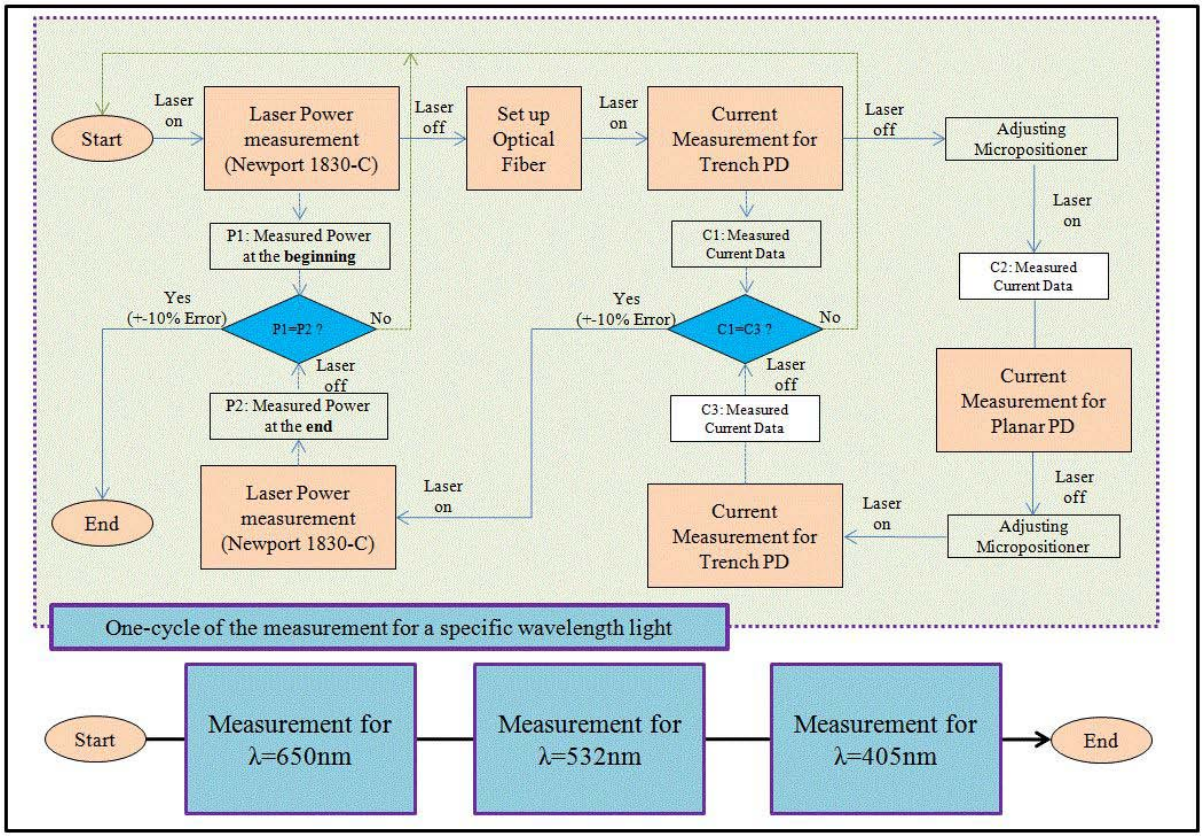

Figure 4.13. A procedure block diagram of the optical measurement.

4.2.2 Reverse bias photocurrent

The generation of current due to the minority carriers transport across the junction was introduced in Chapter 2. If the junction is illuminated by photons which have a higher energy than the band gap energy, the generation of electron-hole pairs will produce a photocurrent.

Fig. 4.14 shows the reverse bias photocurrent values of a single trench and planar type PD with 200 μm by 200 μm size as a function of wavelength. Single trench type PDs with 80 μm depth were used for measurements. The current was measured under the voltage sweep mode of the HP-4145B from −20 V to 2 V at room temperature. As light sources, red (650 nm), green (532 nm), and blue-violet (405 nm) laser pointers were used and their optical output power was 1.34 mW, 1.26 mW, and 0.37 mW, respectively. Each laser source emitted the light constantly during the voltage sweep of HP-4145B.

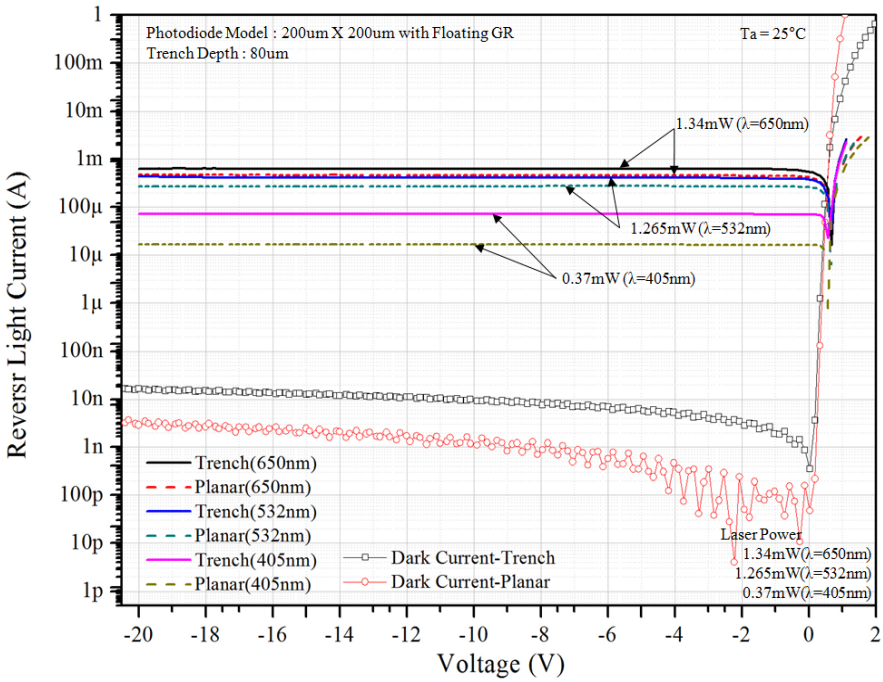

Figure 4.14. Reverse bias photocurrent of trench and planar type single photodiodes as a function of wavelength.

The graph shows that the trench type PDs created higher photocurrent (solid lines) than the planar type PDs (dash lines). In addition, the light generated current density, J_{light}, for each type of PDs as a function of wavelength of laser source is shown in Fig. 4.15. Trench type PDs generate more current at a reverse bias of 2.5 V as expected since this device has a larger effective active volume from the p-doped sidewalls of trench than does the planar type PD. Also, the light generated current density of the trench type PDs was 4.33 times larger at 650 nm (1.340 mW), 1.72 times larger at the 532 nm (1.265 mW), and 1.37 times larger at 405 nm (0.370 mW).

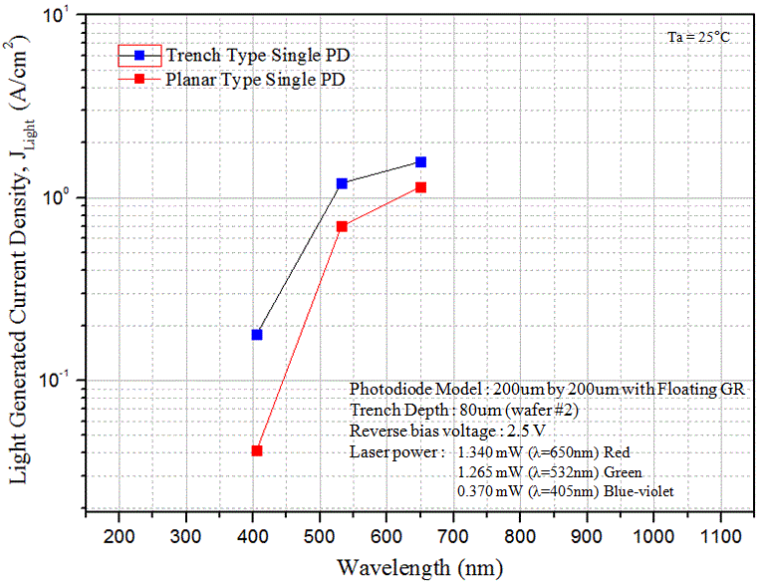

Figure 4.15. Light generated current density of trench and planar type single photodiodes as a function of wavelength.

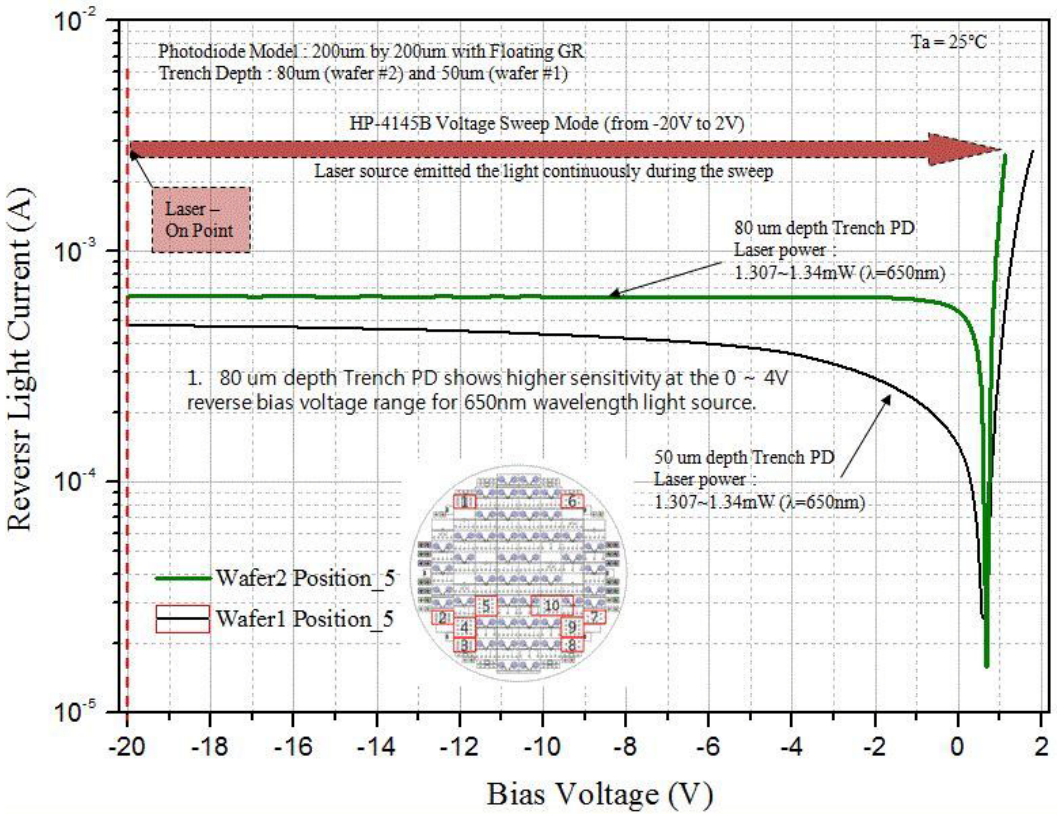

Figure 4.16. Photocurrent of 80 μm and 50 μm deep trench PDs as a function of reverse bias voltage.

Fig. 4.16 shows a comparison between the photocurrent of a 80 μm (water #2) and a 50 μm (wafer #1) deep trench type PD. Under the same conditions, the voltage sweep was performed using the red laser pointer with an optical power of around 1.30 mW-1.34 mW. The 80 μm deep trench PDs produced a larger photocurrent than the 50 μm depth ones because the 80 μm deep trench PDs have larger depletion area volume, arising from the taller p-doped sidewalls.

4.2.3 Responsivity

In this section, responsivity measurements of trench and planar type PDs will be discussed. Responsivity is the ratio of the collected current in amperes (*A*) to the radiant energy in watts (*W*) from the incident light. Measurement of the laser power and the photocurrent was carried out based on the procedure shown in Fig. 4.13. A Tektronix PS283 power supply was employed to apply a constant voltage of 3 V to the laser pointers instead of the two 1.5 V batteries connected in series. The measured laser power from the end of the optical fiber is shown in Table 4.3. Even though the power supply was used as a power source for laser pointers, there were still small output power variations for the three different wavelength laser pointers, since their laser modules can be affected by the internal heating or the life time of optical parts inside the module as illustrated in Fig. 4.10.

Table 4.3. Optical power, reverse bias photocurrent, and calculated responsivity of single trench and planar type photodiodes for three different wavelengths of laser sources.

Wavelength (nm)	Red(650nm)				Green(532nm)				Blue-Violet(405nm)			
Laser Power (mW)	1.340		1.310		1.450		1.270		0.370		0.370	
Type	**Single Trench PD**		**Single Planar PD**		**Single Trench PD**		**Single Planar PD**		**Single Trench PD**		**Single Planar PD**	
	Mean	Stan.D	Mean	Stan.D	Mean	Stan.D	Mean	Stan.D	Mean	Stan.D	Mean	Stan.D
Reverse Light Current @-2.5V	6.30E-04	2.61E-06	4.58E-04	4.74E-06	4.81E-04	3.02E-05	2.79E-04	2.32E-05	7.14E-05	4.13E-06	1.65E-05	8.45E-07
Photosensitivity (A/W)	0.470	0.002	0.342	0.004	0.332	0.021	0.214	0.018	0.193	0.011	0.045	0.002

Comparison results of the photocurrent and responsivity between the single trench PDs and the planar PDs are indicated in Table 4.3, where the responsivity was calculated based on Eq. 4.3.

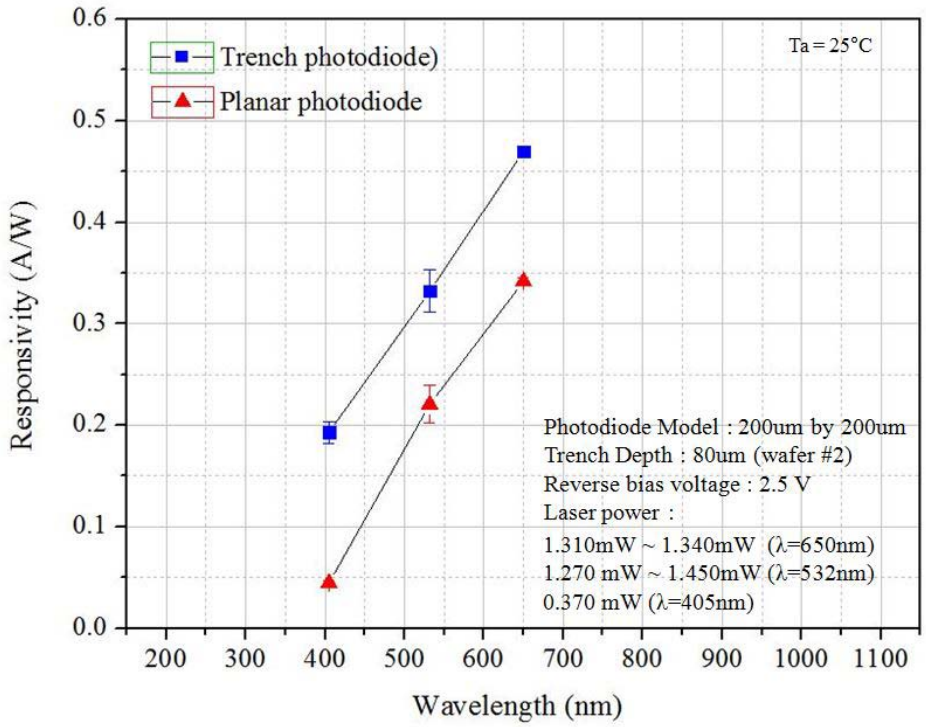

Figure 4.17. Responsivity of the trench and planar type PDs as a function of wavelength.

Fig. 4.17 shows the measured responsivity of the trench type PDs as a function of wavelength. The graph illustrates a responsivity difference of 0.18 A/W to 0.23 A/W between the trench PDs and planar PDs. The trench PDs shows a much higher sensitivity than the planar PDs. Conventional microfluidic optical sensor prototypes which have used commercial planar PDs have presented some drawbacks. One of the critical weaknesses is that they introduces an enormous optical loss due to the fact that the angular FOV is only a few degrees.

Table 4.4. Optical power, reverse bias photocurrent, and calculated responsivity of single 80μm deep 50 μm deep trench photodiodes for three different wavelengths of laser sources.

Wavelength (nm)	Red(650nm)				Green(532nm)				Blue-Violet(405nm)			
Laser Power (mW)	1.340		1.340		1.450		1.275		0.370		0.374	
Type	**80μm depth Trench PD**		**50μm depth Trench PD**		**80μm depth Trench PD**		**50μm depth Trench PD**		**80μm depth Trench PD**		**50μm depth Trench PD**	
	Mean	Stan.D	Mean	Stan.D	Mean	Stan.D	Mean	Stan.D	Mean	Stan.D	Mean	Stan.D
Reverse Light Current @-2.5V	6.36E-04	1.70E-06	4.20E-04	1.73E-05	4.81E-04	2.75E-05	3.41E-04	2.32E-05	7.15E-05	4.08E-06	6.80E-05	3.21E-07
Photosensitivity (A/W)	0.475	0.001	0.322	0.013	0.332	0.019	0.273	0.019	0.193	0.011	0.182	0.001

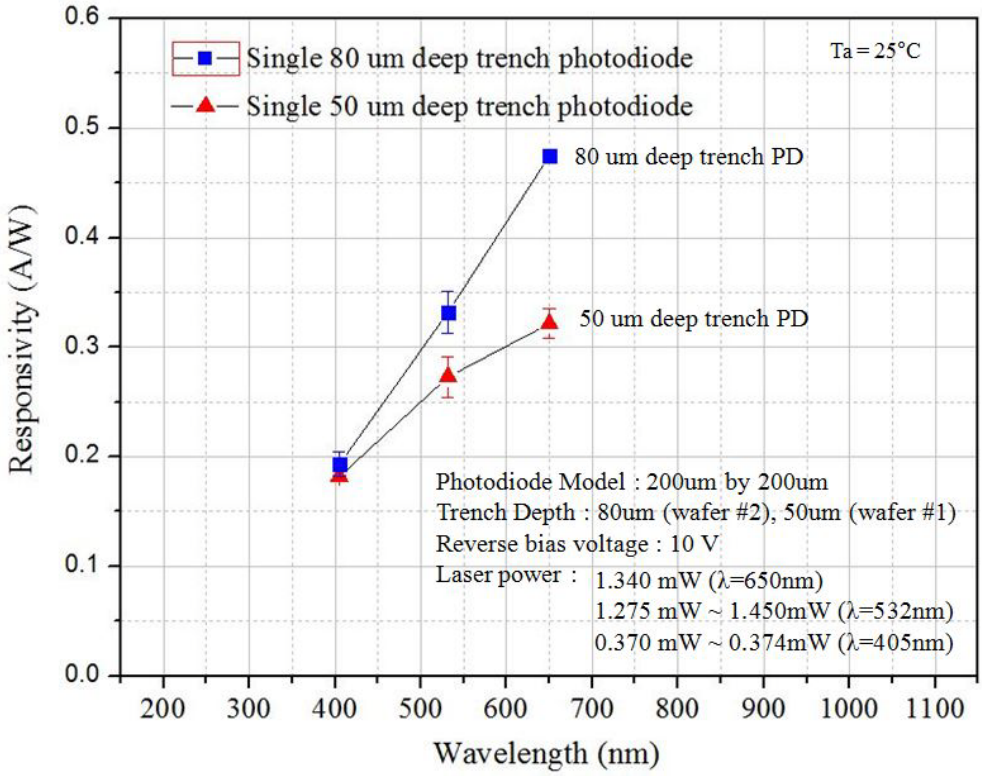

Figure 4.18. Responsivity of 80 μm and 50 μm deep trench PDs as a function of wavelength.

Additionally, the responsivity depends on the trench depth. Trench PDs which have a deeper trench depth can generates more light current than the planar PD as discussed in the previous section, since the deeper trench PDs have larger depletion region volume. Responsivity values of 80 μm and 50 μm deep trench PDs are shown in Fig. 4.18. At 450 nm, (blue-violet), the responsivity of the trench and the planar PD are nearly the same because photons with 405 nm wavelength can penetrate only around 0.3 μm into the silicon as Fig. 4.19 indicates. Consequently, 80 μm deep trench PDs indicated a higher responsivity than 50 μm deep trench PDs.

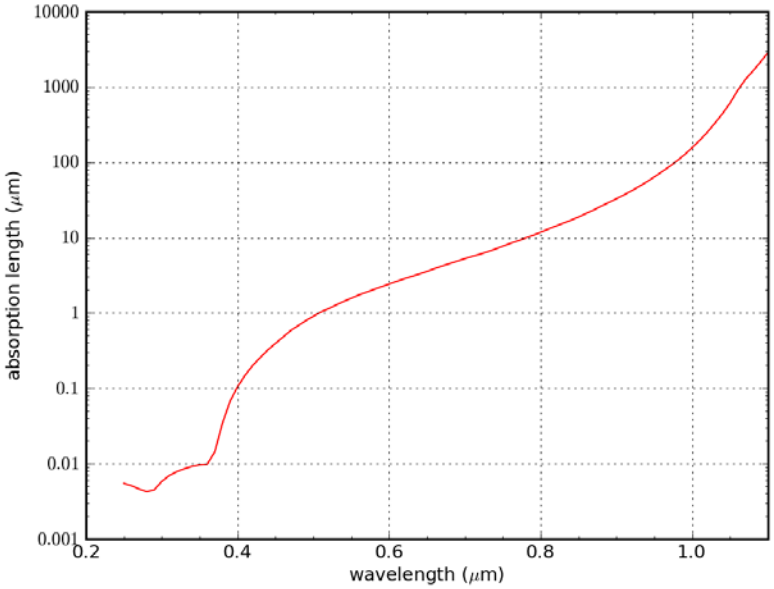

Figure 4.19. Logarithmic plot of the absorption length in silicon as a function of wavelength [54].

4.2.4 Quantum efficiency

Quantum efficiency (QE) is one of the most significant parameters used to evaluate the performance and quality of a photodetector. It is often called the spectral response to reflect its wavelength dependence. The quantum efficiency is the ratio of the number of carriers (electrons or holes) that can be converted to current to the number of incident photons. It is normally expressed and calculated in percent (%) based on the reference sensitivity (*A/W*) at a certain wavelength (nm),

$$QE = \frac{S}{\lambda} \times \frac{hc}{q} \approx \frac{S(A/W) \times 1240(W \cdot nm/A)}{\lambda(nm)} \times 100[\%] \qquad (4.4)$$

where S is the responsivity in A/W at a certain wavelength as shown in the previous section and λ is the given wavelength of the laser source, h is the Planck constant, 6.626×10^{-34}J-s, c is the speed of light, ~300000 km/s, and q is the electron charge which is 1.602×10^{-19} C.

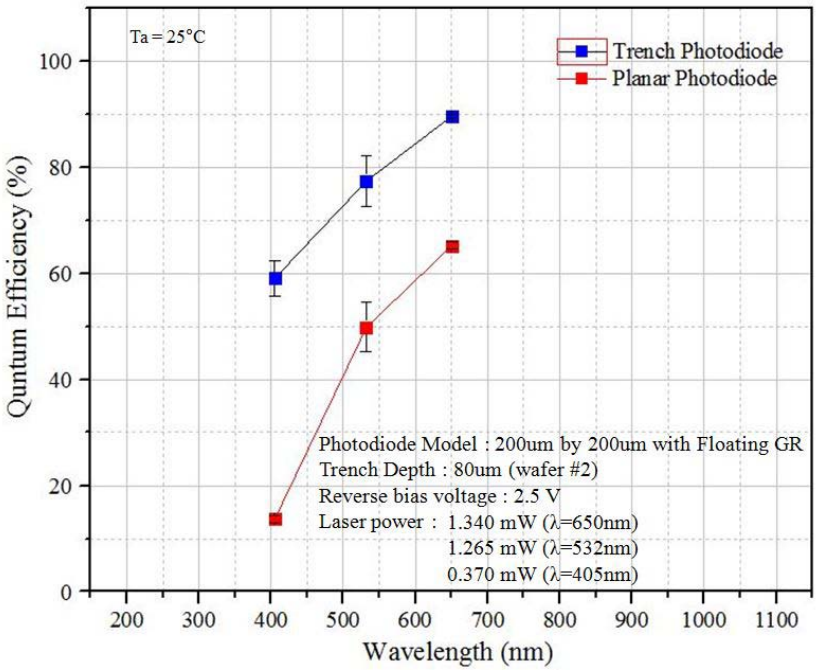

Figure 4.20. Quantum efficiency of the trench and planar PDs as a function of wavelength.

Through Fig. 4.20, it is possible to compare the quantum efficiency of the trench PD and planar PD. Quantum efficiency values were calculated based on Eq. 4.4 for each wavelength. Quantum efficiency of the trench PD was 4.55 times to 1.47 times higher than that of the planar PD for a 405 nm blue-violet laser source and a 650 nm red laser source, respectively.

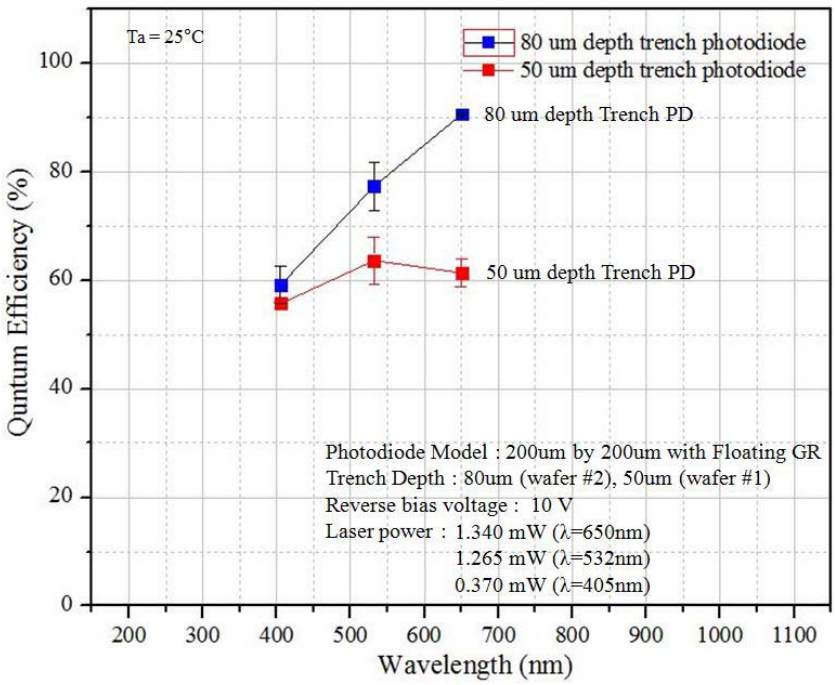

Figure 4.21. Quantum efficiency comparison vs. Wavelength.

According to the results above, trench PDs can be a good selection for optoelectronic device applications near the UV range. In this case, the trench PDs will be able to increase the quantum efficiency dramatically over the planar type PD. The peak of the quantum efficiency was at 532 nm wavelength among three various laser sources. As discussed in the responsivity measurement, quantum efficiency of the trench PD is around 25% higher for green and red light wavelengths.

4.2.5 Responsivity comparison to a commercial photodiode

A S10783 silicon PIN photodiode from Hamamatsu was used for a comparative study of the responsivity. All the performance data of S10783 photodiode were based on its data sheet provided from Hamamatsu Photonics. The S10783 silicon PIN photodiode has 0.5 mm square effective sensitive area, 10 pA dark current at −2.5 V, typically 0.46 A/W sensitivity and 87.8 % quantum efficiency for a 650 nm wavelength light source as shown in Table 4.5 [55].

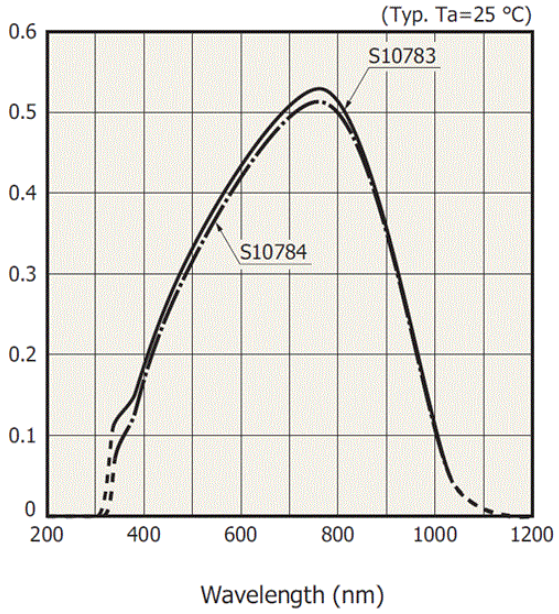

Figure 4.22. Responsivity vs. Wavelength graph of S10783 photodiode [55].

Table 4.5. Parameter comparison between fabricated PDs and a commercial silicon PIN PD from Hamamatsu Photonics.

Parameters	Single Trench PD (80 µm depth trench)	Single Planar PD	*Hamamatsu PIN PD (S10783)*	Units
Effective Photosensitive Area	0.104	0.040	*0.500*	mm^2
Dark current @ -2.5 V	0.55	0.06	*0.01*	nA
Dark current Density @ -2.5 V	5.28×10^{-7}	1.5×10^{-7}	2×10^{-9}	A/cm2
Responsivity @ 650 nm	0.64	0.43	*0.46 (typ.)*	A/W
Quantum Efficiency @ 650 nm	89.6	65.1	*87.8*	%
Laser Power (mW)	1.340	1.310	-	mW

The trench PD gives the highest values of both responsivity and quantum efficiency at 650 nm wavelength compare to the commercial silicon PIN photodiode, although it demonstrates 5.28 × 10^{-7} A/cm^2 dark current density at −2.5 V.

4.3. Light current density measurements of microfluidic sensors

4.3.1 Experiment preparation of the microfluidic formatted sensors

Sensitivity measurements in a microfluidic format were performed to evaluate the electrical and optical properties of both FTPD and planar type PD by using phosphorescent microspheres flowing through the trench channel. The measurement in this microfluidic format includes two preparation steps; sealing the device channel and preparing the phosphorescent microspheres.

1. Device sealing

One of the key requirements for a microfluidic sensor is sealing. Commonly, molded PDMS is used to create flow channels for biosensors by which a glass piece and a patterned PDMS layer can be bonded together through oxygen plasma ashing to properly treat the surfaces. In our case; however, a flexible plastic cover slip (cellulose acetate, square 22 mm × 22 mm) is used as an alternative method. Fig. 4.23 illustrates the dimensions of the plastic cover slip which has an inlet and an outlet hole. 1 mm diameter holes into the plastic cover slip were mechanically drilled.

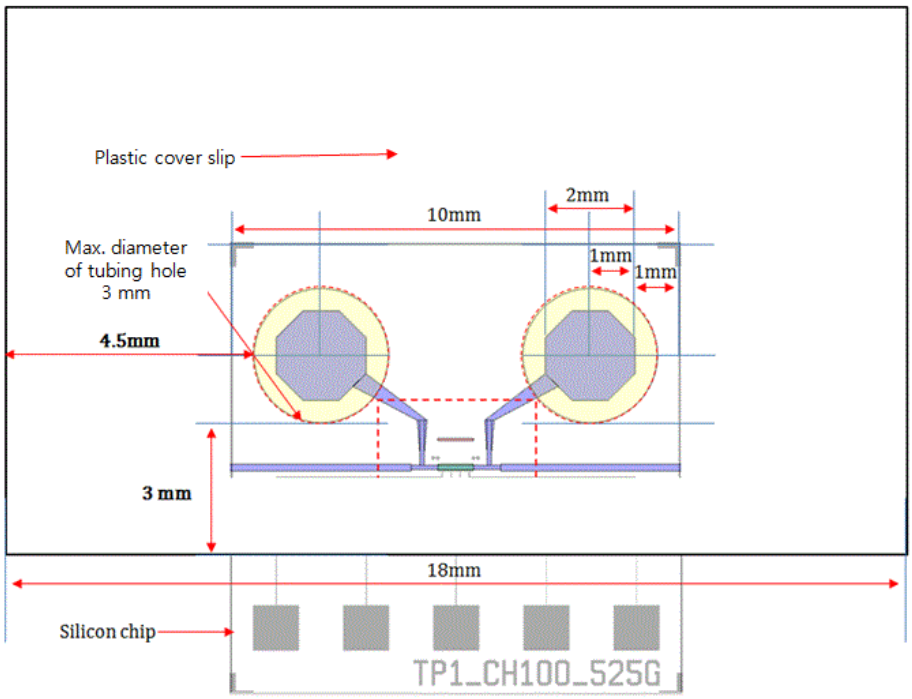

Figure 4.23. Dimensions of plastic cover slip with inlet and outlet hole.

Cyanoacrylate adhesive (FUTURE GLUE™ 15100 from Super Glue corp., CA) was used to bond the

sensor to the plastic cover slip. If a plastic cover slip is coated with too much cyanoacrylate adhesive, excess adhesive will flow into the trench channel during the bonding procedure. Since the sensor has a very shallow and narrow trench, excess adhesive can possibly block proper fluid flow.

Several methods to coat a thin and uniform adhesive layer onto the plastic cover slip were examined. The stamp-and-Stick (SAS) thermal bonding technique can be used to assemble components [56]. The SAS method uses a transfer wafer where the adhesive layer was first coated, and then the cover component is brought into contact with the adhesive like a stamp. Finally the cover component with a thin adhesive coating can be bonded with the device wafer. More detailed procedures can be found in the reference paper by Schmidt [57]. Similarly, as the SAS method employs spin coating to form an adhesive layer onto the transfer wafer, a spin coater was used to coat a thin and uniform adhesive layer onto a plastic cover slip.

A special vacuum spinning chuck for the plastic cover slip was created and installed in the spin coater, and the vacuum level was maintained a minimum level because the plastic cover slip is very thin and flexible. Excessive vacuum pressure causes an un-desired adhesive pattern on the plastic cover because of the vacuum grooves of the chuck which bend the cover slip slightly.

An adhesive coated plastic cover slip was first properly bonded to a trench type PD die. After the assembled components were fully bonded and dried, a microscope was used to check whether any excess cyanoacrylate adhesive had seeped into the trench channel, as shown in Fig. 4.24. In this figure, (a) indicates the area where the plastic cover slip and the top surface of the trench PDs were properly bonded. (b) shows the clean bottom of the trench which was not affected by any cyanoacrylate adhesive. Finally, (c) shows the inside of the trench where the excess cyanoacrylate adhesive had seeped into.

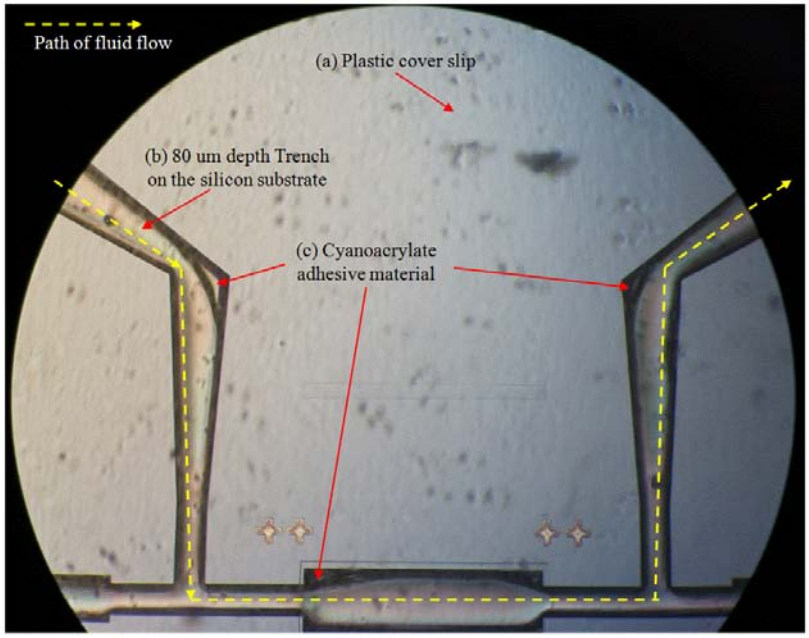

Figure 4.24. Microscope image of the properly FTPD sealed using a plastic cover and cyanoacrylate adhesive.

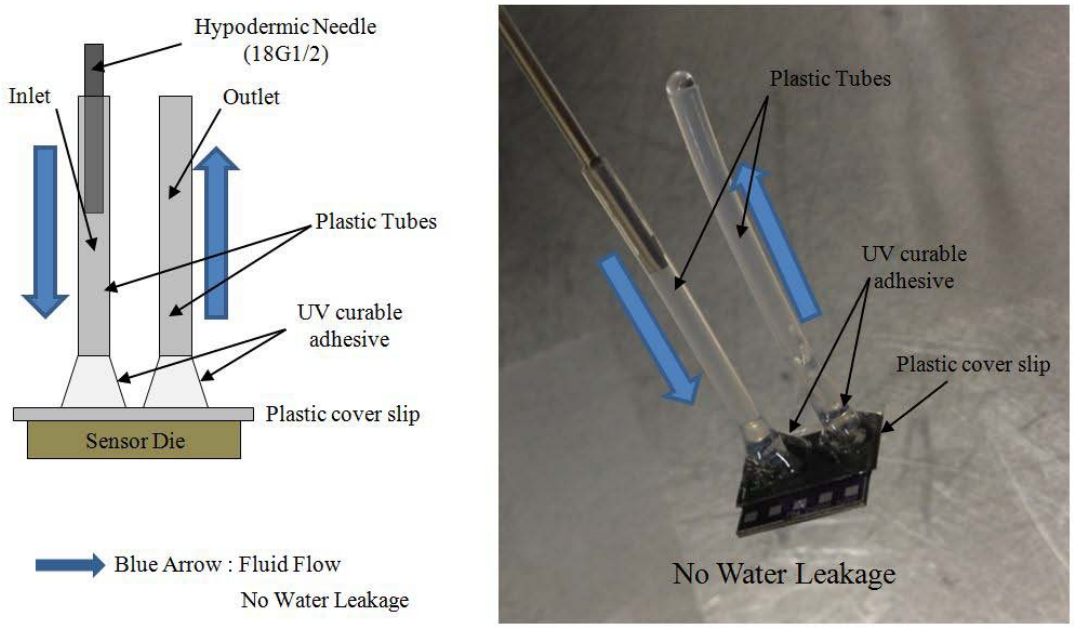

Figure 4.25. Sealing test of the trench FTPD.

After 24 hours curing time, two transparent plastic tubes were coupled to the inlet and outlet ports. Norland UV curable optical adhesive type NOA#68 was used. NOA#68 is a flexible adhesive designed to give improved adhesion to many plastics such as acrylic and polycarbonate. The refractive index of the cured polymer typically has a value of 1.54 [58]. When the adhesive is perfectly cured and dried by UV light, water leakage testing was performed to check if the fluid can flow through the channel without fluid leakage at any point where sealing has been done imperfectly. Fig. 4.25 shows an assembled trench PD operating properly.

2. Phosphorescent microspheres preparation

Polystyrene (PS), poly methyl methacrylate (PMMA) and silica materials are the most commonly used microspheres in biosensors. These materials possess different physical and optical properties, which may present advantages or limitations for different applications.

The polymer microspheres used in this work are generally hydrophobic and they have high protein binding abilities [59-61]. For use of with biosensors, microspheres can be synthesized with functional monomers, called co-polymerizing to give the microspheres reactive surface groups. They require a surfactant to ensure ease of handling and to facilitate the suspension of hydrophobic microspheres in water. The type and concentration of the surfactant should be optimized for the best performance. The commonly used concentration of surfactants is around 0.1 % for un-coated polymer beads and 0.01 % for storage buffering of coated polymer, magnetic, and silica beads [62]. In this work, 27 to 30 μm diameter phosphorescent microspheres from Cospheric LLC. were used

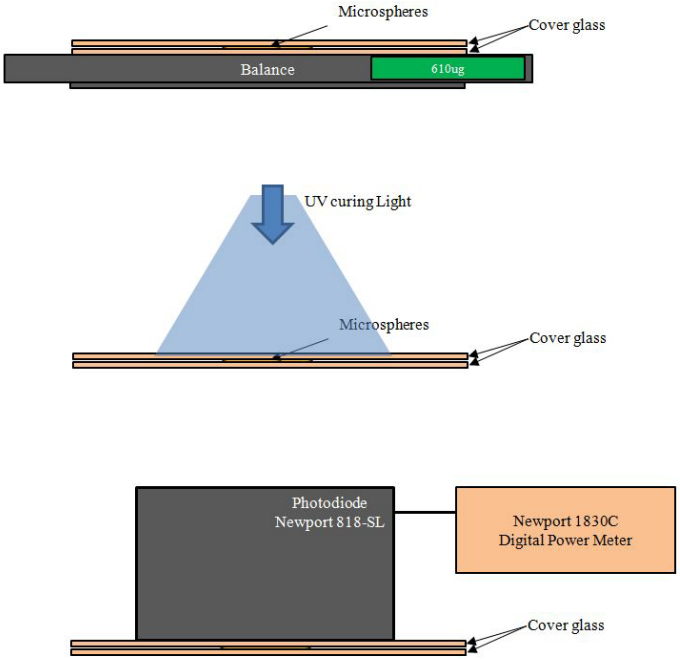

Figure 4.26. Steps of the emission power measurement of phosphorescence microspheres.

Optical power measurement of the phosphorescence was performed on the microspheres as a function of the mass to determine the phosphorescence emission power. 380 µg and 610 µg of phosphorescent microspheres were placed onto 2 inch × 1 inch cover glass using a Mettler AE163 microbalance whose minimum resolution is 10 µg. According to the information on the microsphres Cospheric LLC provides on their website, 380 µg and 610 µg includes 28148 and 45185 microspheres, respectively, and the mass of a microsphere is 13.5 ng [63]. The Newport 1830C digital power meter and 818-SL photodiode detector were employed to measure the optical power that the microspheres emit. A Tecklite UV curing light lamp of 498 mW or a white LED of 4.825 mW were used to excite phosphorescence of the microspheres.

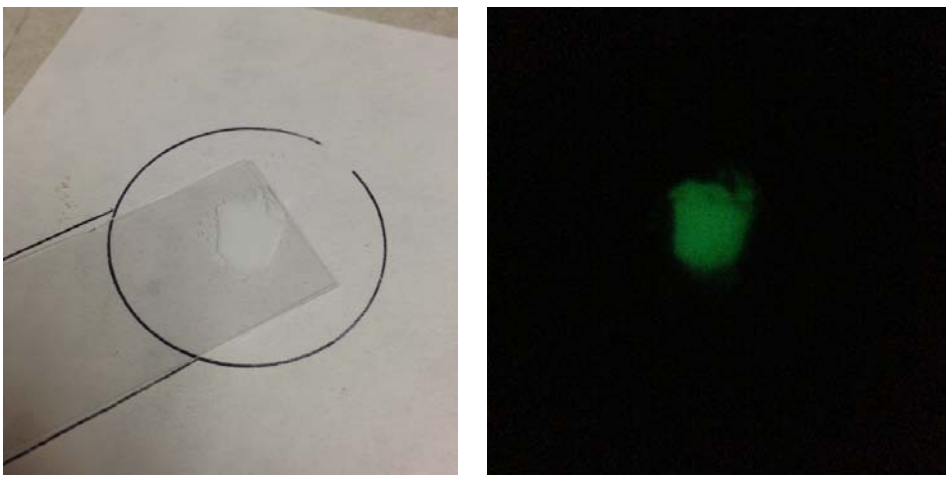

Figure 4.27. 680 micro-gram of microspheres; It is excited by ceiling light (Left), 680 micro-gram microspheres right after UV curing light excitation for 60 sec. (Right).

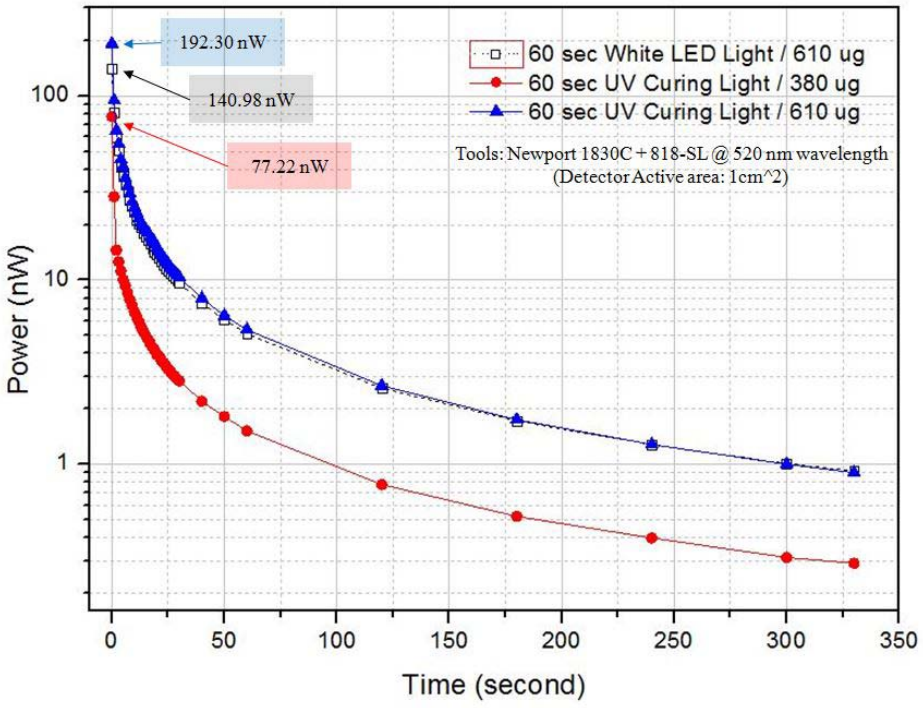

Figure 4.28. Light power decay curves of Cospheric phosphorescent microspheres of 380 μg and 610 μg.

Fig. 4.28 shows the emission decay measurement result of 380 μg and 610 μg of phosphorescent microspheres. The light emission power decreased exponentially as a function of time from 0 to 330 seconds. The maximum light emission power values were 192.30 nW, 140.98 nW, and 77.22 nW for the 610 μg microspheres excited by UV curing light, 610 μg microspheres excited by a White LED light, and 380 μg microspheres excited by UV Curing light, respectively. The light power increases as the mass of microspheres increases. The wavelength parameter input of Newport 1830C was set to 520 nm according to the typical excitation (left) and phosphorescence spectra (right) graph shown in Fig. 4.29 [63].

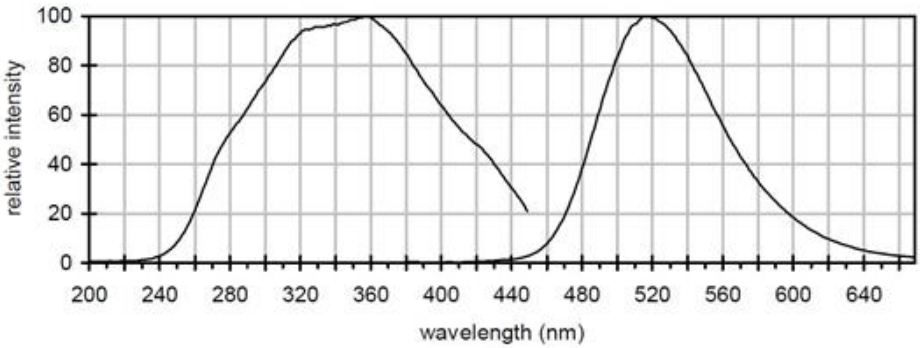

Figure 4.29. Typical excitation (left) and phosphorescence spectra(right) [63].

4.3.2 Photocurrent measurement of FTPD and planar type PDs

1. FTPDs

The goal of this study is to design, fabricate and characterize a flow-through optofluidic sensor with high sensitivity PIN photodiodes embedded in the flow-channel. This idea facilitates an optical fiber-free experiment to detect and transmit the light. In other words, the trench FTPD can not only minimize the loss of light during its transmission, but also simplify the experimental components such as the photodiodes, PMTs or confocal microscopy systems. Fig. 4.30 shows a time domain photocurrent measurement setup.

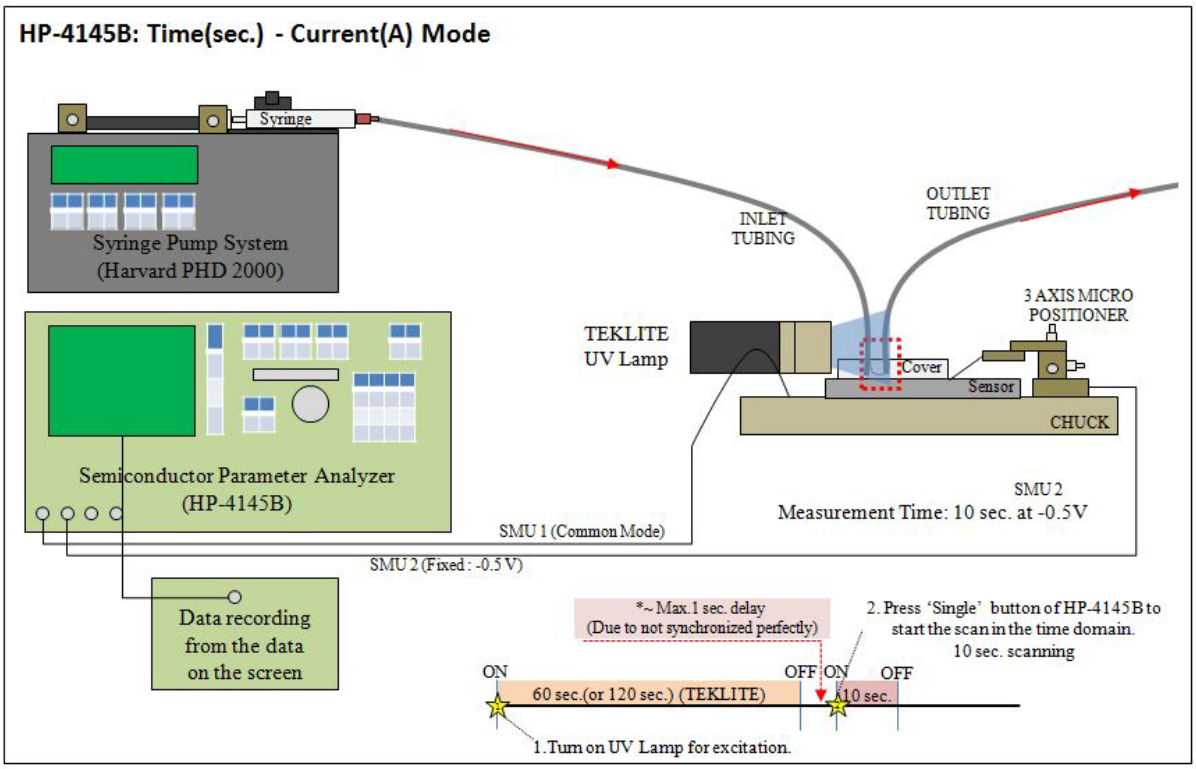

Figure 4.30. Time domain photocurrent measurement setup.

2g/ml-concentration microspheres wetted in a 0.01% solution of DI water and TWEEN 20^{TM} nonionic surfactant (Ethoxylated (20) sorbitan ester from Croda International PLC) for 24 hours was prepared as a fluid [64]. A Harvard PHD-2000 syringe pump system was installed to pump the fluid so that a constant flow rate can be ensured. A Teklite UV lamp was placed near a transparent plastic tube to excite the microspheres inside an area A, as shown in Fig. 4.31.

After 60 seconds UV excitation, the HP-4145B was started in the time domain mode to measure the photocurrent from emitting microspheres as a function of time for 10 seconds. However, the HP-4145B could not start to record current values immediately after the UV lamp was turned off due to the fact that Teklite UV lamp and the HP-4145B were not synchronized together. Moreover, there was maximum 1-2 second delay until the UV light lamp is extinguished completely. Thus, only

photocurrent values 2 seconds after UV lamp turns off were considered. During the measurements, the sampling interval was 0.05 second.

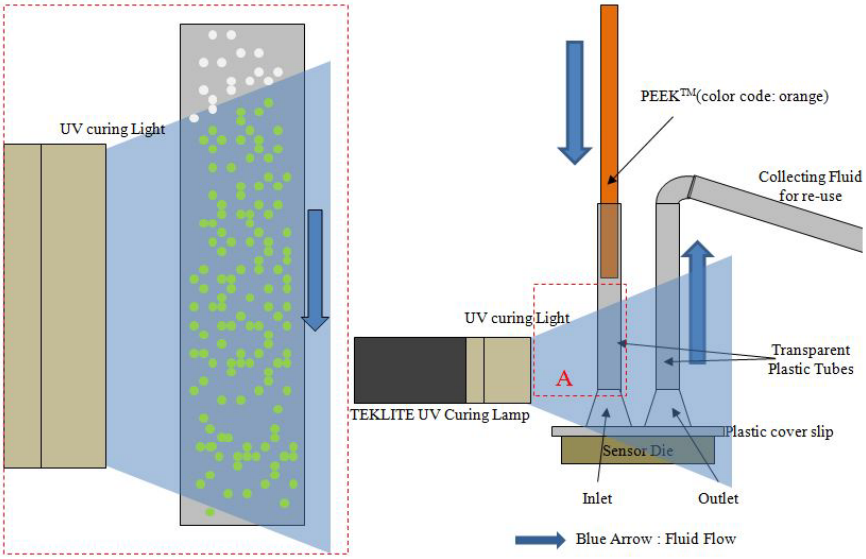

Figure 4.31. Teklite UV lamp setup for excitation of the microspheres.

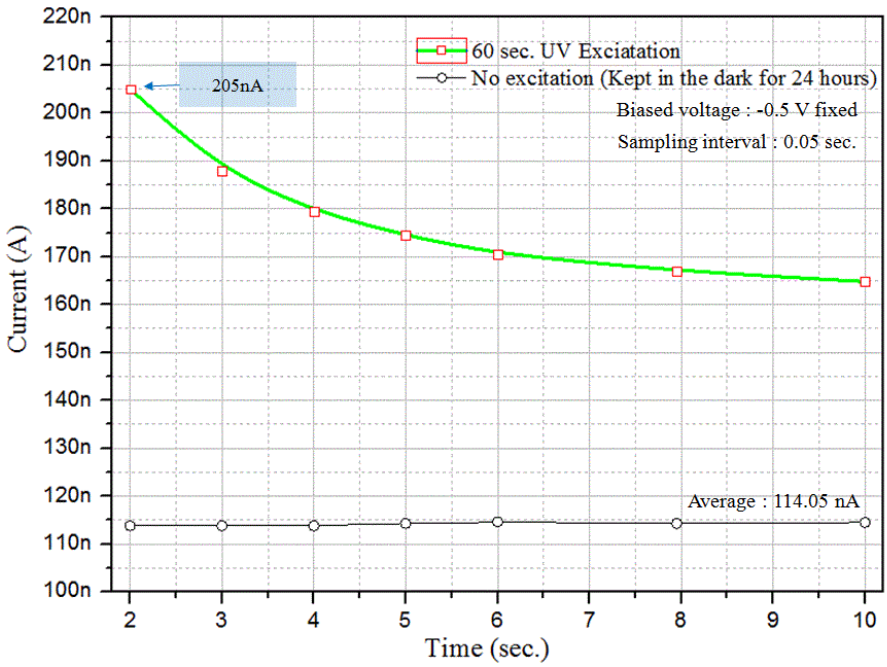

Figure 4.32. Photocurrent from the microspheres' emission as a function of time (2 sec.~ 10 sec.) after 60 sec. excitation at -0.5 V bias. (Sampling interval: 0.05 sec.)

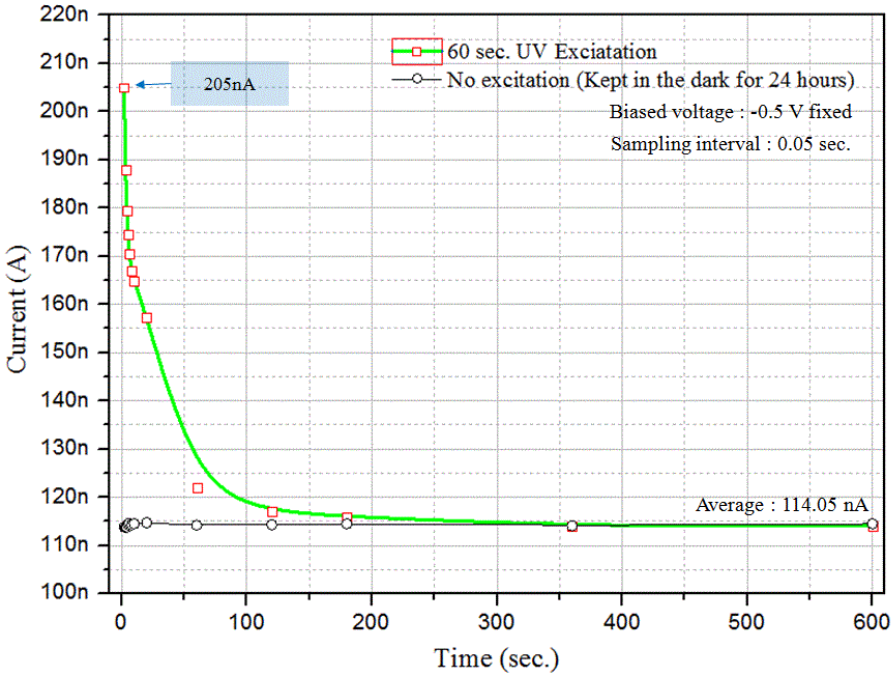

Figure 4.33. Photocurrent from the emitting microsphere as a function of time (2 sec.~ 600 sec.) after 60 sec. excitation at -0.5 V bias. (Sampling interval: 0.05 sec.)

Fig. 4.32 shows the photocurrent from the microspheres from 2 seconds to 10 seconds after UV light excitation. 205 nA current was measured at 2 seconds after UV light turns off, then the current decayed exponentially. In Fig. 4.32 and 4.33, the calculated green line is a B-Spline approximation fitted to the measured values. At 300 seconds, The photocurrent became equal to the dark current level of trench FTDPs. Ceiling lights in the laboratory were turned off and the phosphorescent microspheres were kept in the dark for over 24 hours before measuring the dark current of the FTPDs. The phosphorescent microspheres were still excited to some small degree by weak light in the laboratory during the experiment. The decay time of phosphorescence is much longer than that of fluorescence and this decay can last for minutes to hours until all the excited electron states are exhausted [65-66].

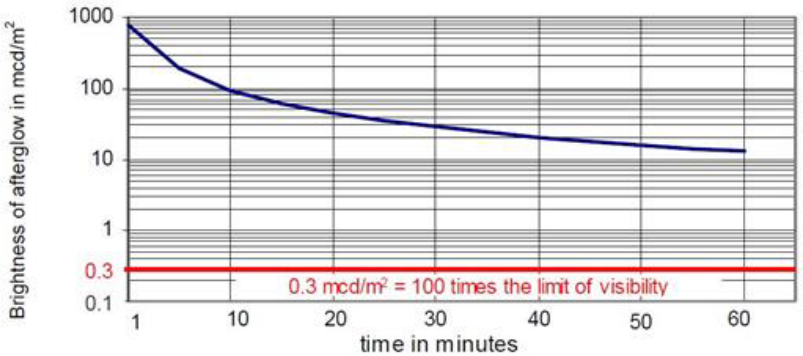

Figure 4.34. Intensity of phosphorescent yellow-green polyethylene microspheres from Cospheric LLC. [63].

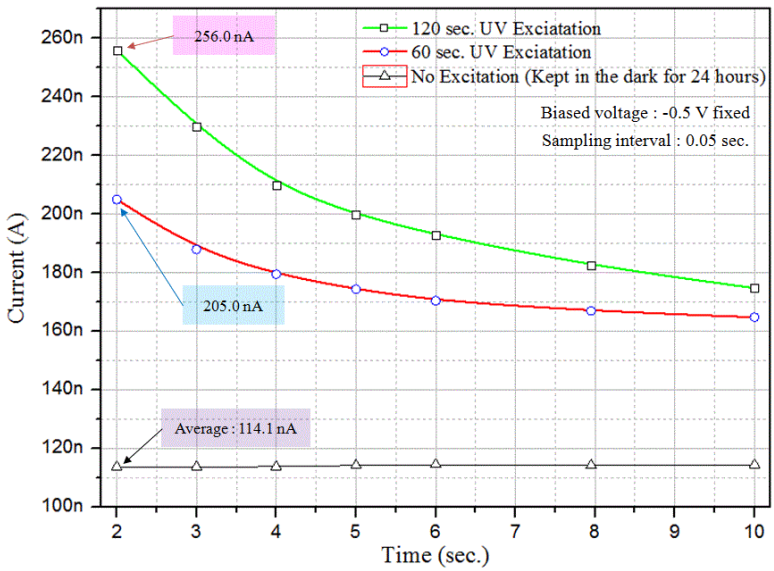

Figure 4.35. Photocurrent as a function of time (2 sec.~ 10 sec.) after 60 sec. excitation at −0.5 V bias. (Sampling interval: 0.05 sec.)

Fig. 4.35 shows the generated photocurrent as a function time for different excitation time conditions. At 2 seconds, the trench FTPD created 256 nA of photocurrent from microspheres excited by UV lamp for 120 seconds, which is around 51 nA or 0.342 μA/cm^2 higher in value than the microspheres excited for 60 seconds. For twice the UV light excitation time, the photocurrent was increased by around 25% for the trench FTPD.

Next, 30 μm diameter polystyrene microspheres coated by phosphorescent pigment were stacked up against each other in the 100 μm width and 80 μm depth trench channel as shown in Fig. 4.36. It is possible that the overlapping microsphere surfaces required longer excitation time until they are fully excited in the channel. However, this may be a minor effect since a polystyrene microsphere is quite transparent for the excitation light [16]. The average dark current level was 114.1 nA.

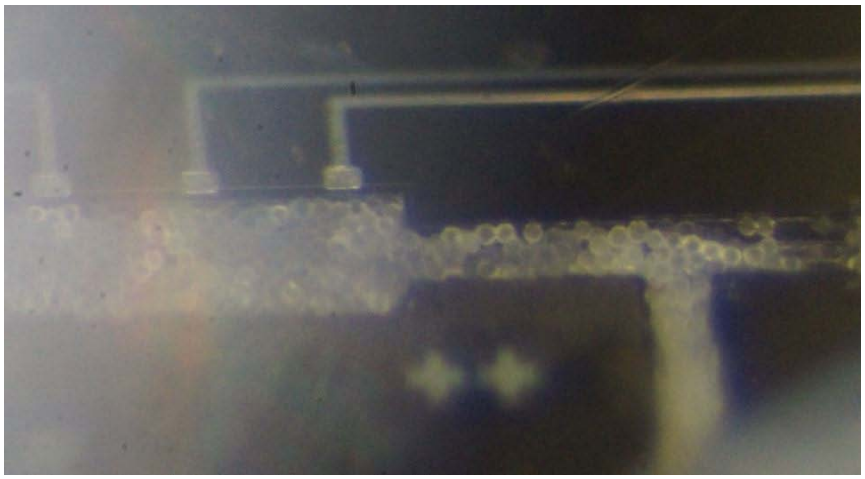

Figure 4.36. Microspheres filling the trench channel.

2. Planar type PDs

The planar FTPD structure offers another method for characterizing the photocurrent. The planar FTPD has PIN photodiodes separated into a single pixels shown in Fig. 4.37. These independent PIN photodiodes allow the sensor to be used for various applications. For instance, a cytometer could be created to count the number of cells or particles flowing through the channel, or multiple microfluidic detectors with various color could create a crude spectrometer. This idea has been applied to the trench FTPDs as well and will be discussed in the next section.

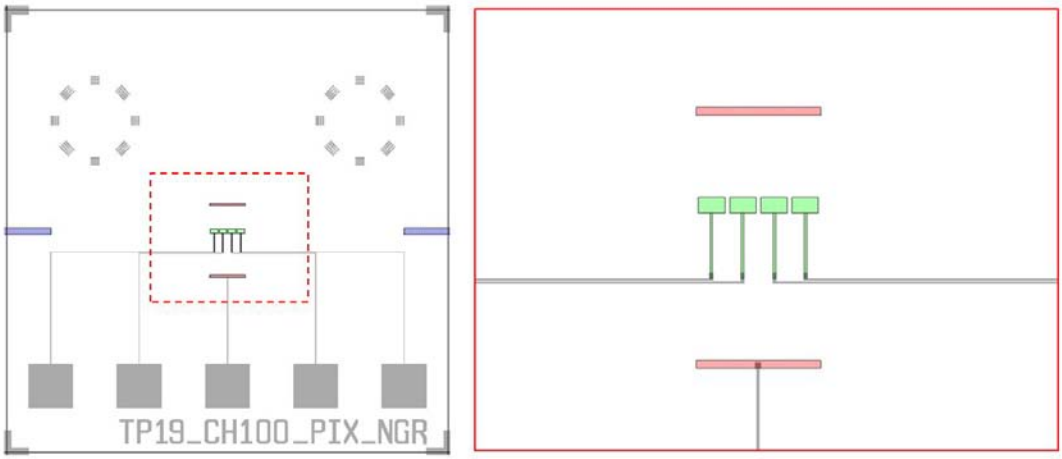

Figure 4.37. Mask design of the planar type PD.

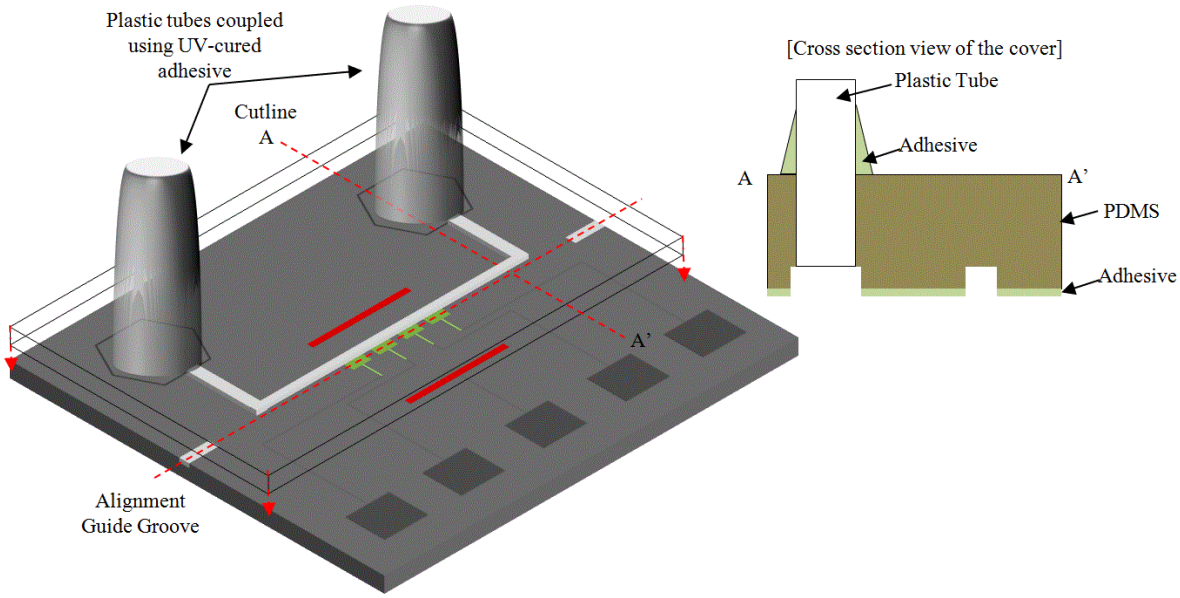

Figure 4.38. Structure of a sealed planar type PDs and its cross-section view (Not to scale).

First, Dow Corning Sylgard 184 PDMS material was used to fabricate a PDMS layer which was used as a cover for the planar type PD. A 10:1 mixture of the silicon elastomer base to the curing agent was prepared for casting a PDMS layer. Plastic tubes (inner diameter: 0.053 inch, thickness of wall: 0.012

inch, outer diameter: 0.077 inch) were molded into the PDMS material during its curing for around 24 hours at room temperature. Again, Norland UV curable adhesive, type NOA#68 was used to seal the coupling area between the plastic tubes and PMDS cover layer as shown in Fig. 4.38.

Another method for making a channel cover is to use a cover die which only has a trench channel and drilled inlet and outlet holes in it created by laser machining as shown in Fig. 4.39. Next, the cover die is flipped over for assembly with the sensor die. In this case, depositing a chrome or aluminum layer over the cover die increases the reflection of the light in the trench when they are assembled. As a result, the reflecting layer facilitates less of the light from particles in the trench.

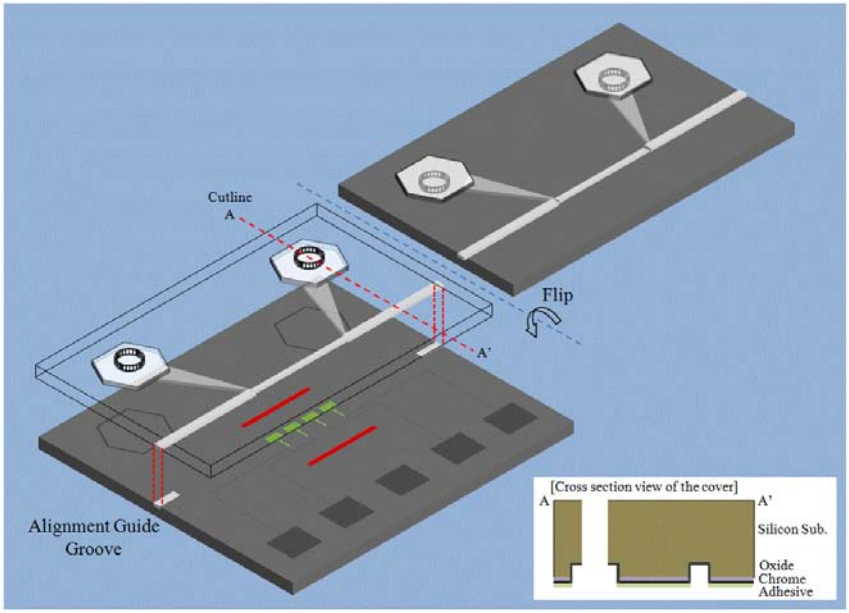

Figure 4.39. Structure of a sealed planar type PD and its cross-section view from Fig. 3.4.

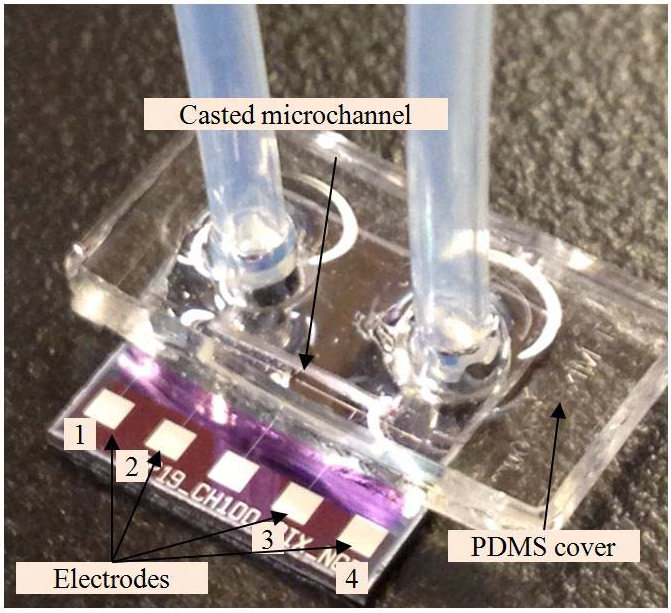

Figure 4.40. A sealed planar type PDs and its microchannel.

Similar to the previously performed procedure in the trench FTPD measurement, signal measurement of the planar FTPD was carried out by connecting to a HP-4145B operating in the time-domain measurement mode. Dark current measurements of each single PD in the planar type PD were taken using four electrodes, pin 1 through pin 4 as indicated in Fig. 4.40. A positive DC bias voltage was applied to the cathode (backside) to create a reverse bias on the photodiode. The size of each separated PD is a 100 μm by 170 μm rectangle. A dark current of 2.82 nA was measured at −10 V bias voltage. Current values collected from pin 1, pin 2 and pin 3 were similar to each other. In contrast, pin 4 showed larger current after negative 12 V and the current reached around 35 nA when a − 40 V bias voltage applied.

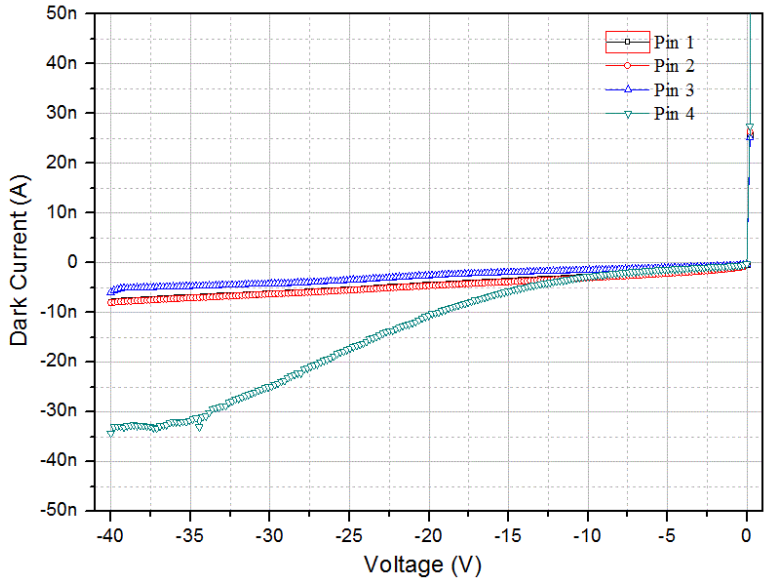

Figure 4.41. Dark current measurement of the planar type PD as a function of the reverse bias voltage.

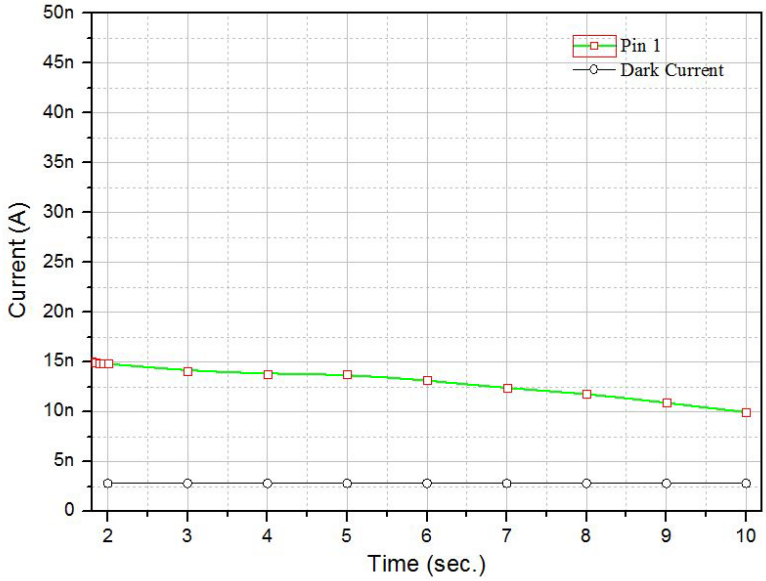

Figure 4.42 Photocurrent from Pin 1 as a function of time (0.1 sec.~ 10 sec.) after 60 sec. excitation at -10 V bias. Dark current at -10V is 2.82 nA.

Fig. 4.41 and 4.42 show the measured photocurrent of the planar type PD at pin 1. The reverse bias voltage was fixed at −10 V during the photocurrent measurement. The photocurrent generated by the phosphorescent emission was 14.8 nA after 2 seconds. After 8 seconds (10 seconds since the UV light was turned off), photocurrent of 9.95 nA was produced and it shows a 0.606 nA/sec linear decay rate from 2 seconds to 10 seconds.

Also, in case that the microsphere emission photocurrent is very small, a transresistance amplifier circuit can be employed in order to covert the photocurrent to a voltage signal.

4.3.3 Improving the performance of the FTPDs

1. Minimizing the dark current

From the measurements of single trench PDs and trench FTPDs, even though they have much better sensitivity and quantum efficiency, the only remaining issue is that the trench type PDs have a larger amount of the dark current than planar type PDs. As discussed previously, scallops on the sidewall surface of trench were considered as one of the origins of the generated dark current. The Bosch-DRIE process is a time-multiplexed or pulsed etch, and it alternates repeatedly between an etching and a depositing phase to fabricate nearly a vertical structure with a high aspect ratio. These repeated etching and deposition cycles result in the rough sidewalls, called scallops, with an amplitude of about 100–500 nm. In general, short cycles produce smoother sidewalls. Thus, a design trade-off between fabricating deeper trenches and smoother sidewalls may be required. Instead of the Bosch-DIRE process, a cryo-DRIE process can be employed to yield smoother sidewalls of the trench without repeated etching and depositing steps. The cryo-DRIE process involves chilling the processing wafer to −110 °C or 163 K) so that chemical reactions on the sidewalls occur slowly. However, commonly used mask materials patterned on the processing wafer can easily crack due to the very low temperature.

2. Separating the PD of the trench FTPD by laser machining.

As discussed in Chapter 3, the channel can be divided using laser micromachining so that each electrode and each divided PIN photodiodes can operate independently and detect the light as shown in Fig. 4.43, similar to a 1 by 4 pixel-detector. Here, 25 μm wide and 200 μm long cross marks (gray colored area) can be used as a cutting guide to separate the PDs during the laser micro-machining process.

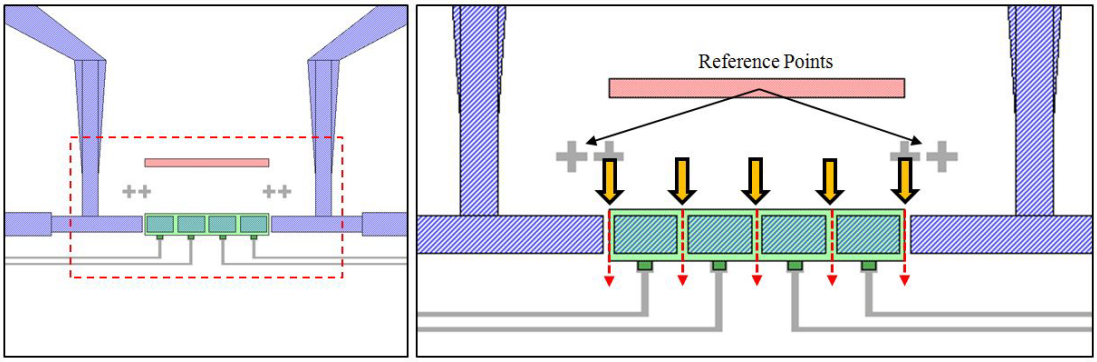

Figure 4.43. Laser cutting process to separate a large PD into isolated trench PDs. Cross marks represent reference points to assist in alignment of the laser cutting.

3. Increasing quantum efficiency using anti-reflection coating

A 1 μm thickness silicon dioxide was deposited as a passivation layer of in the trench FTPDs by plasma enhanced chemical vapor deposition (PECVD). For the trench FTPD, the primary uses of this passivation layer are not only to protect the sensor from dust or humidity, but also to cover the entire boron doped region since this region will be used as a channel where the fluid flows. Cracks or partially covered passivation layer areas can cause electrical shorts. For this reason, a fairly thick 1 μm silicon dioxide layer was deposited. However, an anti-reflection coating could be created by optimizing the materials and their thickness.

Chapter 5

Summary and Future Work

This chapter summarizes the accomplishments of this study and suggests possible future works. Future work on the incorporation of PIN photodiodes into a fluidic channel has application to the development of highly sensitive biosensors.

5.1 Summary

This study demonstrates pioneering research in the field of integrated optical sensors for biosensing applications. The goal of this work is to develop optoelectronic devices with high photon collection efficiency by designing effective and unique device structures for micro diagnostics. Even though various novel optical biosensor designs have been introduced for a long period of time, there are still limitations on photon collection efficiency, portability and cost. By integrating the photodiode and microfluidic channel, this sensor promises a high photon collection efficiency and responsivity to light. Since the FTPD consists of a fluidic channel trench that has a PIN photodiode created on both bottom and walls of the trench, this sensor improves the photon collection efficiency. Moreover, the optical loss is suppressed by a reflective cover which is placed over the channel.

Semiconductor microfabrication processes were utilized to reduce the size and cost and improve the portability. On the other hand, due to the unique geometry of the sensor, specifically designed micro fabrication processes were required. Various microfabrication issues occurred during this development, and these have been resolved as described in Chapter 3.3.3.

Electrical, optical and microfluidic measurements were performed to evaluate the characteristics of the FTPD. The dark current density of the FTPD was measured to be 1.76×10^5 A/cm^2 at −2 V reverse bias voltage and its breakdown voltage was 240 V. The trench type PD shows a higher responsivity to the light and a higher external quantum efficiency than a planar type PD. Also, the trench PD with a deeper trench depth generated more photocurrent and showed higher responsivity and quantum efficiency than shallower trench PDs.
Through microfluidic measurements, the FTPD created 256 nA of photocurrent from emission by phosphorescent microspheres which were excited by a UV lamp for 120 seconds. By comparison, the planar type PD showed as 14.8 nA photocurrent generated by the phosphorescent emission. The back ground dark current of these two sensors were 114.05 nA and 2.83 nA, respectively. A transresistance amplifier circuit can be employed in order to covert the output signal from current to voltage.

However, since the back ground dark current is amplified together with the signal obtained from microspheres emission, the dark current needs to be suppressed. In order to reduce the dark current, the photodetector must be biased with a voltage as low as possible. In the future, improvements on reducing background dark current are expected by separating active area of FTPD and modifying microfabrication processes.

The FTPD improves the photon collection efficiency and the responsivity to light when compared to conventional planar type photodiodes. This sensor can be used for biosensing applications such as disease detection, cell counting, laser induced fluorescence detection, and miniaturized total analysis systems.

5.2 Future Work

5.2.1 Separating active areas of the FTPD through laser micromachining

The main befit of separating the active areas of FTPD is to reduce the overall active area and to thereby suppress the back ground dark current. The active are of the FTPD includes the entire trench area designed for the inlet and outlet holes and optical fiber grooves due to the limitation of microfabrication process. This unnecessary photodiode area causes the undesired dark current, and it also limits some applications.

Separating the active area allows the photodiodes to operate independently. Moreover, dark current collection from the electrode is limited to separated area. A 1 × 4 photodiode array operating individually can be created by laser machining tool since there are four electrodes as described in section 4.3.3.

However, testing the resistance between separated photodiodes must be performed to make sure the active areas are completely electrically isolated by the laser machining process. Melted silicon and doped-silicon particles created by the laser machining might affect to the resistance between the separated photodiodes. Test patterns to evaluate this consideration are designed on the wafer. As an alternative method, depositing oxide and oxide patterning can be performed immediately after the DRIE process to diffuse p+ boron not into the entire trench area, but only into the patterned areas. However, in this study, this method was not undertaken because it involves some process risk.

In addition reducing the back ground dark current, a 1 × 4 photodiode array with individually addressable pixels can extend the field of its applications, especially those involving cytometry and research on living cells, and microgel electrophoresis for virus and genetic analysis.

As another method to separate the active areas, a 1 μm thick oxide mask layer can be used. Depositing and patterning a 1 μm oxide mask layer can be performed immediately after the DRIE process in order for boron atoms to diffuse into only the desired areas. The effectiveness of such an approach is questionable because of many unknown factors associated with conformal oxide coating and

patterning. Even microfabrication experts were not sure of the potential for success using this approach. However, this method now appears more feasible, since the photolithography process conditions for obtaining 80 μm deep trenches have been developed and tested through this study. A sufficient design margin will improve the success rate of the process.

5.2.2 Improvement of optical coupling and sealing

In this study, an optical fiber was not used to excite the microspheres. For more efficient UV excitation, an 80 μm diameter cladding optical fiber can be inserted into the groove. Sealing difficulties and optical coupling issues can be resolved by designing an acrylic sealing component. The acrylic component can integrate the fluidic channel, tubing inlet, outlet, optical fiber grooves and filters as well as offerings perfect improved sealing to minimize any fluid leakage.

5.2.3 Future applications

Appling the FTPD sensor in more sophisticated biosensing applications is a logical extension of this work. The sensor may need to be redesigned to be compatible with different sensing concepts or the spectral range of the emitting microspheres.

Multiple color detection is possible by fabricating optical filter layers over each active area. In this case, different fluorescent molecules have different excitation and fluorescence wavelengths. By utilizing dichroic filters specific wavelengths can be blocked or passed [67]. Moreover, an FTPD with a segmented array of photodiodes can be used for capillary electrophoresis to detect DNA migration pattern for identification of viral strains. An array of photodiodes for the FTPD can be integrated into an optical detector for disease and genetic analysis sensors to detect the intensity profile of fluorescent light along an agarose gel for gel electrophoresis of DNA.

List of References

[1] A. P. F. Turner, " Biosensors: sense and sensibility", Chem. Soc. Rev., 42, pp. 3184-3196, 2013.

[2] All-printed amperometric biosensor platform, www.acreo.se, Sweden.

[3] P. Zuo, X. Li, D. C. Dominguez and B. Ye, "A PDMS/paper/glass hybrid microfluidic biochip integrated with aptamer-functionalized graphene oxide nano-biosensors for one-step multiplexed pathogen detection", Lab Chip, 13, pp. 3921-3928, 2013.

[4] H. Shi, B. Song, F. Long, X. Zhou, M. He, Q. Lv, and H. Yang, "Automated online optical biosensing system for continuous real-time determination of microcystin-LR with high sensitivity and specificity: Early warning for cyanotoxin risk in drinking water sources", Environmental Science & Technology, Vol. 47, no. 9, pp. 4434-4441, 2013.

[5] F. Long, A. Zhu, H. Shi, H. Wang and J. Liu, "Rapid on-site/in-situ detection of heavy metal ions in environmental water using a structure-switching DNA optical biosensor", Sci. Rep., online, 2013.

[6] A. Sassolas1, B. Prieto-Simón, J. Marty, "Biosensors for pesticide detection: New trends", American Journal of Analytical Chemistry, 3, pp. 210-232.I1, 2012.

[7] D. Ho, "CMOS contact imagers for spectrally-multiplexed fluorescence DNA biosensing", Dissertation of Doctor of Philosophy, Department of Electrical and Computer Engineering, University of Toronto, 2013.

[8] Z. Wang, Y. Fan, J. Chen, Y. Guo, W. Wu, Y. He, L. Xu, F. Fu, "A microfluidic chip-based fluorescent biosensor for the sensitive and specific detection of label-free single-base mismatch via magnetic beads-based 'sandwich' hybridization strategy", electrophoresis, Vol. 34, Issue 15, pp. 2177–2184, 2013.

[9] Z. Wang, J. Chen, Y. Fan, W. Wang, F. Fu, " A novel micro-fluidic biosensor for the rapid and sequence-specific detection of DNA with electrophoretic driving mode and laser-induced fluorescence detector", Microfluidics and Nanofluidics, , Vol. 14, Issue 1-2, pp 145-152, 2013.

[10] E. Ban, E. Song, "Recent developments and applications of capillary electrophoresis with laser-induced fluorescence detection in biological samples", Journal of Chromatography B, Vol. 929, no. 15, pp. 180-186, 2013.

[11] Y. Tung, M. Zhang, C. Lin, K. Kurabayashi, S. J. Skerlos, "PDMS-based opto-fluidic micro flow cytometer with two-color, multi-angle fluorescence detection capability using PIN photodiodes", Sensors and Actuators B, 98, pp. 356–367, 2004.

[12] Y. Garini, I. T. Young, G. McNamara, "Spectral imaging: principles and applications", Cytometry Part A, Vol 69A, Issue 8, pp. 735-747, 2006.

[13] T. Zimmermann, J. Rietdorf, R. Pepperkok, "Spectral imaging and its applications in live cell microscopy", FEBS Letters, Vol. 546, Issue 1, 3, pp. 87-92, 2003.

[14] R. Singh, D. Ho, A. Nilchi, G. Gulak, P. Yau, and R. Genov, “A CMOS/Thin film fluorescence contact imaging microsystem for DNA analysis,” IEEE Trans. Circuits and Systems I, vol. 57, no. 5, pp. 1029–1038, 2010.

[15] Drent, P., "Properties and selection of objective lenses for light microscopy applications. Microscopy and Analysis", 19, pp. 5-7, 2005.

[16] R. E. Hummel, Electronic Properties of Materials, 3rd edition, Appendix 4, pp. 413.

[17] Peter Y. Yu, Manuel Cardona, "Fundamentals of Semiconductors: Physics and Materials Properties", 2010.
[18] Sima Dimitrijev, Principles of Semiconductor Devices, Edition 6, Oxford University Press, pp. 187, 2005.
[19] S. M. Sze, K. K. Ng, Physics of Semiconductor Devices, Hoboken, NJ, Wiley-Interscience, 2007.
[20] J. Hodak, "Introduction to fluorescence and phosphorescence", Spectroscopy for Chemistry BSAC program, 2008.
[21] P. de Paula, J. Atkins' Physical Chemistry, Oxford University Press, 2002.
[22] R. Dieme, "Investigation of process fabrication for low-noise p-type diffused piezoresistors", Ph.D. Dissertation, Department of Electrical and Computer Engineering, University of Florida, 2009.
[23] Nyquist, “Thermal agitation of electric charge in conductors,” Phys. Rev. 32, pp. 110-113, 1928.
[24] B. Johnson, “Thermal agitation of electricity in conductors,” Phys. Rev. 32, pp. 97-109, 1928.
[25] W. Schottky, "Über spontane stromschwankungen in verschiedenen elektrizitätsleitern", Annalen der Physik, vol. 57, pp. 541–567, 1991.
[26] Designing Photodiode Amplifier Circuits with OPA128, BURR-BROWN, Application Bulletin.
[27] L. M. Terman, “An investigation of surface states at a silicon/silicon oxide interface employing metal-oxide-silicon diodes,” Solid-State Electron. 5(5), pp. 285-299, 1962.
[28] T. Nakamura, H. Kitada, Y. Mizushima, N. Maeda, K. Fujimoto, T. Ohba, "Comparative study of side-wall roughness effects on leakage currents in through-silicon via interconnects," 3D Systems Integration Conference (3DIC), 2011 IEEE International, pp.1-4, 2012.
[29] A. L. McWhorter, "1/f noise and germanium surface prosperities", In Semiconductor Surface Physics, R. H. Kingdton (Ed.), University of Pennsylvania Press, Philadelphia, PA, pp. 207–228, 1957.
[30] F. N. Hooge, "1/f noise is no surface effect", Physics Letters, 29A (3), pp. 139–140, 1969.
[31] E. Cocheteau, B. Belier, L. Bary, and R. Plana, “Formation of ultra-shallow p+/n junctions using BF2 implantation for the fabrication of improved piezoresistive cantilevers,” Eleventh International Conference on Solid-State Sensors and Actuators, Munich, Germany, 2001.
[32] B. Belier, C. Bergaud, E. Cocheteau, L. Bary, and R. Plana, “Formation of implanted piezoresistors under 100-nm thick for nanoelectromechanical systems,” Fifteen IEEE International Conference on Micro Electro Mechanical Systems, Las Vegas, NV, pp. 360-363, 2002.
[33] M. Lang, "Complete monolithic integrated 2.5 Gbit/s optoelectronic receiver with large area MSM photodiode for 850 nm wavelength", ELECTRON LETT, pp. 1247-1249, 2001.
[34] D.A. Neamen, "Semiconductor Physics and Devices", McGraw-Hill, pp. 645-647, 2003.
[35] Photodiode Characteristics and Applications, UDT Sensors Inc., CA, pp. 7.
[36] Y. Tung, M. Zhang, C. Lin, K. Kurabayashi, S. J. Skerlos, "PDMS-based opto-fluidic micro flow cytometer with two-color, multi-angle fluorescence detection capability using PIN photodiodes", Sensors and Actuators B, 98, pp. 356–367, 2004.
[37] S. W. Kettlitz, S. Valouch, W. Sittela and U. Lemmera, "Flexible planar microfluidic chip employing a light emitting diode and a PIN-photodiode for portable flow cytometers", Lab on a Chip, pp. 12, 197, 2012.
[38] L. Cui, T. Zhang, H. Morgan, "Optical particle detection integrated in a dielectrophoretic lab-on-a-chip", J. Micromech. Microeng. 12, pp. 7–12, 2002.

[39] Y. Mita, K. Hirose, M. Kubota, T. Shibata, "Deep-trench vertical Si photodiodes for improved efficiency and crosstalk," Selected Topics in Quantum Electronics, IEEE Journal of, vol.13, no.2, pp. 386-391, 2007.
[40] S. Akamine, H. Kuwano, H. Yamada, "Scanning near-field optical microscope using an atomic force microscope cantilever with integrated photodiode," Applied Physics Letters , vol.68, no.5, pp.579-581, 1996.
[41] E. H. Altendorf, E. Iverson, D. Schutte, B. H. Weigl, T. D. Osborn, R. Sabeti, P. Yager, "Optical flow cytometry utilizing microfabricated silicon flow channels". Proc. SPIE 2678, Optical Diagnostics of Living Cells and Biofluids, pp. 267, 1996.
[42] A. Rochas, A. R. Pauchard, P. Besse, D. Pantic, Z. Prijic, R. S. Popovic, "Low-noise silicon avalanche photodiodes fabricated in conventional CMOS technologies," Electron Devices, IEEE Transactions on , vol.49, no.3, pp.387-394, 2002.
[43] S. Franssila, Introduction to Microfabrication, published by John Wiley & Sons in 2004.
[44] PDS Products N-Type Planar Diffusion Sources, Product Datasheet, Saint-Gobain Ceramic Materials, PA, pp. 3-4, 2011.
[45] G. S. May, S. M. Sze, "Fundamentals of Semiconductor Fabrication", John Wiley & Sons in 2004.
[46] PDS Products P-Type Planar Diffusion Sources, Product Datasheet, Saint-Gobain Ceramic Materials, PA, pp. 2-3, 2011.
[47] D J Hayton1, T E Jenkins1, P Bailey2 and T C Q Noakes," Optical and ion-scattering study of SiO2 layers thermally grown on 4H-SiC", Semicond. Sci. Technol. 17 L29, 2002.
[48] S. Wolf and R. N. Tauber, "Silicon processing for the VLSI era vol. 1: Process technology", Lattice Press, 2000.
[49] Sami, "Introduction to microfabrication", Wiley, pp. 119–130, 1995.
[50] N. T. Nguyen, "Spin-on glass materials and applications in advanced IC technologies", Ph.D. Dissertation, University of Twente, pp. 39, 1999.
[51] PDS Product P-type Planar Diffusion Sources - Low Temperature Oxidation and Silicon-Boron (Si-B) Layer, Technical Bulletin, SGBN-PDS-TB1-113011, Saint-Gobain Ceramic Materials, PA. 2011.
[52] H. Wang, “silicon x-ray smart sensor micromodule and microsystems”, Ph.D. dissertation, Department of Electrical Engineering and Infotech Oulu, University of Oulu, University of Oulu, Oulu, Finland, 2002.
[53] R. L. Byer, “Diode laser-pumped solid-state lasers”, Science 239, 742, 1988.
[54] M. A. Green, M. J. Keevers, "Optical properties of intrinsic silicon at 300 K", Progress in Photovoltaics: Research and Applications, vol. 3, pp. 189 - 192, 1995.
[55] Silicon PIN Photodiode: model- S10783-4 data sheet, Hamamatsu photonics USA, CA.
[56] S. Satyanarayana, R. N. Karnik, A. Majumdar, "Stamp-and-stick room-temperature bonding technique for microdevices," Microelectromechanical Systems, Journal of , vol.14, no.2, pp.392,399, 2005.
[57] M. A. Schmidt, “Wafer-to-wafer bonding for microstructure formation,” Proc. IEEE, vol. 8, pp. 1575–1585, 1998.
[58] Norland adhesives information., Norland Products Inc, NJ.
[59] H. Kawaguchi, "Functional polymer microspheres", Prog. Polym Sci. 25, pp. 1171-1210, 2000.
[60] K. Sahil, " Microsphere: A review", International Journal of Research in Pharmacy and Chemistry,

IJRPC, 1(4), 2011.
[61] Microsphere selection, revision 1.03, Product information documents, Bangs Laboratories, Inc., IN, 2013.
[62] Bangs Beads Technical Product Guide 2012-2013, pp. 56, Bangs Laboratories, Inc., IN, 2013.
[63] Phosphorescent yellow-green microspheres, Phosphorescence Microsphere information in Cospheric LLC., Santa Barbara, CA,
[64] Protocol for preparing TWEEN 20 solutions, Document number: SOP-00018, revision: 01, Cospheric LLC., Santa Barbara CA.
[65] Manual for using fluorescent microspheres to measure regional organ perfusion fluorescent microsphere resource center, Division of pulmonary and critical care medicine, University of Washington, pp 23, 1999.
[66] K. Shin, S. Lee, K. Han, S. Kim, E. Yang, J. Park, B. Ju, J. Kang, T. Kim, "Amplification of fluorescence with packed beads to enhance the sensitivity of miniaturized detection in microfluidic chip", Biosensors and Bioelectronics, Vol. 22, pp. 2261-2267, 2007.
[67] J. M. Eichenholz, J. Dougherty, "Ultracompact fully integrated megapixel multispectral imager", Proc. SPIE 7218, Integrated Optics: Devices, Materials, and Technologies XIII, 721814, 2009.